

MICROSCOPIC FLOW OF VISCOELASTIC WORMLIKE MICELLAR SOLUTIONS  
THROUGH CONTRACTION GEOMETRIES

by

Emad Jafari Nodoushan, M.S., B.S.

A dissertation submitted to the Graduate Council of  
Texas State University in partial fulfillment  
of the requirements for the degree of  
Doctor of Philosophy  
with a Major in Materials Science, Engineering and Commercialization  
August 2020

Committee Members:

Namwon Kim, Chair

Bahram Asiabanpour

William Chittenden

Young Ju Lee

Byoung Hee You

**COPYRIGHT**

by

Emad Jafari Nodoushan

2020

## **FAIR USE AND AUTHOR'S PERMISSION STATEMENT**

### **Fair Use**

This work is protected by the Copyright Laws of the United States (Public Law 94-553, section 107). Consistent with fair use as defined in the Copyright Laws, brief quotations from this material are allowed with proper acknowledgement. Use of this material for financial gain without the author's express written permission is not allowed.

### **Duplication Permission**

As the copyright holder of this work I, Emad Jafari Nodoushan, refuse permission to copy in excess of the "Fair Use" exemption without my written permission.

## **ACKNOWLEDGEMENTS**

I would like to express my sincere appreciations to people who generously supported me through this project. First and foremost, I would like to thank Dr. Namwon Kim, my PhD advisor for his consistent guidance, scientific advices, stimulating questions, motivating and support during my studies. I am grateful for the opportunity that I had to work under his supervision, gain knowledge and learn several skills.

I also thank Dr. Young Ju Lee, for his contributions to various aspects of this research, guidance, and encouragement that helped me to move forward with my studies. I would also like to thank my advisory committee members, Dr. Bahram Asiabanpour, Dr. William Chittenden, and Dr. Byoung Hee You for providing valuable feedbacks, thoughtful comments and recommendations that made this research moving forward.

I would like to thank Dr. Jennifer Irvin, the director of Materials Science, Engineering and Commercialization (MSEC) program, for all her supports and helps without which I would not be able to make it through my PhD. I also thank Ms. Karla Pizana and Ms. Kelsie Crumpton from the MSEC program and Ms. Sarah Rivas from Ingram School of Engineering for helping me with the administrative procedures.

Finally, I thank my beloved family for being supportive and motivative along my education.

## TABLE OF CONTENTS

	<b>Page</b>
ACKNOWLEDGEMENTS.....	iv
LIST OF FIGURES .....	viii
LIST OF ABBREVIATIONS.....	xi
ABSTRACT.....	xiii
CHAPTER	
I. INTRODUCTION.....	1
1.1. Introduction .....	1
1.2. Aims and Objectives .....	5
1.3. Outline of Dissertation .....	6
II. BACKGROUND .....	8
2.1. Formation of Micellar Structures.....	8
2.2. Wormlike Micelles.....	9
2.3. Linear Rheology of WMS.....	13
2.4. Non-linear Shear Rheology of WMS.....	15
2.5. Shear Induced Structures .....	18
2.6. WMS Under Extensional Flow .....	19
2.7. Contraction Viscoelastic Flows .....	21
III. CHARACTERIZATION METHODS AND EXPERIMENTAL APPARATUS .....	23
3.1. Rheological Characterization.....	24
3.1.1. Dynamic Oscillatory Measurements.....	24
3.1.2. Steady Shear Measurements .....	25
3.1.3. Extensional Rheometry.....	26
3.2. Flow Visualization.....	32
3.2.1. Fluorescent Streak Imaging .....	33
3.2.2. Micro-Particle Image Velocimetry ( $\mu$ -PIV).....	33

IV. RHEOLOGY OF WORMLIKE MICELLAR SOLUTIONS .....	36
4.1. Introduction.....	36
4.2. Theoretical Background.....	37
4.3. Rheological Characterization of Test Fluids.....	39
4.3.1. Preparation of Test Fluids.....	39
4.3.2. Dynamic Oscillatory Shear Measurements.....	41
4.3.3. Steady Shear Measurements .....	43
4.3.4. Extensional Relaxation Times .....	46
4.3.5. Extensional Viscosities .....	50
4.4. Effect of Temperature and Salinity on WMS Rheology.....	51
4.4.1. Preparation of Test Fluids.....	52
4.4.2. Effect of Temperature .....	53
4.4.3. Effect of Secondary Salt .....	59
4.5. Conclusion .....	63
V. MICROSCOPIC FLOW OF WORMLIKE MICELLAR SOLUTION IN CONTRACTION GEOMETRY .....	67
5.1. Introduction.....	67
5.2. Non-Dimensional Numbers .....	68
5.3. Design and Fabrication of Microfluidic Chips .....	72
5.4. Newtonian-Like Flows.....	73
5.5. Evolution of Vorticities.....	76
5.6. Steady Viscoelastic Flows .....	78
5.7. Quasi-Static Secondary Flow Regions.....	83
5.8. Conclusions.....	86
VI. CONCLUSIONS AND RECOMMENDATIONS .....	88
6.1. The Influence of Shear and Extensional Relaxation Times on the Contraction Flow .....	88
6.2. The Ratio of Relaxation Times and its Effect on the Contraction Flow.....	89
6.3. Role of Shear Thinning and High Yield Stress on the Contraction Flow.....	90
6.4. Quasi-Static Secondary Flow Regions and the Role of Shear Banding .....	91
6.5. Recommendations for Future Studies .....	92

REFERENCES .....94

## LIST OF FIGURES

<b>Figure</b>	<b>Page</b>
2.1. The effect of the packing parameter on the shape of micellar structures.....	8
2.2. Schematic diagram of a wormlike micelle.....	10
2.3. A schematic of CTAB/NaSal wormlike structures. ....	12
2.4. Schematic illustration of reptation tube. ....	14
2.5. A) A representation of zero-shear viscosity as a function of the salt to surfactant molar ratio and structural changes in wormlike micelles (the schematic of entangled and branched wormlike micelles are adopted from Candau <i>et al.</i> <sup>55</sup> ). ....	15
2.6. The three typical zones of I: shear thinning, II: shear thickening, and III: shear thinning in a log–log viscosity-shear rate curve from a shear thickening fluid. ....	17
2.7. A Schematic illustration of a sudden contraction geometry and the secondary flows observed in flow of Newtonian and viscoelastic fluids. ....	22
3.1. A) The experimental setup for dynamic shear oscillatory measurements. ....	25
3.2. A) A schematic illustration of CaBER rheometer.....	28
3.3. A) The experimental setup for extensional rheology measurement.....	31
4.1. A schematic illustration of wormlike micellar network with entanglements (shown in dashed circles). ....	38
4.2. Schematic diagram for the formation of wormlike micelles.....	40
4.3. Elastic and loss modulus ( $G'$ and $G''$ ) as a function of angular frequencies. ....	42
4.4. TEM Images of A) $C_d = 50$ mM and B) $C_d = 100$ mM ( $x^*$ in both images represents the network mesh size). ....	43
4.5. Measured shear viscosities as a function of shear rates. ....	44
4.6. Measured shear stresses as a function shear rates. ....	46
4.7. The thinning of filament over time for different CTAB concentration ( $R = 0.32$ , $50 \text{ mM} \leq C_d \leq 100 \text{ mM}$ ). ....	47
4.8. Normalized filament diameter profiles as a function of time. ....	47

4.9. Extensional relaxation times ( $\lambda_E$ ) as a function of CTAB concentration ( $C_d$ ). .....	49
4.10. Extensional viscosities ( $\eta_E$ ) as a function of Hencky strains ( $\epsilon$ ).....	50
4.11. Cole-Cole plots for solution ( $S = 0$ ) at varying temperatures ( $25\text{ }^\circ\text{C} \leq T \leq 60\text{ }^\circ\text{C}$ ).....	54
4.12. Elastic modulus as a function of angular frequency curves plots for solution ( $S = 0$ ) at varying temperatures ( $25\text{ }^\circ\text{C} \leq T \leq 60\text{ }^\circ\text{C}$ ). .....	55
4.13. A) The logarithmic plot of relaxation time and B) the ratio of entanglement length as a function of absolute temperature for solution ( $S = 0$ ) at varying temperatures ( $25\text{ }^\circ\text{C} \leq T \leq 40\text{ }^\circ\text{C}$ ).....	57
4.14. Shear viscosities vs. shear rates of solution ( $S = 0$ ) at varying temperatures ( $25\text{ }^\circ\text{C} \leq T \leq 60\text{ }^\circ\text{C}$ ).....	58
4.15. Shear stresses vs. shear rates of of solution ( $S = 0$ ) at varying temperatures ( $25\text{ }^\circ\text{C} \leq T \leq 60\text{ }^\circ\text{C}$ ).....	59
4.16. Shear viscosity vs. shear rates of solutions with different concentrations of NaCl ( $S = 0, 3, 6$ and $9$ ) at $25\text{ }^\circ\text{C}$ . .....	60
4.17. Shear stresses vs. shear rates plots of solutions with varying amount of NaCl concentration ( $S = 0, 3, 6$ and $9$ ) at $25\text{ }^\circ\text{C}$ . .....	61
4.18. A) Relaxation times and B) the ratio of entanglement length over the average contour length of micelles as a function of $S = \frac{[NaCl]}{[CTAB]}$ for solutions with varying salt concentration ( $S = 0, 3, 6$ and $9$ ) at varying temperatures ( $25\text{ }^\circ\text{C} \leq T \leq 40\text{ }^\circ\text{C}$ ). .....	62
5.1. Schematic diagram of experimental setup for the investigation of WMS behavior at the sudden contraction microchannel. ....	73
5.2. Streak images of solutions with $C_d = 50, 62.5,$ and $75\text{ mM}$ at the same volumetric flow rate of $Q = 0.2\text{ mL/h}$ .....	74
5.3. A De-Wi-Re map showing the summary of flow conditions that each solution showed Newtonian-like flow pattern. ....	74
5.4. Transition from Newtonian-like flows (solid symbols) to Secondary flows (hollow symbols) in terms of viscoelastic Mach number for solutions with $C_d = 50, 62.5,$ and $75\text{ mM}$ . ..	75
5.5. Streak images of solutions with CTAB molar concentrations of $C_d = 50, 62.5,$ and $75\text{ mM}$ . .	76
5.6. The normalized vortex length as a function of A) Wi number and B) De number.....	77

5.7. The normalized vortex length as a function of De numbers that are modified by the ratio of extensional to shear relaxation times.....	78
5.8. Streak images of solutions with CTAB molar concentrations of $C_d = 87.5$ , and 100 mM. ....	79
5.9. The velocity and shear profiles of a Newtonian-flow far from contraction entry and deviation of shear thinning and thickening fluids from the Newtonian velocity profile.....	80
5.10. Profiles of A) the normalized velocity and B) shear rate for a Newtonian-like flow along the lines with the fixed distance from the contraction entry.....	82
5.11. Streak images of WMS with the CTAB molar concentrations of $C_d = 87.5$ , and 100 mM. .	83
5.12. The profiles of shear rates for the test solutions of $C_d = 100$ mM along the perpendicular lines to the channel centerline at the fixed distance from the contraction entry. ....	84
5.13. Maps of A) velocity and B) shear rates at the contraction entry for the test solution of $C_d = 100$ mM at $Q = 1$ mL/h.....	85
5.14. The normalized length of quasi-static secondary flow regions as a function of A) Wi number and B) De number.....	86

## LIST OF ABBREVIATIONS

<b>Abbreviation</b>	<b>Description</b>
SHNC	3-Hydroxy-Naphthalene-2-Carboxylate
CaBER	Capillary Break Up
CTAX	Cetyl Trimethylammonium Halides
CTAT	Cetyl Trimethylammonium Tosylate
CPyCl	Cetylpyridinium Chloride
CTAB	Cetyltrimethylammonium Bromide
CMC	Critical Micellar Concentration
De	Deborah
DOS	Dripping-Onto-Substrate
EIS	Elongation Induced Structure
EOR	Enhanced Oil Recovery
fps	Frame Per Seconds
CTAT	Hexadecyltrimethylammonium P-Toluenesulfonate
HEC	Hydroxyl Ethyl Cellulose
ID	Inner Diameter
LDPE	Low Density Polyethylene
Ma	Mach
OD	Outer Diameter
PEO	Polyethylene Oxide

PMMA	Polymethyl Methacrylate
Re	Reynolds
SIP	Shear-Induced Phase
SIS	Shear-Induced Structure
SAOS	Small Amplitude Oscillation Shear
TTAA	Tris(2-Hydroxyethyl) Tallowalkyl Ammonium Acetate
Wi	Weissenberg
WMS	Wormlike Micellar Solutions

## ABSTRACT

Viscoelastic fluids are commonly used in many engineering applications such as in polymer processing industry, enhanced oil recovery and inkjet printing. Viscoelastic contraction flow represents the most common flow condition in those applications, but the flow is associated with its inherent problems such as additional pressure drops and flow instabilities. It is well known that formation of secondary flows at the upstream corners of the contraction greatly influences the fluidic behavior and promotes the flow instabilities. Therefore, investigating the flow conditions that induce the secondary flow has been an extensive research subject with the ultimate goal of elucidating the kinematics of viscoelastic contraction flows. Several relevant studies concluded that formation of secondary flow is influenced greatly by the elastic stress associated with the viscoelastic flow. Non-dimensional numbers that estimates the ratio of elastic stress to viscous (Wi and De numbers) or inertial (El number) stress has been used to quantify the effect of elasticity on the viscoelastic flow behavior. Even though a general consensus has been established that the higher elastic stress promoted the formation and enhancement of secondary flow, quite different flow behaviors were reported for the different fluids at the same level of elastic stress. Additionally, comparable secondary flows were also observed at different levels of elastic stresses. It should be noted that these non-dimensional numbers could not solely characterize the behavior of viscoelastic contraction flow. In this study, in addition to the role of elastic stress, the contribution of shear dependent rheology and extensional characteristics of the viscoelastic test fluids to the contraction fluidic behavior has been investigated experimentally. Wormlike micellar solutions (WMS) were chosen as the viscoelastic test fluids in virtue of their advantageous characteristics over polymer solutions and their growing applications. The shear and extensional rheology of the test fluids were characterized, and the velocity and shear deformation profiles associated with their contraction flow were quantitatively measured. Secondary flows in the form of upstream corner vortex were observed at sufficiently high elastic stresses where the viscoelastic Mach number ( $Ma = \sqrt{DeRe}$ ) was larger than the unity. The length of secondary flows was found to be correlated with both the elastic stress (De number) and the ratio of extensional to shear relaxation times ( $\frac{\lambda_E}{\lambda}$ ). For the test fluids that showed high yield stress and strong shear thinning rheology, a new type of secondary flows with a quasi-static condition ( $\sim$ zero velocity) was observed at the upstream corner of contraction entry. Furthermore, the role of shear stress and shear viscosity in forming the quasi-static secondary flow has been discussed for the first time by matching the shear rates measured from the quantitative analysis of viscoelastic contraction flow to the rheological behaviors of the test fluids.

# I. INTRODUCTION

## 1.1. Introduction

Contraction flows of viscoelastic fluids have particular importance in many polymer processing techniques such as extrusion, injection molding, and film blowing,<sup>1-3</sup> and also in more recent applications like ink-jet printing,<sup>4</sup> enhanced oil recovery (EOR),<sup>5</sup> and microfluidic rheometry for characterization of viscoelastic fluids at high deformation rates.<sup>6, 7</sup> Flow instabilities and extra pressure drops have been commonly reported for contraction viscoelastic flows. Formation and enhancement of secondary flows (*i.e.* corner vortices) have been observed in the upstream corner of contraction entry, which influenced the flow behavior and promoted flow instabilities.<sup>8,9</sup> The ultimate goal of investigating the contraction flows of viscoelastic fluids is to elucidate their flow kinematics. Therefore, understanding the flow conditions inducing the formation and enhancement of secondary flows has been a main motivation for studying the contraction flows.<sup>10</sup>

Despite the numerous experimental and numerical investigations, much less is known about viscoelastic flows compared to the well understood Newtonian flows. The behavior of viscoelastic fluids is influenced by the rate of deformation, types of deformation caused by shear or extension, and rheological properties of the fluids. A contraction flow is associated with a complex field of regions with the strong shearing near the walls and the non-homogeneous extension along the centerline of contraction entry.<sup>11-13</sup> The Newtonian contraction flows only showed the small secondary flows, so called Moffat vortices, at very high levels of inertial to viscous stresses quantified by Reynolds numbers ( $Re = \frac{\text{Inertial Forces}}{\text{Viscous Forces}}$ , *i. e.*  $Re > 200$ ).<sup>14</sup> In contrast, very large corner vortices were observed from contraction viscoelastic flows even at very small  $Re$  (*i.e.*  $\ll 1$ ). The viscoelastic fluids differ

from Newtonian fluids in terms of their elastic properties. Thus, the ratio of elastic to viscous characteristics is considered as an important factor influencing the behavior of contraction viscoelastic flows. Whether a viscoelastic fluid behaves elastic-like or fluid-like is indeed a time dependent phenomenon and depends on the rate of deformation. A time-dependent modulus such as  $G(t) = G_0 \exp\left(\frac{-t}{\lambda}\right)$  can be considered to describe the behavior of a viscoelastic fluid where  $\lambda$  is the characteristic stress relaxation time as  $\lambda \rightarrow 0$  for viscous fluids and  $\lambda \rightarrow \infty$  for elastic solids. For a time scale shorter than its characteristic relaxation time, the fluid behaves as an elastic-like solid and for the longer time scale, it acts as a viscous-like fluid. The product of deformation rate by the relaxation time of the fluid ( $\lambda\dot{\gamma} = \frac{\text{Elastic Forces}}{\text{Viscous Forces}} = \frac{\lambda}{t_{flow}}$  where  $t_{flow} \approx \frac{1}{\dot{\gamma}}$  approximates the residence time of the flow in the contraction area) results in a non-dimensional number ( $=\lambda\dot{\gamma}$  denoted as Weissenberg and Deborah numbers) that estimates the ratio of elastic to viscous stresses associated with the flow of viscoelastic fluids. Thus, this non-dimensional number was widely used to characterize the viscoelastic contraction flows in former studies.

Boger *et al.*<sup>15</sup> used a series of elastic fluids with a constant viscosity (later named as Boger fluids) and showed that the length of corner vortices increased as a function of  $\lambda\dot{\gamma}$ . Evan and Walters<sup>16,17</sup> studied the contraction flow of both shear thinning fluids and Boger fluids. Even though they reported that the length of vorticities increased as a function of  $(\lambda\dot{\gamma})$  only for the shear thinning fluids, no explanation was provided in terms of the behavioral difference between the shear thinning and Boger fluids. In another study, Boger<sup>18</sup> showed that the vortex lengths increased as a function of  $(\lambda\dot{\gamma})$  for Boger fluids with different relaxation times, but the function that defines the relation between vortex length and the  $(\lambda\dot{\gamma})$  was different for each fluid. Therefore, Boger suggested that  $\lambda\dot{\gamma}$  cannot solely describe

the flow behavior, and more than one non-dimensional number is required to characterize the viscoelastic contraction flows.

Rodd *et al.*<sup>19</sup> used the ratio of  $\lambda\dot{\gamma}$  to Re number, which resulted in a non-dimensional Elasticity number ( $El = \frac{\text{Elastic Forces}}{\text{Inertial Forces}}$ ) that indicates the ratio of elastic to the inertial stresses associated with the fluid flow. When using Boger fluids (which have a constant or nearly constant viscosity), both  $\lambda\dot{\gamma}$  and Re number have changes linearly with the applied flow rate. Thus, the El number would have a single constant value for a given fluid flowing through a given geometry. The authors characterized the contraction flows of diluted polymer solutions (Boger fluids which have a nearly constant viscosity) and attributed the difference of fluidic behaviors at comparable  $\lambda\dot{\gamma}$  to their level of elasticity (El number). For the fluid with low level of elasticity, shorter vortex lengths were reported, which was attributed to the role of the fluid inertia. In another study, Rodd *et al.*<sup>20</sup> observed that the onset of vorticities for the fluid with higher level of elasticity occurs at higher  $\lambda\dot{\gamma}$  numbers. They suggested that the higher elasticity suppressed the onset of flow instabilities. The El and  $\lambda\dot{\gamma}$  non-dimensional numbers have been used in several studies that investigated the contraction viscoelastic flows by using different polymer solutions and contraction geometries.<sup>21-26</sup> However, quite different flow behaviors were observed among those studies that showed the flow behavior cannot be solely described by using these non-dimensional numbers. For example, Lanzaro and Yuan<sup>24</sup> found that different levels of fluid elasticity can either increase or decrease the stability of the vorticities with a fixed flow geometry. In addition, the viscosity (and thus the Re number) of fluids with strong shear thinning behavior decreased at the higher shear rates. Therefore, defining a single El number did not represent accurately the elasticity of the shear thinning fluids under high

shear rates. El numbers based on the viscosity of the solutions at the corresponding shear rates associated with the contraction flow did not correlate with the length of corner vortices in contraction flows of shear thinning DNA solutions.<sup>27</sup> Therefore, it is necessary to consider a relevant non-dimensional number that is closely related with the rheology of viscoelastic solutions on their flow behavior to characterize the contraction viscoelastic flows.

Another factor that may greatly influence the viscoelastic behavior of contraction flows is the role of extension at the contraction entry. While the viscosity of the Newtonian fluids under the uniaxial extensional deformation are always three times higher than those under the shear deformation, the modulus, viscosity and the relaxation time of viscoelastic fluids vary greatly under extensional flows compared to those under shear flows. The role of extension in the contraction flow was investigated by the study of White and Baird<sup>28</sup> who found large corner vortices in their contraction flows of low density polyethylene (LDPE) melts, but they did not observe any vorticity from the contraction flow of polystyrene (PS) melts. The authors suggested that the difference between the flow behaviors was attributed to the difference of extensional characteristics between these fluids where the PS melts did not show the strain-hardening (i.e. unbounded stress growth upon startup of extensional flow) that was observed for LDPE melts. Similarly, in a study by Kang,<sup>29</sup> while the contraction flow of polyethylene oxide (PEO) solution (strain hardening fluid) showed formation and enhancement of vorticities, no vorticities were observed for the hydroxyl ethyl cellulose (HEC) solution (strain thinning fluid) under the same flow conditions. However, other than that qualitative explanations, the effects of shear and elongational deformations on the contraction flow of viscoelastic fluids are still not investigated

quantitatively.

In addition, while extensive research in this field has been conducted on polymer solutions, much less is known about the contraction flow of wormlike micellar solutions (WMS). Wormlike micelles are made by assembly of surfactants units that aggregate together by relatively weak physical attractions. The micellar structures in the equilibrium state break and reform continuously. The dynamic break and reform of WMS is the reason why that they named as living polymers.<sup>30</sup> Since WMS have advantageous characteristics over the polymer solutions, they are considered as suitable alternatives for polymeric solutions in various applications. As an example in EOR, applying high shear rates to polymer solutions will result in permanent shear degradation of polymer chains, however wormlike micelles are able to reaggregate when no more shear rate is applied.<sup>31</sup> Moreover, wormlike micelles can form flow induced structures under elongational deformation that results in a higher extensional relaxation time compare to their relaxation time under shear deformation.<sup>32</sup> Indeed, WMS with entangled wormlike micelles show strong shear thinning behavior and unique phenomena such as shear banding.<sup>33</sup> Since both elongational and shear deformations are applying to the fluids flowing through contraction geometry, our first hypothesis is that in addition to the influence of elastic stresses, the variation between extensional and shear relaxation times of WMS influence their contraction flow behavior. Second, since the shear thinning causes variation of viscosity as a function of shear rates, the velocity profiles and in turn the contraction flow behavior of WMS are influenced by their strong shear thinning flow behavior.

## **1.2. Aims and Objectives**

The aim of this study is to investigate the contraction flows of WMS, to provide

experimental information on the fluidic behavior of WMS through sudden contraction geometry. Our objective is to find a correlation between the shear and extensional relaxation times of WMS, the elastic stresses and the length of secondary flows that are observed in their contraction flow. Another objective is to quantitatively characterize the influence of shear dependent rheology of WMS on their contraction flow behavior. A microfluidic contraction geometry has been chosen to facilitate the quantitative measurement of velocity and deformation profiles by using the micro particle image velocimetry ( $\mu$ -PIV). In addition, investigating the flow at microscale enables us to study the viscoelastic flows with minimized inertial effects. The shear and extensional relaxation times of WMS are measured by shear and extensional rheological measurements and the elastic stresses were estimated by Deborah and Weissenberg non-dimensional numbers. The length of secondary flows was measured by flow visualization techniques and the correlation between the relaxation times, elastic stresses and the length of secondary flows were investigated. The velocity and shear rates of contraction flows were quantitatively measured. The measured shear rates were compared to the shear rheology curves of WMS and the influence of relevant shear viscosity and stresses of WMS on the velocity profiles were investigated.

### **1.3. Outline of Dissertation**

In Chapter 2, a background on the formation of micelles, wormlike micelles and the structural characteristics of wormlike micelles are discussed. The nonlinear rheology of viscoelastic fluids and the terms and definitions that help the clear understanding of chapters to come are introduced. Previous relevant studies on the contraction viscoelastic flows are also reviewed. Chapter 3 describes the methodological principles and

experimental apparatus that were used to characterize the shear and extensional rheology of WMS and measure the velocity and deformation rate of microscopic WMS contraction flows. The rheological characteristics of WMS are discussed in Chapter 4. Unique responses of WMS to shear and extensional deformations are investigated, and the relation of wormlike micellar structure to their linear and nonlinear rheology is discussed throughout the chapter. Chapter 5 describes the study on the contraction flows of viscoelastic WMS through a microfluidic contraction geometry. The formation and growth of secondary flows influenced by the elasticity, the response of WMS flow to the shear and extensional deformations, and the effect of nonlinear WMS rheology on the contraction flow behaviors are discussed throughout the chapter. Finally, Chapter 6 summarizes the results concerning the effects of non-Newtonian rheology and elasticity of the test fluids on their contraction flows and proposes some recommendations for future studies.

## II. BACKGROUND

### 2.1. Formation of Micellar Structures

Surfactants have amphiphilic structures that are constituted with hydrophobic tail and hydrophilic head groups.<sup>34</sup> Dissolving surfactants in an aqueous solution at a concentration higher than their critical micellar concentration (CMC) results in self-assembly of micellar structures.<sup>35</sup> The driving force for the formation of micelles is the tendency of hydrophobic tails to isolate from water while hydrophilic head groups are favored to be in contact with water molecules. In theory, the shape of micellar structures depends on the critical packing parameter ( $C_p$ ) of the surfactant molecules as follows:

$$C_p = \frac{v}{a_0 l} \quad (2.1)$$

where  $l$  and  $v$  are the length and volume of hydrophobic tail, respectively and  $a_0$  is the effective surface area of surfactant head group.<sup>36</sup> Figure 2.1 shows the expected shape of the micellar structure based on the  $C_p$  of their constituting surfactants.

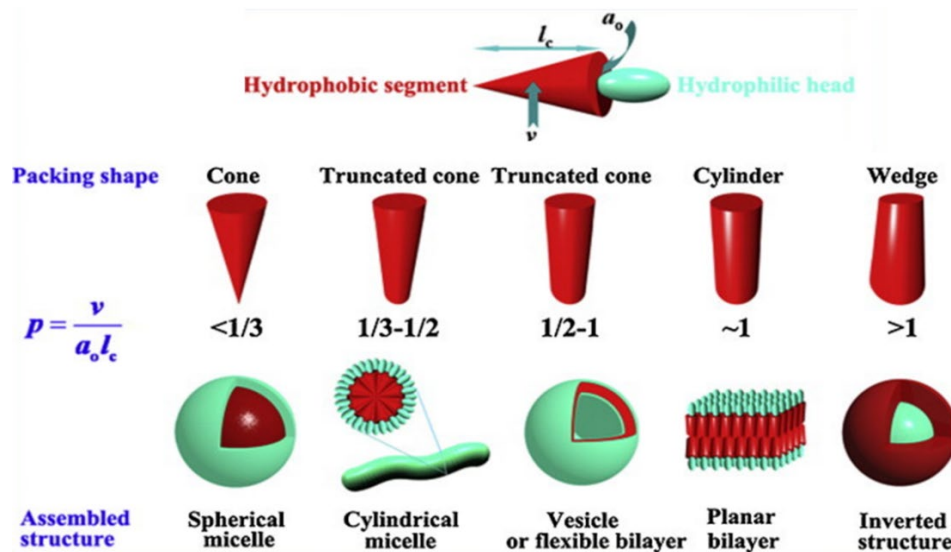


**Figure 2.1.** The effect of the packing parameter on the shape of micellar structures. Reprinted with

permission from Elsevier.<sup>37</sup>

For  $C_p < 1/3$ , surfactants are in cone shape and above their CMC, these surfactants assemble into the spherical micelles spontaneously. When the critical packing parameter is in the range of  $1/3 < C_p < 1/2$ , surfactants are expected to form cylindrical (rod-like) micelles. The micellar structures that are formed by self-assembly of surfactants with the critical packing parameters of  $1/2 < C_p < 1$  and  $C_p \sim 1$  are vesicles and bilayers, respectively.<sup>36, 38</sup> However,  $C_p$  of surfactant molecules is subjected to change by tuning the concentration of surfactant molecules in the solution.<sup>39</sup> Indeed, the presence of a co-solute in solution results in transformation of micellar structures, for example, from spherical to cylindrical structures.<sup>40</sup> Therefore, the value of  $C_p$  is only providing a prediction of micellar shape under the concentration close to the CMC,<sup>39</sup> and the shape of micellar structures may change at higher concentrations or by adding co-solutes.

## **2.2. Wormlike Micelles**

Increasing the concentration of surfactants that are assembled to form rod-like micelles spontaneously results in a significant enhancement of the zero-shear viscosity of the micellar solution.<sup>41, 42</sup> The enhanced viscosity of the solution under the higher surfactant concentration is related to the changes in microstructure of micelles. In a diluted solution, the length of rod-like micelles is shorter than the distance between micelles, so-called intermicellar distance.<sup>43</sup> The rod-like micelles have a cylindrical body with two hemispherical endcaps, in which the curvature of the cylindrical body is smaller than the curvature of endcaps. When increasing the surfactant concentration, added surfactants tend to locate in the cylindrical body of micellar structure (not in endcaps) to minimize the free energy in the solution, which results in the uniaxial growth of micellar structures.<sup>44</sup> This tendency is quantified by the endcap energy denoted as  $E_C$ , which is the excessive free energy for the

molecules located in the two hemispherical endcaps compared to those in their cylindrical body.<sup>45</sup> The growth in length of rod-like micelles results in formation of long cylindrical structures, which are termed wormlike micelles because of their shape and flexibility. Therefore, one can define the wormlike micelles as the cylindrical structures longer than the persistence length ( $l_p$ ) of cylindrical micelles. The persistence length is the longest length in which micelles act as rigid structures. The overall length of wormlike micelles is denoted as the contour length  $L$ , which can vary from nanometers to sub-micrometer length scales.<sup>46</sup> In virtue of the flexibility of wormlike micelles; the shape of wormlike micellar conformation may be found in a coil-like structure as showed in Figure 2.2.

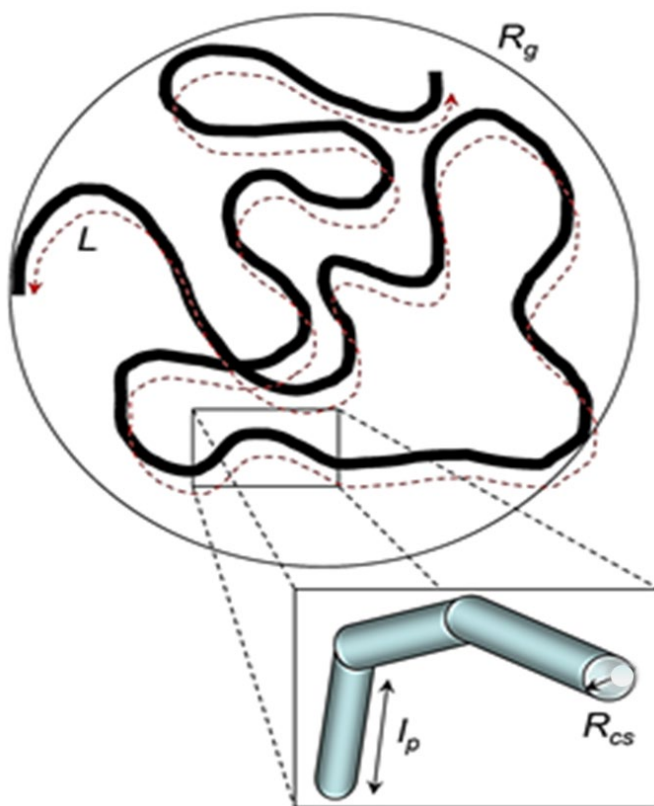


**Figure 2.2.** Schematic diagram of a wormlike micelle.  $R_g$ : radius of gyration,  $L$ : contour length,  $l_p$ : persistence length, and  $R_{cs}$ : radius of the cylinder. Reprinted with permission from Royal Society of Chemistry.<sup>40</sup>

The mean field theory developed by Cates and Candau,<sup>35</sup> is defined the relation between the average contour length ( $\bar{L}$ ) of the cylindrical micelles (neutral or highly screened micelles) and the concentration of surfactants ( $c$ ), as follows:

$$\bar{L} \sim c^{\frac{1}{2}} \exp\left(\frac{E_c}{2k_B \bar{T}}\right) \quad (2.2)$$

where  $k_B$  is the Boltzmann constant and  $\bar{T}$  is the absolute temperature. This definition is only valid for neutral micelles. For charged surfactants, headgroups repel each other, which results in cylindrical structures with shorter lengths. For charged micelles in the absence of electrolyte, the scission energy has an additional component,  $E_e$ , because of the repulsion of charges along the micellar chain backbone that favor shorter micelles. In this case the average contour length  $L$  of wormlike micelles is given by:

$$\bar{L} \sim c^{\frac{1}{2}} \exp\left(\frac{E_c - E_e}{2k_B \bar{T}}\right) \quad (2.3)$$

For concentration of surfactants that is higher than a threshold concentration ( $c^*$ ), so-called the overlap concentration, the wormlike micelles are sufficiently long to impose constraints on the movement of one another and to form entanglements with their adjacent counterparts:<sup>43, 44, 47</sup>

$$c^* = \left(\frac{k_B l_B R_{CS} v^2}{E_c}\right)^2 \quad (2.4)$$

where  $v$  is the effective linear charge density,  $l_B$  is the Bjerrum length (defined by  $l_B = e^2/\epsilon_0 k_B \bar{T}$ , where  $e$  is the elementary charge and  $\epsilon_0$  is the dielectric constant of medium (water)) and  $R_{CS}$  is the radius of the cylinder.<sup>47</sup>

Further increasing the concentration beyond  $c^*$  results in formation of longer wormlike micelles with higher number of entanglements, a “tight” network of entanglements that

account for the gel-like behavior of WMS. The formation of entanglements between wormlike micelles results in enhancement of viscosity and imparts viscoelastic characteristics to the solution. Cationic surfactants such cetyltrimethylammonium bromide (CTAB) and Cetylpyridinium Chloride (CPyCl) are known to form wormlike micellar structures. The growth of cylindrical micelles can be promoted with the addition of counterions such as hydrotropic salts.<sup>48</sup> These counterions penetrate to the area between the adjacent surfactant head groups and screen the electrostatic charge between them. Therefore, counterions that reduce the repulsion in the head groups can facilitate the uniaxial growth of cylindrical micelles (See Equations 2.3 and 2.2). WMS that are formed by dissolving CTAB and sodium salicylate (NaSal) as a counterion is one of the most studied micellar solutions. Figure 2.2 shows a schematic of micellar structure that is formed by CTAB and NaSal molecules.

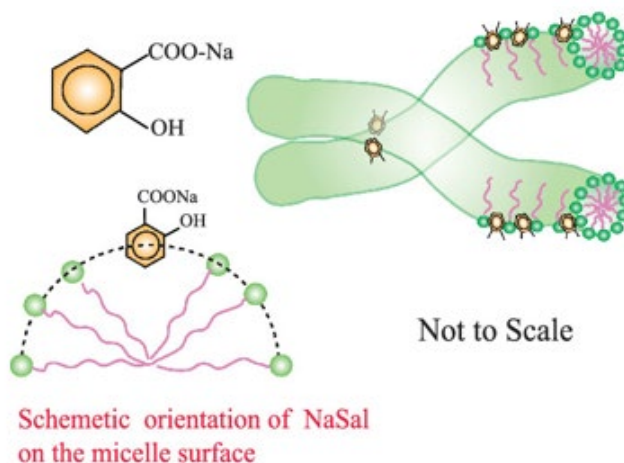


**Figure 2.3.** A schematic of CTAB/NaSal wormlike structures. Reprinted with permission from AIP Publishing.<sup>49</sup>

In wormlike micelles, surfactants units aggregate together by relatively weak physical attractions. The micellar structures in the equilibrium state break and reform continuously,

where the kinetics of breakage and reformation reactions are greatly dependent on the surfactants and salt concentrations, temperature, and flow. The dynamic break and reform of wormlike micelles is the reason why that they named as living polymers.<sup>30</sup> According to the Reptation-Reaction model,<sup>50</sup> wormlike micelles can relieve applied stresses and dissipate the imposed energy via the reversible breakdown of long micellar chains.

### 2.3. Linear Rheology of WMS

Linear rheology addresses the response of materials to the low level of stresses (or strains) where the material is subjected to reversible structural changes. The linear rheology of WMS follows the Maxwellian behavior. The Maxwell model considers a spring as an elastic element ( $\sigma_E = G\gamma_E$ ) and a dashpot as a viscous element ( $\sigma_V = \eta\dot{\gamma}_V$ ) that are connected in series to describe the viscoelastic behavior of a material. By applying a strain to the material, the sum of the strains in both elements is equals to the applied strain, and the total stress equals to the stresses in each element:

$$\gamma = \gamma_V + \gamma_E \quad (2.5)$$

$$\sigma = \sigma_V = \sigma_E \quad (2.6)$$

The derivative of the strain is an equation of state that can be used to derive the relaxation time of the material:

$$\dot{\gamma} = \frac{\sigma}{\eta} + \frac{1}{G} \dot{\sigma} \quad (2.7)$$

If we take a constant strain ( $\gamma_0$ ), then  $\dot{\gamma}$  is zero. Equation 2.7 can be simplified as:

$$0 = \frac{\sigma}{\eta} + \frac{1}{G} \dot{\sigma} \quad (2.8)$$

The analytic solution for this differential equation is:

$$\sigma(t) = G_0 \gamma_0 e^{-\frac{G}{\eta} t} \quad (2.9)$$

$$G(t) = G_0 e^{-\frac{G}{\eta}t} = G_0 e^{-\frac{t}{\lambda}} \quad (2.10)$$

The term  $\frac{\eta}{G} = \lambda$  is the characteristic relaxation time of the viscoelastic material. In order to measure the relaxation time of a viscoelastic material following the Maxwell model, the dynamic oscillatory measurement<sup>51, 52</sup> is used as described in Chapter 3.

The reason why wormlike micelles shows the similar rheological behavior with the Maxwellian fluid is their ability to break and reform continuously. In case of polymers, the chains are relaxed from the stress only by reptation, which is the self-diffusion along their contour length in a hypothetical tube that represents the constraints imposed to the movement of the polymer chain (see Figure 2.4).<sup>53</sup> In contrast, wormlike micelles are able to instantly break and change their conformation to be relaxed from the applied stress.<sup>35, 54</sup>

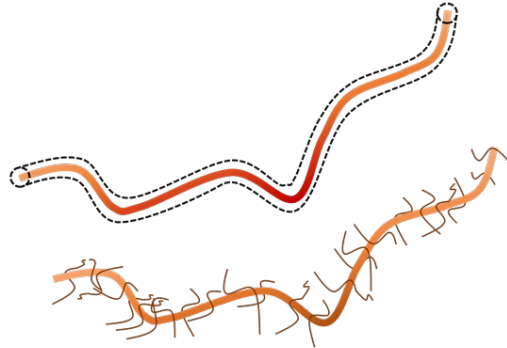


**Figure 2.4.** Schematic illustration of reptation tube.

The viscosity of WMS measured at very low deformation rate is called the zero-shear viscosity ( $\eta_0$ ), at which the structure of wormlike micelles is still intact. In case WMS are prepared by mixing surfactants and salts in water, enhanced  $\eta_0$  was reported by adding more salts.<sup>55</sup> The increase of  $\eta_0$  indicates formation of longer micelles and higher level of entanglements in the micellar network. However, adding more salts resulted in drop in  $\eta_0$  after a peak of maximum zero-viscosity of WMS (see Figure 2.5A). It has been suggested

in different ways like excessive salt ions either promoted the formation of branched wormlike micelles<sup>55, 56</sup> or resulted in shorter micellar chains.<sup>57</sup> The branched wormlike micelles at excessive salt concentrations have been observed by Gaudino *et al.*<sup>56</sup> (see Figure 2.5B). They reported that the branching points can move along the wormlike micellar chain, which act as an additional stress relaxation mechanism, thus reducing the viscosity. Branching point of wormlike micelles is different from the one of polymers in which the monomers are covalently bonded, and the branching points are fixed on the chain. A similar trend was observed when measuring the zero-shear viscosity as the salt to surfactant ratio was kept constant, but the surfactant concentration was increased.<sup>42</sup>

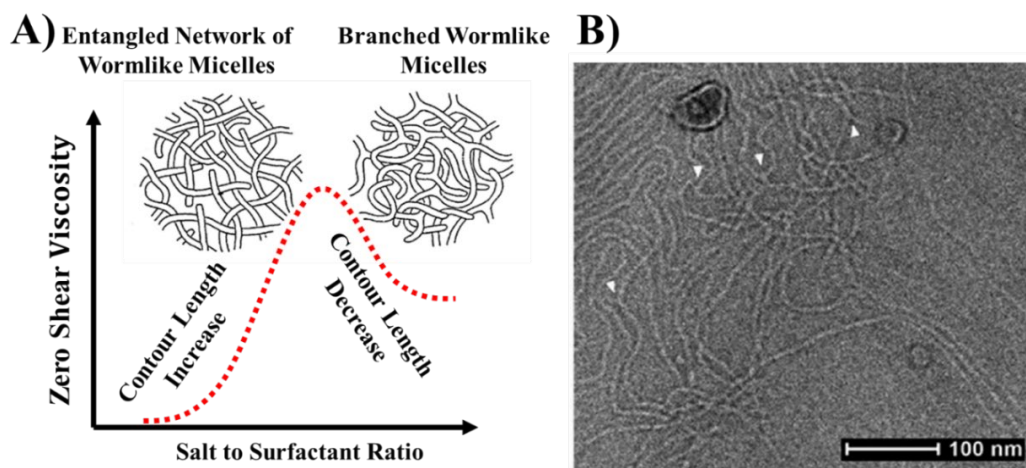


**Figure 2.5.** A) A representation of zero-shear viscosity as a function of the salt to surfactant molar ratio and structural changes in wormlike micelles (the schematic of entangled and branched wormlike micelles are adopted from Candau *et al.*<sup>55</sup>) and B) a Cryo-TEM image of wormlike micelles prepared by  $[CPyCl] = 100 \text{ mM}$  and  $[NaSal] = 90 \text{ mM}$  presented in the study of Gaudino *et al.*<sup>56</sup> The white arrows show the branch points in wormlike micelles. Reprinted with permission from AIP Publishing.<sup>56</sup>

#### 2.4. Non-linear Shear Rheology of WMS

Above the deformation range of linear viscoelasticity, structural change occurs in the

material as a result of applied deformations. In general, the power law model provides the simplest description of viscosity as a function of shear rate:

$$\eta(\dot{\gamma}) = K\dot{\gamma}^{n-1} \quad (2.11)$$

where  $K$  is the flow consistency index and  $n$  is the flow behavior index. Depending on the value of  $n$ , the fluid behavior is either shear-thinning ( $n < 1$ ), Newtonian ( $n = 1$ ), or shear-thickening ( $n > 1$ ).<sup>58</sup> The wormlike micelles show a constant shear viscosity when very low shear rates are applied, which equals to their zero-shear viscosity. The non-linear rheology of WMS is highly dependent on the structure of wormlike micelles. For entangled wormlike micelles, high deformation rates result in disentanglement of wormlike micelles, thus decreased viscosity of WMS.<sup>51</sup> The decreased viscosity of a material as a function of deformation rates is called shear thinning behavior. However, the shear thickening behavior for short wormlike micelles (and Rod-like micelles) was observed under high shear rates. Viscosity curve of a shear-thickening fluid is typically constituted of three regions: a slight shear-thinning at low shear rates, a subsequent viscosity increases over a critical shear rate, and a shear-thinning region at high shear rates.<sup>59, 60</sup> Therefore, a power law model fails to describe the fluidic behavior in the entire range of applied shear rates. For example, while a power-law model (with  $n > 1$ ) can describe the shear-thickening behavior of fluid in intermediate shear rates, it fails to fit for the regions of low and high shear rates where the fluid shows the shear-thinning (see Figure 2.6).

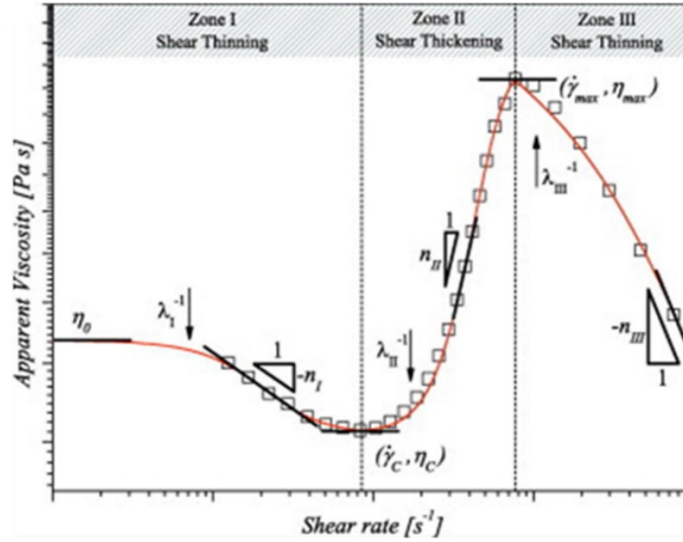


**Figure 2.6.** The three typical zones of I: shear thinning, II: shear thickening, and III: shear thinning in a log–log viscosity–shear rate curve from a shear thickening fluid. Reprinted with permission from Elsevier.<sup>61</sup>

Galindo-Rosales *et al.*<sup>61</sup> suggested a composite function by taking all regions of viscosity curve into account as follows:

$$\dot{\gamma} = \begin{cases} \eta_I(\dot{\gamma}) & \text{for } \dot{\gamma} \leq \dot{\gamma}_c \\ \eta_{II}(\dot{\gamma}) & \text{for } \dot{\gamma}_c < \dot{\gamma} \leq \dot{\gamma}_{max} \\ \eta_{III}(\dot{\gamma}) & \text{for } \dot{\gamma}_{max} < \dot{\gamma} \end{cases} \quad (2.12)$$

where  $\dot{\gamma}_c$  is the critical shear rate and  $\dot{\gamma}_{max}$  is the shear rate at which the test fluid shows the highest viscosity. The viscosity functions of  $\eta_i$  (for  $i = I, II, III$ ) are branched equations based on the cross model:<sup>62</sup>

$$\eta = \eta_\infty + \frac{\eta_0 - \eta_\infty}{1 + (\lambda\dot{\gamma})^n} \quad (2.13)$$

where  $\eta_\infty$  is the infinite shear viscosity,  $\eta_0$  is the zero-shear viscosity, and  $\lambda$  is the relaxation time of the fluid. The final forms of suggested model are derived as follows:

$$\eta(\dot{\gamma}) = \begin{cases} \eta_I(\dot{\gamma}) = \eta_c + \frac{\eta_0 - \eta_c}{1 + \left[ K_I \left( \frac{\dot{\gamma}^2}{\dot{\gamma} - \dot{\gamma}_c} \right) \right]^{n_I}} & \text{for } \dot{\gamma} \leq \dot{\gamma}_c \\ \eta_{II}(\dot{\gamma}) = \eta_{\max} + \frac{\eta_c - \eta_{\max}}{1 + \left[ K_{II} \left( \frac{\dot{\gamma} - \dot{\gamma}_c}{\dot{\gamma} - \dot{\gamma}_{\max}} \right) \dot{\gamma} \right]^{n_{II}}} & \text{for } \dot{\gamma}_c < \dot{\gamma} \leq \dot{\gamma}_{\max} \\ \eta_{III}(\dot{\gamma}) = \frac{\eta_{\max}}{1 + [K_{III}(\dot{\gamma} - \dot{\gamma}_{\max})]^{n_{III}}} & \text{for } \dot{\gamma}_{\max} < \dot{\gamma} \end{cases} \quad (2.14)$$

where  $K_i$  (for  $i = I, II, III$ ) are the time constant parameters,  $n_i$  (for  $i = I, II, III$ ) are the dimensionless exponents that are related to the slope of the each power-law regime,  $\eta_c$  is the viscosity of fluid at the critical shear rate, and  $\eta_{\max}$  is the viscosity of fluid at  $\dot{\gamma}_{\max}$  (see Figure 2.6). The proposed model describes well both shear-thinning (either for  $\dot{\gamma} \leq \dot{\gamma}_c$  or  $\dot{\gamma}_{\max} < \dot{\gamma}$ ) and shear-thickening ( $\dot{\gamma}_c < \dot{\gamma} \leq \dot{\gamma}_{\max}$ ) regimes that were observed in the viscosity curve of a shear-thickening fluid.<sup>59, 61</sup> However, a number of independent constants used in its derivation is a drawback of this model.

## 2.5. Shear Induced Structures

Shear-thickening of WMS is attributed to the shear-induced gelation that formed by long micellar chains.<sup>63</sup> In this approach, gelation occurs when the applied shear rate is high enough, i.e., above a critical shear rate  $\dot{\gamma}_c$ , to overcome the rotational Brownian diffusion ( $D_r$ ) of the rod-like micelles:

$$\dot{\gamma}_c \sim D_r \sim \frac{k_B T}{\pi L^3 \eta_s} \quad (2.15)$$

where  $\eta_s$  is the viscosity of the solvent. Barentin and Liu<sup>64</sup> presented a new mechanism for the formation of shear-induced structure, in which the micelles collide under the shear flow and aggregate into bundles. Unlike the approach explaining the shear-induced gelation by overcoming the Brownian diffusion, they concluded that shear-induced gelation is attributed to micellar–micellar interactions. This shear-induced state is called alternatively

shear-induced phase (SIP)<sup>65</sup> or shear-induced structure (SIS)<sup>66</sup>. Rehage and Hoffmann<sup>42</sup> observed that an aqueous WMS of CPyCl/NaSal formed a gel-like structure along the direction of shear flow above a critical shear rate. This gel-like structure is referred to as SIS, a structure that will disintegrate with the cessation of the shear flow.<sup>42, 67</sup> The general rheological response of the CPyCl/NaSal solution under the Couette flow condition confirms that the formation and disbanding of SIS increases and decreases the viscosity of the solution, respectively. The formation of SIS occurs when a flow regime causes a stretching and tumbling of wormlike micelles, which invoke micelle–micelle collisions that produce a complex viscous network. Rojas et al.<sup>67</sup> revealed that while it is not possible for short micelles to form long-range connections under static conditions, these connections can be elongated by imposing an appropriate level of shear stress.

## **2.6. WMS Under Extensional Flow**

The behavior of viscoelastic fluids that are under the extensional deformation depends on both the extensional rate and the total strain that are applied to the fluid. While the extensional viscosity of a Newtonian fluid is always three times higher than its shear viscosity, the viscoelastic fluids show a significant deviation from this relation. In case of the extensional flow, polymers may stretch in the direction of flow. Conformational changes of polymer chains from their coil-like structure at equilibrium to the stretched state require a large amount of applied stress. Therefore, the coil-to-stretch transition is considered as the underlying reason for that very high ratio of extensional viscosity to shear viscosity was observed in some polymer fluids (e.g. high Trouton ratio).<sup>68, 69</sup> A theoretical study by Larson and Magda predicted that the coil-to-stretch transition in polymer chains occurred when they are subject to high extension rate and enough strain.<sup>68</sup> Thus, the

Hencky strain indicating the total strain applied to the fluid over the time is an important factor for the study of elongational flow:<sup>70, 71</sup>

$$\varepsilon(t) = \int_0^t \dot{\varepsilon}(t) dt \quad (2.16)$$

where  $\dot{\varepsilon}$  is the extension rate. Compared to polymer solutions, the elongational flow of WMS is much less understood. Bhardwaj *et al.*<sup>72</sup> measured the extensional rheology of WMS prepared by CTAB/NaSal and CPyCL/NaSal. For both solutions, the extensional viscosity has increased as a function of Hencky strains and reached to a constant value for sufficiently high Hencky strains. The increased extensional viscosity of solutions is attributed to the coil-to-stretch transition in wormlike micelles. The authors found that solutions of lower  $C_d$  showed more strain hardening behavior. Sachsenheimer *et al.*<sup>32</sup> found considerably longer extensional relaxation time for CTAB/NaSal solutions of  $R = \frac{[NaSal]}{[CTAB]} < 1$  compared to their shear relaxation time. The authors suggested that longer relaxation time in the elongational flow must be a result of an elongation induced structure (EIS) formed in WMS. Omidvar *et al.*<sup>73</sup> studied the shear and extensional rheology of WMS prepared by dissolving hexadecyltrimethylammonium p-toluenesulfonate (CTAT) in deionized water. At lower concentrations, these WMS showed strain hardening behavior, and the maximum extensional viscosities were  $\sim 10^5$  times higher than their zero-shear viscosity. At higher concentrations, the Trouton ratio has dropped to an ultimate value of  $Tr \sim 3$ . The authors concluded that the higher extensional viscosities observed at low concentrations was caused by formation of EIS. However, the ratio of extensional to shear relaxation times reported in their study was lower than unity for all concentrations<sup>73</sup> in contrast to the study by Sachsenheimer *et al.* In summary, extensional flow of the WMS

promises rich fluid dynamics associated with structural changes that necessitates further investigations.

## 2.7. Contraction Viscoelastic Flows

A contraction flow is associated with non-homogenous extension rates along the centerline area of contraction entry and shear flows elsewhere<sup>11</sup>. Formation of large secondary flow is observed for the viscoelastic contraction flow that is not observed for Newtonian contraction flows (see Figure 2.7). As discussed in Section 1.1, the effect of elasticity on the fluidic behavior was investigated in literature by using non-dimensional numbers that quantify the ratio of elasticity to viscous and inertial stresses associated with the flow. However, these non-dimensional numbers could not fully characterize the viscoelastic contraction flows. Flow transitions and formation secondary flows were reported to occur at different range of those non-dimensional numbers using different viscoelastic fluids or at different range of concentrations for the same viscoelastic fluid. In addition, the secondary flows were not reported for the viscoelastic fluids that does not (does or does not ??) show strain hardening characteristics.<sup>60, 74</sup> The formation of vorticities is known to result in a lower extension rate in the upstream of contraction entry, and thus is considered as a stress relief method for the fluid flowing toward the contraction entry.<sup>75, 76</sup> The flow patterns observed with diluted to semi-diluted polymer solutions in the previous literatures<sup>21-26</sup> can be categorized as follows: Newtonian-like flow, formation and enhancement of lip/corner vorticities, and unsteady and time dependent flows. The transitions of flow patterns were dependent on the value of  $\lambda\dot{\gamma}$ .

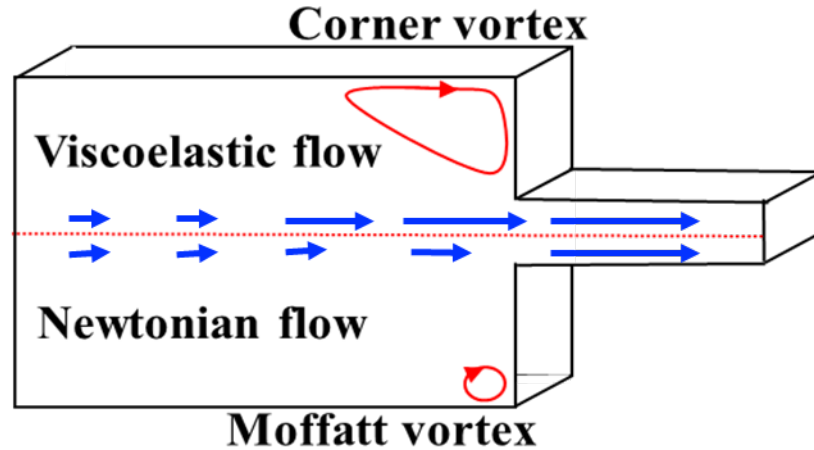


**Figure 2.7.** A Schematic diagram of a sudden contraction geometry illustrating the secondary flows observed with Newtonian and viscoelastic fluid flows.

As discussed in this chapter, various Non-Newtonian phenomena that are associated with the structural changes in the viscoelastic fluids occur at high deformation rates. Moreover, the viscoelastic fluids show unique response to the extensional flow comparing to shear flow, which is not reflected in the non-dimensional numbers. In order to better understand the viscoelastic contraction flows, the effect of these phenomena on the fluidic behavior should be investigated.

### III. CHARACTERIZATION METHODS AND EXPERIMENTAL APPARATUS

This chapter provides a description of the methodological principles and experimental apparatus that are used to characterize the structure of wormlike micelles, the viscoelastic properties, and the flow behavior of wormlike micellar solutions (WMS). Section 3.1 describes the rheological characterization methods that are employed to study WMS. Rheology is the science of studying flow and deformation of materials to elucidate the interrelation between force, time and deformation<sup>77</sup>, which determines the mechanical properties of the materials. The dynamic oscillatory shear rheometry experiments (Section 3.1.1) provide insight to the structure of wormlike micelles. The small amplitude of strain that is applied to test fluids in dynamic oscillatory test does not deform the structure of wormlike micelles. Thus, the characteristics of micelles that are measured in this method reflect the structural properties of wormlike micellar chains in their equilibrium state. Steady shear experiments (Section 3.1.2) are used to measure the viscosity and shear stress of the test fluids. It is possible to obtain the fluid properties in both linear and nonlinear state by changing the shear rate from very low to high. The extensional rheometry (Section 3.1.3) is used to measure the characteristics of wormlike micelles, when the fluid is subjected to extension. Section 3.2 describes the flow visualization techniques that are used to characterize the flow behavior of WMS. Fluorescent streak imaging (Section 3.2.1) technique is used to document the flow pattern of WMS in the microfluidic device. Section 3.2.2 describes the micro-particle image velocimetry ( $\mu$ -PIV) that is used for quantitative velocity measurements of microscopic flows.

### 3.1. Rheological Characterization

#### 3.1.1. Dynamic Oscillatory Measurements

As one of dynamic oscillatory measurements that is widely used to obtain information about structural properties of viscoelastic solutions, the small amplitude oscillation shear (SAOS) test is used to determine the structural properties of WMS. In SAOS test, a small sinusoidal shear strain applies to the fluid:

$$\gamma(t) = \gamma_0 \sin(\omega t) \quad (3.1)$$

where  $\gamma_0$  is the strain amplitude and  $\omega$  is the angular frequency. The resulting stress from the fluid response is measured as a function of time:

$$\sigma(t) = \sigma_0 \sin(\omega t + \delta) \quad (3.2)$$

where  $\sigma_0$  is the stress amplitude and  $\delta$  is the phase shift with respect to the applied strain. The stress data can also be analyzed by decomposing the stress sinusoidal term into two terms, one in the phase with the strain ( $\sin \omega t$ ) and the other one in the  $90^\circ$  out of phase with the strain ( $\cos \omega t$ ):

$$\sigma(t) = \gamma_0 (G'(\omega)\sin(\omega t) + G''(\omega)\cos(\omega t)) \quad (3.3)$$

where  $G'(\omega)$  and  $G''(\omega)$  are considered as the elastic modulus and loss modulus of the viscoelastic solution, respectively. The elastic modulus is proportional to the stress in-phase with the applied strain and indicates the elasticity of material. The loss modulus is proportional to the stress out of phase with the applied strain and indicates the energy loss due to the viscous dissipation in material.<sup>78</sup>

Since wormlike micelles break and reform continuously, they show a single shear relaxation time ( $\lambda$ ) and their dynamic rheology follows the Maxwell model where their elastic modulus ( $G'$ ) and loss modulus ( $G''$ ) can be described as:

$$G'(\omega) = \frac{G'_0 \omega^2 \lambda^2}{1 + \omega^2 \lambda^2} \quad (3.4)$$

$$G''(\omega) = \frac{G'_0 \omega \lambda}{1 + \omega^2 \lambda^2} \quad (3.5)$$

Therefore,  $\lambda$  of WMS can be obtained as the reciprocal of the  $\omega$  at the crossover point of  $G'$  and  $G''$ <sup>35,79</sup>.

Rheological properties of each solution were characterized using a stress-controlled rheometer (HAAKE iQ rheometer, Thermo Scientific) (see Figure 3.1A). The temperature of test fluid is controlled by using an isothermal bath (Isotemp, Fisher Scientific) coupled to the rheometer. A geometrical setup of parallel plates with 60 mm diameter is used to measure elastic and loss moduli ( $G'$  and  $G''$ , respectively) under the SAOS mode.

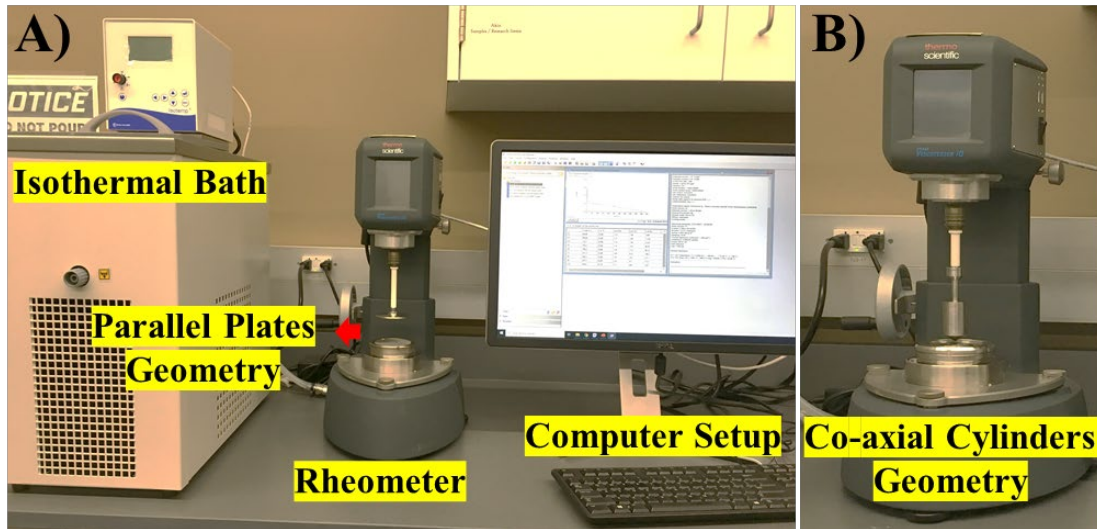


**Figure 3.1.** A) The experimental setup for dynamic shear oscillatory measurements. B) Shows the co-axial cylinders geometry setup that is used for steady shear measurements.

### 3.1.2. Steady Shear Measurements

Steady shear measurements provide the information about the shear viscosity,  $\eta(\dot{\gamma})$  and shear stress,  $\sigma(\dot{\gamma})$  of viscoelastic solutions as a function of the imposed shear rate. The viscosity of non-Newtonian fluids is defined by the ratio of shear stress to the shear rate:

$$\eta = \frac{\sigma}{\dot{\gamma}} \quad (3.6)$$

Rotational rheometers are developed to measure the shear viscosity of fluids. In these rheometers, a rotor rotates at a certain angular velocity ( $\Omega$ ) to apply a defined amount of shear rate to the fluid and the torque ( $M$ ) on the rotor axis is measured:

$$\dot{\gamma} = K_{\gamma}\Omega \quad (3.7)$$

$$\sigma = K_{\sigma}M \quad (3.8)$$

where  $K_{\gamma}$  and  $K_{\sigma}$  are strain and stress constants that are geometry-dependent factors. For a co-axial cylinder geometry setup, the values of  $K_{\gamma}$  and  $K_{\sigma}$  depend on the radius of the outer stationary cylinder ( $R_o$ ), and length ( $L_i$ ) and radius of rotating inner cylinder ( $R_i$ ) as follows<sup>80, 81</sup>:

$$K_{\gamma} = \frac{R_o^2}{R_o^2 - R_i^2} \quad (3.9)$$

$$K_{\sigma} = \frac{1}{2\pi L_i R_o^2} \quad (3.10)$$

Therefore, the viscosity and shear stress can be derived by substituting these constants in equations (3.6-8). In this study, shear viscosities and shear stresses of solutions are measured at a wide range of shear rates using a cylinder with 12.54 mm radius and a cup with 13.60 mm radius. WMS shows a constant shear viscosity at small shear rates (i.e.  $\dot{\gamma} \ll 1$ ) and this viscosity value is considered as the zero-shear viscosity ( $\eta_0$ ) of the solution.

### 3.1.3. Extensional Rheometry

The extensional rheometry has been used for characterizing viscoelastic fluids by tracking the thinning process of their stretched filament. For example, in a capillary break up (CaBER) rheometer, a fluid sample is placed between the two plates of the CaBER

rheometer (see Figure 3.2A). As the upper plate moves upward with an initial step-strain and, an unstable liquid bridge is formed between the two plates. The liquid bridge gets thinner over time until its pinch-off (Figure 3.2B). The filament thinning dynamics depend on the interplay of capillary, inertia, viscous and elastic forces. The capillary is the driving force for the thinning of filament whereas the rest of forces counteract against it. Depending on the relative magnitude of inertia, viscous and elastic forces, several scaling laws have been established to describe the thinning dynamics of fillaments.<sup>72, 82, 83</sup> Therefore, the thinning phenomena of the filament can be analyzed to characterize the extensional rheology of the fluid. While the CaBER rheometry has been widely used to characterize extensional rheology of fluids, recent reports suggested that the initial step-strain (upper plate moving upward) could disrupt the microstructure and alter the viscosity and relaxation time of the fluid.<sup>32, 82</sup> Recently, Dinic et. al.<sup>83-86</sup> introduced the dripping-onto-substrate (DOS) method to characterize the extensional rheology of fluids. In DOS method, a droplet of fluid is pumped from a vertical needle that is placed at a certain distance ( $H$ ) above a glass substrate (Figure 3.2C). Once the droplet contacted with the substrate, a fluid filament is formed which shows thinning over time (Figure 3.2D) akin to CaBER experiment.<sup>82, 84</sup>

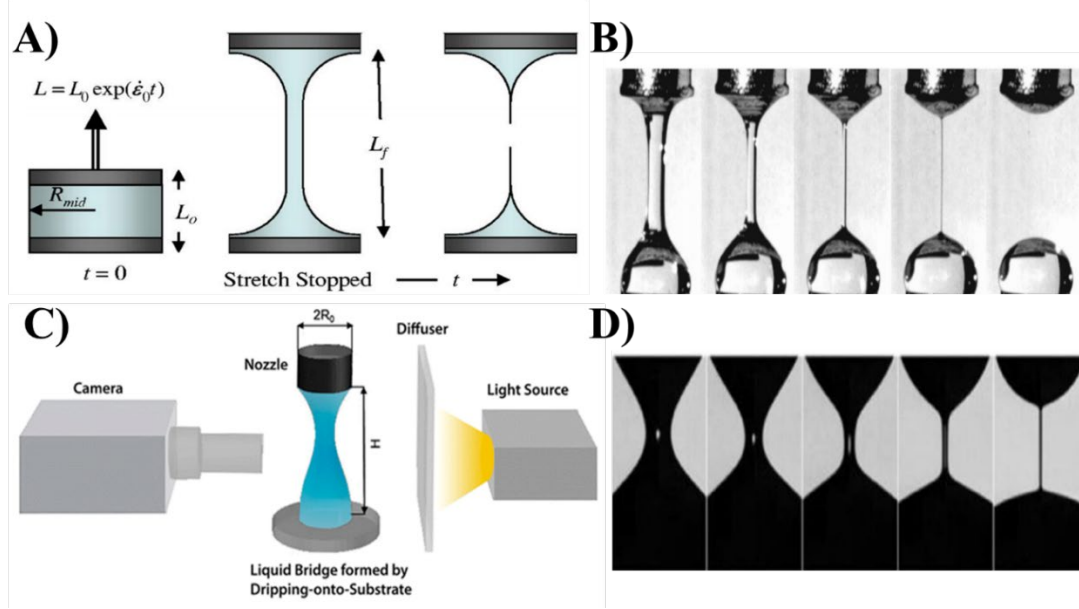


**Figure 3.2.** A) A schematic illustration of CaBER rheometer. Reprinted with permission from AIP Publishing.<sup>72</sup> B) An example of filament thinning of a fluid observed from a CaBER rheometry experiment. Reprinted with permission from AIP Publishing.<sup>72</sup> C) A schematic illustration of DOS rheometry setup. Reprinted with permission from Royal Society of Chemistry.<sup>84</sup> D) An example of filament thinning of a fluid observed from a DOS rheometry experiment. Reprinted with permission from American Chemical Society.<sup>87</sup>

The thinning dynamics that is dominated by inertial and capillary forces is described by an inertia-capillary scaling equation<sup>86, 88</sup>:

$$\frac{D(t)}{D_0} = 0.8 \left( \frac{t_{ic} - t}{t_R} \right)^{\frac{2}{3}} \quad (3.11)$$

where  $t_{ic}$  is the pinch-off time,  $D_0$  is the initial diameter of liquid bridge, and  $t_R$  is the Rayleigh time, a characteristic time scale that is calculated by:

$$t_R = \left( \frac{\rho R_0^3}{\Gamma} \right)^{\frac{1}{2}} \quad (3.12)$$

where  $\Gamma$  is the surface tension of the fluid and  $R_0$  is the initial radius of the liquid bridge.

If viscous and capillary forces dominate on filament thinning dynamics, the phenomena is described by an visco-capillary scaling equation<sup>86, 89</sup>:

$$\frac{D(t)}{D_0} = 1 - 0.07 \left( \frac{t}{t_{VC}} \right) \quad (3.13)$$

where  $t_{VC}$  is the visco-capillary time, a characteristic time scale that can be calculated as:

$$t_{VC} = \left( \frac{\eta R_0}{\Gamma} \right) \quad (3.14)$$

For viscoelastic solutions, after a time of  $t_C$ , the elastic and capillary forces dominate on the thinning dynamics of the filament. In the elasto-capillary thinning regime, the radius of the fluid filament decays exponentially over time. The equation provided by Entov and Hinch<sup>90</sup> described the electro-capillary thinning dynamics as:

$$\frac{D(t)}{D_0} \approx \left( \frac{GR_0}{2\Gamma} \right)^{\frac{1}{3}} e^{\left( \frac{-t}{3\lambda_E} \right)} \quad (3.15)$$

where  $G'$  is the elastic modulus and  $\lambda_E$  is the extensional relaxation time of the solution. Therefore, by plotting the  $D(t)/D_0$  as a function of time in a semi-logarithmic scale, the elasto-capillary region appears as a linear line. The extensional relaxation of a solution is then obtained by fitting the diameter data in the elasto-capillary region with an equation in the form of:

$$\frac{D(t)}{D_0} = A e^{-Bt} \quad (3.16)$$

where  $B$  is equivalent to  $1/3\lambda_E$ . In the elasto-capillary thinning regime, the elastic stress ( $\sigma_E = \eta_E \dot{\epsilon}$ , where  $\eta_E$  is the extensional viscosity and  $\dot{\epsilon}$  is the extension rate) counteracts against the capillary stress,  $2\Gamma/D(t)$ , which is the driving force for thinning of filament. Therefore, the extensional viscosity of the fluid can be derived as:

$$\eta_E = \left( \frac{2\Gamma}{\dot{\epsilon} D(t)} \right) \quad (3.17)$$

The Hencky strain  $\epsilon(t)$  is the total strain experienced by the fluid in a stretched filament

that is defined as:

$$\varepsilon(t) = 2\ln\left(\frac{D_0}{D(t)}\right) \quad (3.18)$$

Therefore, the extension rate is calculated by derivation of equation 3.18:

$$\dot{\varepsilon}(t) = -2\frac{d\ln\left(\frac{D(t)}{D_0}\right)}{dt} \quad (3.19)$$

By substituting equation 3.19 into equation 3.17, the extensional viscosity can be obtained as:

$$\eta_E = \left(\frac{-\Gamma}{\frac{dD(t)}{dt}}\right) \quad (3.20)$$

In order to calculate the extensional viscosity, Anna and McKinley<sup>91</sup> suggested to fit the data of  $D(t)/D_0$  with a fitting equation in the form of:

$$\frac{D(t)}{D_0} = Ae^{-Bt} - Ct + D \quad (3.21)$$

where A, B, C and D are fitting parameters. The derivative form of this fitting equation is subsequently used in equations 3.17 and 3.19 to compute the extensional viscosities.

Figure 3.3A shows the experimental setup that was used to characterize the extensional rheology of WMS. The experiments have been carried out using a contact angle and surface tension measurement instrument (First Ten Angstroms, Inc., Portsmouth, VA).

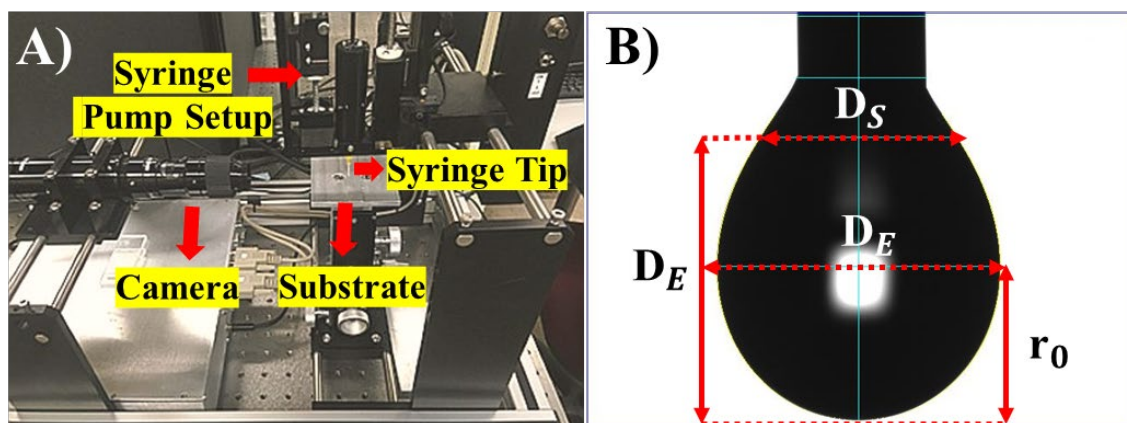


**Figure 3.3.** A) The experimental setup for extensional rheology measurement. B) Pendant drop of a test fluid with an illustration of geometrical parameters that are used to calculate the surface tension.

The test fluids were loaded in a 5 mL gas-tight syringe (Hamilton, Reno, NV) and the syringe were placed into the syringe pump of the instrument (See Figure 3.3A). A gauge 20 syringe tip with the outer diameter (OD) of 0.9081 mm was mounted to the syringe while a glass substrate is placed under the syringe. The vertical distance between the tip of syringe and the substrate is adjusted at  $H \approx 3.5$  mm. Test fluids were gently pumped out with a very low flow rate ( $1 \mu\text{L/s}$ ), and the pumping were stopped once the droplet touches the substrate. The filament thinning of test fluid are then recorded with a CCD Camera (GigE Vision, Imprex, Inc., Milwaukee, WI) with the frame rates of 5-60 frame per seconds (fps). After the series of captured images were converted to binary images using ImageJ (NIH), the binary images were processed with a MATLAB code<sup>86, 92</sup> to measure and track the change of the filament diameter over time. The initial diameter of all filaments is considered as  $D_0 = 0.9081$  mm that equals to the OD of the syringe tip. Further, the normalized diameter of filaments,  $D(t)/D_0$  was plotted as a function of time using SigmaPlot (version 12.0, Systat Software Inc, San Joe, CA). The curve fit function of SigmaPlot is used for fitting the data points with equations 3.16 and 3.21. In order to

calculate the extension rates, the obtained fitting parameters from equation 3.21 were substituted to the derivation form of equation 3.21 using Microsoft Excel. Finally, to calculate the extensional viscosities using equation 3.17, the surface tension of the test fluids has been measured.

### 3.1.3.1. Surface Tension Measurement

Analysis of pendant drop shape was used to measure the surface tension ( $\Gamma$ ) of the test fluids. The contribution of the gravitational force and the surface tension ( $\Gamma$ ) of a liquid to the shape of a pendant drop is described by Young-Laplace equation<sup>93</sup>:

$$\Gamma = \frac{\Delta\rho g r_0^2}{\beta} \quad (3.22)$$

where  $\Delta\rho$  is the density difference between the liquid and its carrier phase, i.e. air in this study,  $g$  is the gravitational acceleration constant,  $r_0$  is the radius of curvature at the drop apex (See Figure 3.2B), and  $\beta$  is the non-dimensional shape factor. The shape factor,  $\beta$  is related to  $D_E/D_S$ , where  $D_E$  is the maximum diameter of the penant drop and  $D_S$  is the diameter of the drop at the distance of  $D_E$  from the apex, which can be calculated using the following equation provided by Hansen and Rødsrud<sup>93</sup>:

$$1 = 0.12836 - 0.7577 \left(\frac{D_E}{D_S}\right) + 1.7713 \left(\frac{D_E}{D_S}\right)^2 - 0.5426 \left(\frac{D_E}{D_S}\right)^3 \quad (3.23)$$

Therefore, the surface tension of the liquid can be calculated by characterizing the shape of pendant drop and obtaining  $r_0$  and  $\beta$ . The surface tension measurement instrument shown in Figure 3.3A calculated the geometrical parameters and returned the surface tension of each test fluid.

## 3.2. Flow Visualization

A fluorescence microscope (IX73, Olympus) equipped with a high-speed camera (NX4-

S2, IDT) was used to visualize and capture flow patterns of WMS. The microscopic flow of WMS influenced by the contraction entry was visualized using fluorescent streak imaging and micro-particle image velocimetry ( $\mu$ -PIV). For the fluorescent flow visualization techniques, test fluids were seeded with 0.02 %wt of 2.0  $\mu\text{m}$  diameter red fluorescent particles (ex/em = 542/612 nm, Thermo Scientific). A mercury lamp for continuous illumination and a filter cube (49008-BX3, Olympus) that filtered the appropriate range of wavelengths were used to excite the fluorescent particles and images from excited fluorescent particles are recorded by the high-speed camera.

### **3.2.1. Fluorescent Streak Imaging**

In fluorescent streak imaging technique, acquired images from a fluid flow at a defined condition were overlaid by a software (*i.e.* ImageJ (NIH)). The constructed image by overlaying the images shows the pathlines of tracing particles over the entire time period of image acquisition. For each volumetric flow rate, a series of 300 frames ( $1024 \times 1024$  pixels, 8-bit grayscale) with the acquisition rate of 200 to 600 fps was captured at the center plane ( $z = 0$ ) of the microchannel using 4X or 10X objectives. For each set of experiments, series of 100 to 300 frames were overlaid using the maximum intensity function of ImageJ (NIH).

### **3.2.2. Micro-Particle Image Velocimetry ( $\mu$ -PIV)**

Micro-particle image velocimetry ( $\mu$ -PIV) is used for quantitative measurements of a velocity field with a spatial resolution of only a few micrometer scale. In PIV measurements, acquired images are processed by a cross-correlation algorithm. After the algorithm divides each image to  $k$  interrogation areas with a size of  $p \times q$  pixels, it computes the displacement vector of seeded particles for each interrogation window between the two

sequential images using the peak value of correlation function. Given the time interval between the two images and the displacement vector of particles, the local velocity vector can be calculated. To increase the resolution of vector fields, a multi-pass approach when choosing the interrogation windows can be employed, in which the vector fields are calculated using interrogation windows that are reduced in size for each pass. The displacement vectors resulting from the first pass are interpolated to the smaller spatial resolution, and the interrogation area of the second pass is shifted by the interpolated vectors before the second pass correlation. The result of each pass is used to shift the interrogation windows during the next pass, therefore the resolution and accuracy of displacement vectors are improved<sup>94</sup>.

Two sets of experiments were conducted for  $\mu$ -PIV analysis: (i) For the low volumetric flow rates,  $0.05 \text{ mL/h} < Q < 0.5 \text{ mL/h}$ , a series of 200 frames ( $1024 \times 1024$  pixels, 8 bits) was captured with the rate of 200 fps using a 4X objective. The captured frames were then used to generate 100 pairs of sequential frames; (ii) For the high volumetric flow rates,  $Q > 0.5 \text{ mL/h}$ , a 10X objective was used after positioning the field of view at the upstream corner of the contraction entry in order to investigate fluid dynamics of secondary flows. For each set of experiments, a series of 300 frames was captured at the center plane with the acquisition rate of 600 fps and used to generate 150 pairs of sequential frames. A particle-tracking tool built for MATLAB<sup>95</sup> was used to reconstruct the velocity field of the fluid flow. The built-in PIVlab (version 2.31, developed by Dr. William Thielicke and Prof. Eize J. Stamhuis, published under the BSD and CC-BY license) cross-correlation function was used to compare interrogation areas between pairs of sequential frames with the multi-pass interrogation method in three passes with windows sizes of  $64 \times 64$ ,  $32 \times 32$ , and 16

× 16 pixels, respectively. A mean velocity field is generated for each experiment by averaging the velocity fields of sequential frames. The shear and strain rate profiles were generated based on the mean velocity field frame using PIVlab.

## IV. RHEOLOGY OF WORMLIKE MICELLAR SOLUTIONS

### 4.1. Introduction

The most relevant modeling of viscoelastic solutions is to consider these materials as a two-component system, one with a pure “elastic” property connected to the other one with a pure “viscous” property. Such a model, so called the Maxwell model<sup>96</sup> introduced by James Clerk Maxwell, considers a spring connected with a dashpot in series, which is the basis for understanding of viscoelastic response of solutions. In nature, no material shows the viscoelastic behavior as simple as predicted by Maxwell model, but the linear viscoelasticity of wormlike micellar solutions (WMS) can be described outstandingly with the model.<sup>51, 97</sup> The Maxwell model predicts a mono-exponential decay of the stress in viscoelastic fluid, which is characterized by a single relaxation time ( $\lambda$ ). The close agreement of WMS linear viscoelasticity to the Maxwellian flow is attributed to the ability of wormlike micelles to break and reform continuously. The reaction-reptation model introduced by Cates<sup>35, 50, 54</sup> incorporates the reptation relaxation mechanism of entanglements that was developed for polymers<sup>53</sup> with the reversible scission of the wormlike micelles, which successfully describes the Maxwellian behavior of WMS. Therefore, rheological characterization of WMS provides valuable information about the microscopic structure of wormlike micelles and its relation to the macroscopic flow behavior of WMS. The nonlinear viscoelastic behavior of WMS when there are structural changes in the material is associated with phenomena such as shear thinning that commonly observed for viscoelastic solutions and several unique phenomena such as shear thickening<sup>64, 98-100</sup> and shear banding.<sup>101-103</sup> In this chapter, thorough rheological characterization of WMS is aimed to study the structure of wormlike micelles, the non-

linear phenomena associated with WMS flows, and correlation between these phenomena and the microscopic structure of wormlike micelles. The second section of this chapter (Section 4.2) provides the theoretical background on the structure of wormlike micelles and its relationship with the rheological parameters. In Section 4.3, the rheological characterization of test fluids that were used to study the microscopic flow of WMS is presented. Additionally, since there are growing applications of WMS such as in seawater super cavitation desalination techniques<sup>104, 105</sup> and enhanced oil recovery (EOR)<sup>31, 106, 107</sup>, a complementary study regarding the effect of temperature and water salinity (NaCl) on the rheology of WMS is provided in Section 4.4.

## 4.2. Theoretical Background

Wormlike micelles break and reform continuously in a solution and show viscoelastic properties with a single relaxation time ( $\lambda$ ):

$$\lambda \sim \sqrt{\lambda_r \lambda_b} \quad (4.1)$$

where  $\lambda_b$  and  $\lambda_r$  are micellar reversible breaking and reptation relaxation times of wormlike micelles, respectively.<sup>108, 109</sup> When the kinetics of reversible breaking of micellar chains dominates over the timescales for reptation of micellar chains, micellar solutions show the Maxwellian behavior and the Cole-Cole plot ( $G''$  against  $G'$ ) of WMS showing a semicircle trace.<sup>35, 79</sup> However, at high frequencies where the  $\omega$  is in order of  $\frac{1}{\lambda_b}$ , the rheology of WMS behavior deviates from the Maxwellian behavior and the wormlike micelles show an upturn in their  $G''$  and  $G'$ .<sup>49</sup> The value of local minimum of  $G''$  over the plateau modulus ( $G'_0$ ) of WMS is giving an estimate for the number of entanglements on the average micellar contour length  $\bar{L}$ :

$$\frac{G''_{\min}}{G'_0} \approx \frac{l_e}{L} \quad (4.2)$$

where  $l_e$  is the entanglement length, which is the length of micellar chains in the intervals between the two entanglement points,<sup>110</sup> that can be derived from:

$$l_e \approx \frac{\xi_m^{\frac{5}{2}}}{l_p^{\frac{3}{2}}} \quad (4.3)$$

where,  $l_p$  is the persistence length, which is the length that micellar chains act as rigid entities. The parameter  $\xi_m$  is the network mesh size that can be estimated from plateau modulus  $G'_0$ <sup>79, 110</sup>:

$$G'_0 \approx \frac{k_B \check{T}}{\xi_m^3} \quad (4.4)$$

where  $k_B$  is the Boltzmann constant and  $\check{T}$  (K) is the absolute temperature. The length scales associated with the wormlike micellar network are illustrated in Figure 4.1.

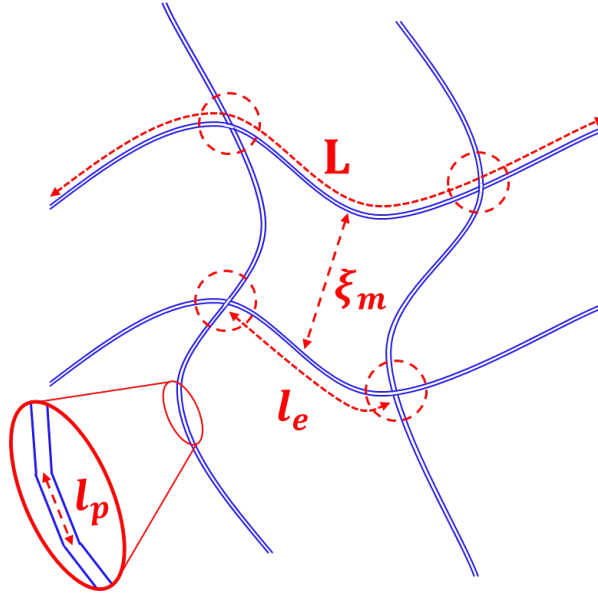


**Figure 4.1.** A schematic illustration of wormlike micellar network with entanglements (shown in dashed circles).  $l_e$  is the entanglements length,  $L$  is the contour length of micellar chains,  $\xi_m$  is the network mesh size, and  $l_p$  is the persistence length.

### 4.3. Rheological Characterization of Test Fluids

#### 4.3.1. Preparation of Test Fluids

Cetyltrimethylammonium bromide (CTAB) is a cationic surfactant with 16 atoms of carbon in its backbone, which forms micellar structures when its concentration is higher than the critical micellar concentration (CMC = 0.9 mM).<sup>72, 111</sup> In the presence of salts such as sodium salicylate (NaSal), the electrostatic repulsion between the charged head groups of CTAB is abated by oppositely charged counterions (i.e. COO<sup>-</sup> in NaSal) and wormlike micelles can be formed even at highly diluted concentrations of the surfactant<sup>112</sup> (See Figure 4.2). The solution of CTAB/NaSal is one of the widely studied WMS, and various factors contributing to its rheological and flow behavior have been investigated.<sup>113-117</sup> Azzouzi *et al.*<sup>118</sup> studied the effect of salt (NaSal) concentration ( $10 \text{ mM} \leq C_s \leq 1 \text{ M}$ ) on the rheological behavior of CTAB/NaSal solutions with a fixed surfactant (CTAB) concentration ( $C_d = 50 \text{ mM}$ ). While they observed solutions showed shear thickening behavior for  $10 \text{ mM} \leq C_s \leq 18 \text{ mM}$ , the viscosity of solutions decreased as a functional of higher shear rates (shear thinning) for higher  $C_s$  concentrations. However, since  $R$  provides only an estimate of how much counterions are available per surfactant molecule, it is more appropriate to consider the molar ratio of salt to surfactant concentration ( $[\text{NaSal}]/[\text{CTAB}] = R$ ) than  $C_s$ . Kim and Yang<sup>119</sup> studied the rheology of CTAB/NaSal solutions for  $1 \leq R \leq 10$  with a given  $C_d$  and reported that the relaxation time of solutions decreased at higher  $R$ . Vasudevan *et al.*<sup>117</sup> studied the CTAB/NaSal solutions with  $0.18 \leq R \leq 0.34$  and  $C_d = 50, 70, \text{ and } 90 \text{ mM}$ . The authors reported that the zero-shear viscosity of solutions increased with higher  $R$  and  $C_d$ , and the shear thickening behavior was limited to diluted solutions (i.e. at  $R \leq 0.32$  for  $C_d = 50 \text{ mM}$  and  $R \leq 0.22$  for  $C_d = 90 \text{ mM}$ ). For higher surfactant (and

salt) concentrations, the length of wormlike micelles increases, and entanglements are formed between the micelles. The entangled wormlike micelles cannot align by the flow to show the shear thickening behavior. Instead, as the concentration increase and more entanglements form, shear thinning behavior become more prominent. Therefore, if the lower concentration among the test fluids is chosen based on the limit of shear thickening behavior, and the rest of test fluids is prepared with higher concentrations, a range of structures from short to highly entangled wormlike micelles can be investigated. In this study, the molar ratio of salt to surfactant has been kept constant at  $R = 0.32$ , and five different surfactant concentrations,  $C_d = 50, 62.5, 75, 87.5,$  and  $100$  mM were selected for the preparation of test fluids. The lower limit of concentration,  $C_d = 50$  mM with  $R = 0.32$ , was chosen based on the limit of shear thickening behavior observed by Vasudevan *et al.*<sup>117</sup>. The higher limit of concentration,  $C_d = 100$  mM with  $R = 0.32$ , was selected based on the study of Cardiel *et al.*<sup>120</sup>, in which a highly entangled network of wormlike micelles were observed and the relaxation time of the solution was 2 orders of magnitude higher than that of  $C_d = 50$  mM solution.

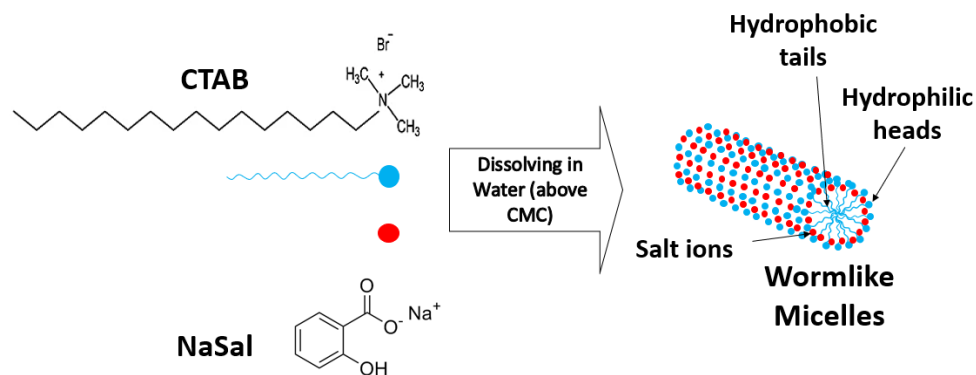


**Figure 4.2.** Schematic diagram for the formation of wormlike micelles.

To prepare each test fluid, appropriate amounts of CTAB and NaSal (Provided in Table

4.1) were added to DI water and the solution were mixed by using a magnet stirrer for 4 hours. The test fluids then were left for at least 48 h to ensure that the wormlike micelles reached to their equilibrium state.

**Table. 4.1.** Molar concentrations and rheological properties of test solutions.

[CTAB] (mM)	[NaSal] (mM)	$R = \frac{[NaSal]}{[CTAB]}$	$\lambda$ (s)	$\lambda_E$ (s)	$\lambda_E / \lambda$	$\eta_0$ (Pa·s)
100	32	0.32	6.1	7.57	1.2	120
87.5	28	0.32	1.35	4.69	3.5	21
75	24	0.32	0.23	3.47	15	3.5
62.5	20	0.32	0.06	1.82	30.3	0.53
50	16	0.32	0.02	1.18	59.3	0.03

#### 4.3.2. Dynamic Oscillatory Shear Measurements

In order to determine the relaxation times ( $\lambda$ ) of solutions, the elastic ( $G'$ ) and viscous ( $G''$ ) moduli of WMS ( $R = 0.32$ ,  $50 \text{ mM} \leq C_d \leq 100 \text{ mM}$ ) were plotted as a function of angular frequency ( $\omega$ ) (see Figure 4.3). The relaxation time for the solution of  $C_d = 50 \text{ mM}$  was determined as  $0.02 \text{ s}$  ( $\lambda = 1/\omega$  when  $G' = G''$ ), and the duration of the relaxation time increased with the solutions of higher  $C_d$  as the relaxation time was  $6.1 \text{ s}$  for the solution of  $C_d = 100 \text{ mM}$ . The longer relaxation time is attributed to the formation of longer wormlike micelles with higher density of entanglements as a result of higher  $C_d$ .

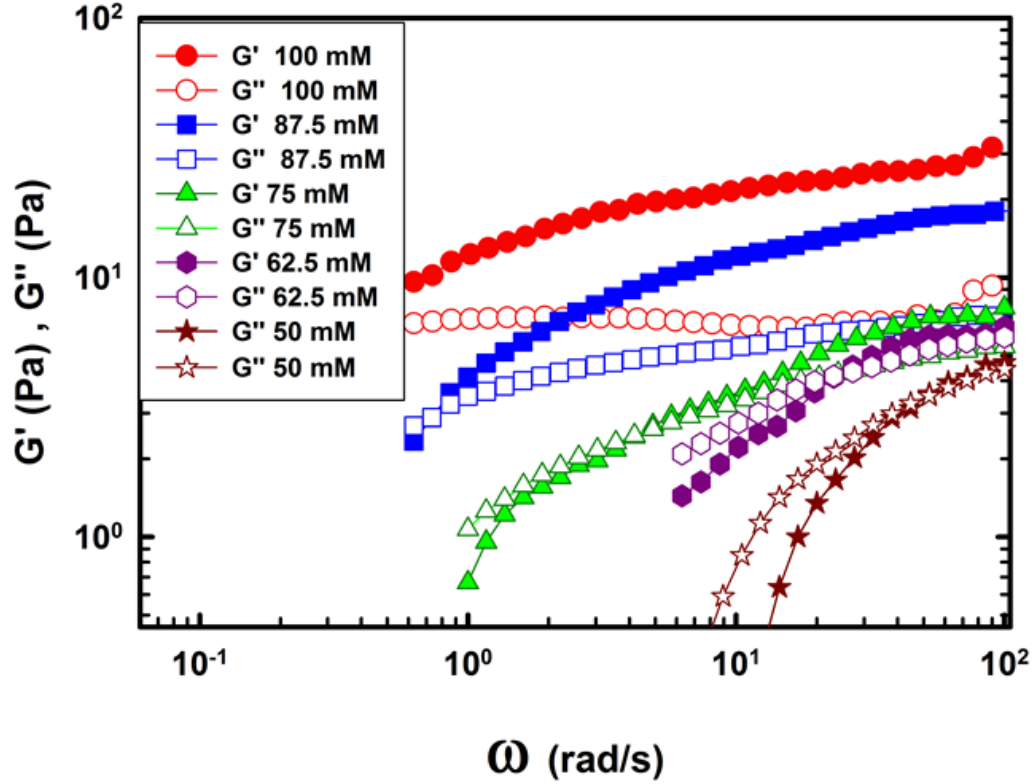


**Figure 4.3.** Elastic and viscous moduli ( $G'$  and  $G''$ ) as a function of angular frequency.

The solutions with lowest and highest  $C_d$  used for this study were previously visualized by Cardiel *et al.*<sup>120</sup> using Cryo-TEM (Figure 4.4). At  $C_d = 50$  mM, a few individual micellar chains with an average contour length of  $\bar{L} = 350$  nm were observed that they were barely overlapped with a network mesh size of  $\xi_m \approx 300$  nm. In contrast, highly entangled bundles of micelles in the solution of  $C_d = 100$  mM were observed with a mesh size of  $\xi_m \approx 47$  nm. Similarly, Vasudevan *et al.*<sup>117</sup> also reported that for CTAB/NaSal solutions ( $0.18 \leq R \leq 0.34$ ,  $50 \text{ mM} \leq C_d \leq 90 \text{ mM}$ ), increasing  $C_d$  resulted in formation of longer micellar chains for a given fixed  $R$ .

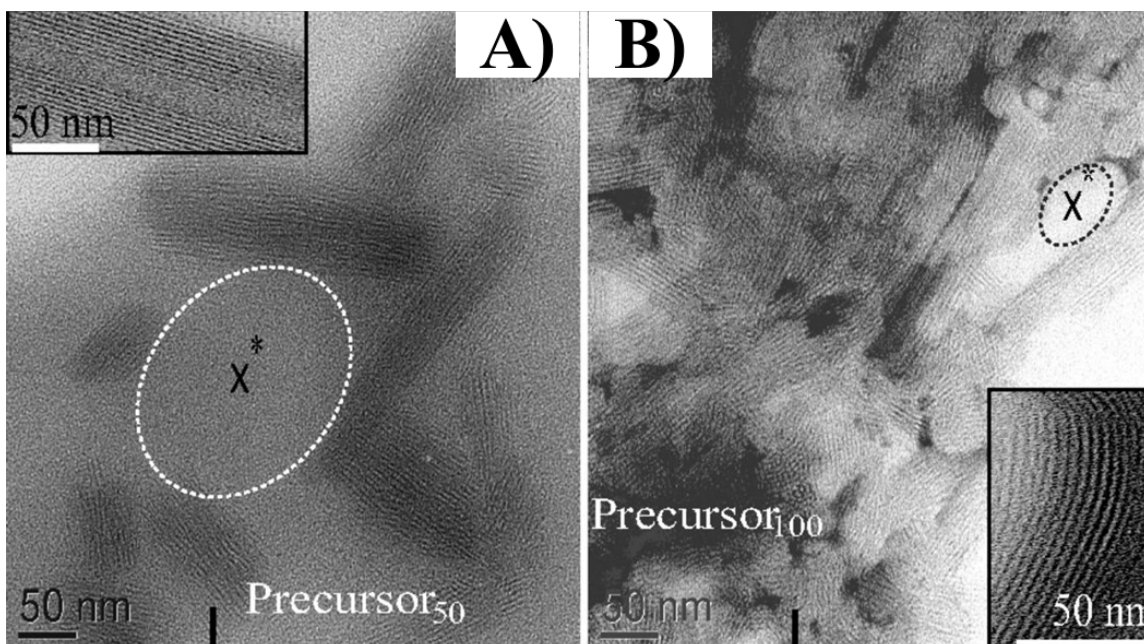


**Figure 4.4.** TEM Images of A)  $C_d = 50$  mM and B)  $C_d = 100$  mM ( $x^*$  in both images represents the network mesh size). Copyright (2013) National Academy of Sciences.<sup>120</sup>

### 4.3.3. Steady Shear Measurements

Figure 4.5 shows the measured shear viscosity as a function of shear rates for each solution. For high  $C_d$  solutions (100, 87.5, and 75 mM), the initial viscosity plateau (so called Newtonian plateau) were observed at low shear rates ( $\dot{\gamma} \ll 0.1$ ). The value of viscosity in the plateau region is considered as zero-shear viscosity ( $\eta_0$ ) when the micellar structures remain intact from the applied shear rates.

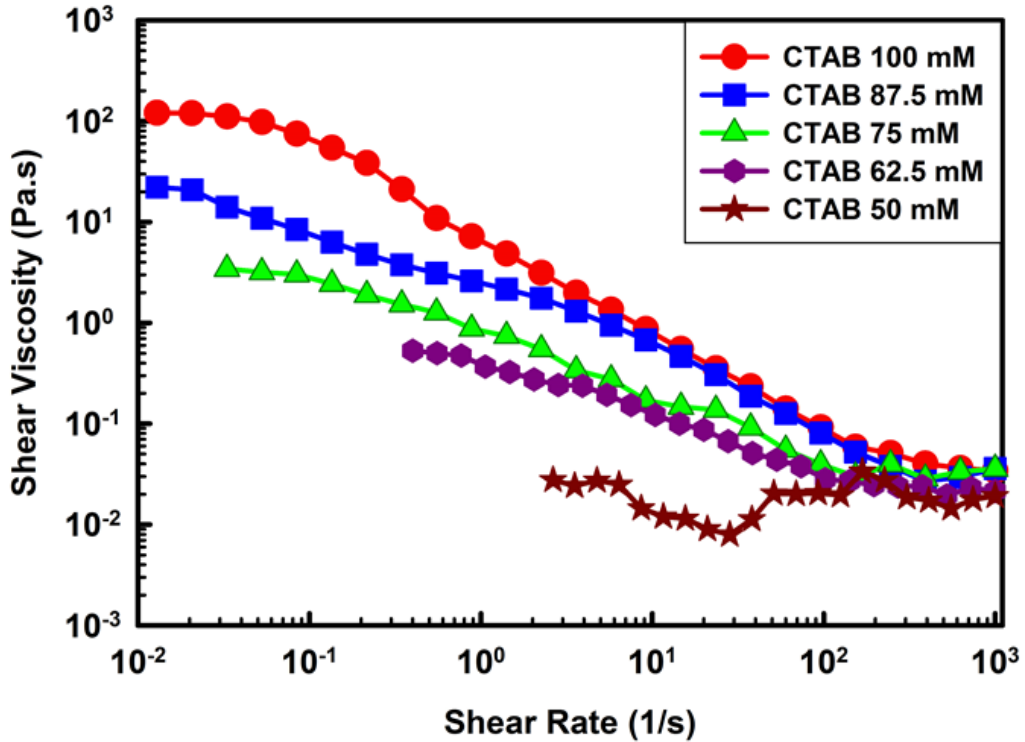


**Figure 4.5.** Measured shear viscosities as a function of shear rates.

For low  $C_d$  (62.5 and 50 mM) solutions, it was not possible to measure the viscosity of fluids at low shear rates due to the lack of sensitivity of the rheometer. Therefore, the value of viscosity at the lowest examined shear rate were considered as the zero-shear viscosity. The measured zero-shear viscosity of 0.03 Pa·s for  $C_d = 50$  mM solution showed good agreements with the results obtained from micro-rheometry of the same solution in previous studies ( $\eta_0 = 0.008$  Pa·s<sup>120, 121</sup> and  $\eta_0 = 0.03$  Pa·s<sup>117</sup>).

Test solutions for  $C_d \geq 62.5$  mM showed a shear thinning behavior at the intermediate shear rates, which followed by a second plateau near the highest range of shear rates. In the shear thinning region, increased shear rate disentangled and shortened micellar bundles, which resulted in lower viscosity. Hence, a strong shear thinning behavior is an indicator of the high viscoelasticity and dense entanglements in the solution. For  $C_d = 100$  mM solution,

the zero-shear viscosity of 121 Pa·s is 4 orders of magnitude higher than that of  $C_d = 50$  mM solution ( $\eta_0 = 0.03$  Pa·s). Such a high zero-shear viscosity represents that significant entanglements occurred in the micellar network, which increased the resistance for the solution to flow.

The second plateau of the viscosity that was observed near the highest shear rates occurs when all the entanglements are eliminated, and only individual rod-like micelles remained in the fluid. Thus, ultimate viscosities ( $\eta_\infty$ ) for all solutions are close to each other at the value of  $\eta_\infty \approx 0.03$  Pa·s, in which the minor difference is due to the higher population of micelles at the higher surfactant concentrations  $C_d$ . Lastly, a slight shear thickening was observed for  $C_d = 50$  mM solution, which is attributed to the formation of shear induced structures (SIS).<sup>122, 123</sup> In SIS, rod-like micelles align in the direction of shear flow and form a transient structure that resulting in increased viscosity.<sup>122, 124</sup>

Figure 4.6 shows the shear stresses as a function of shear rates for each solution. A stress plateau is evident for solutions with  $C_d \geq 75$  mM, where the shear stress is independent of shear rates. The stress plateau observed in the shear stress-strain rate curve,  $\sigma(\dot{\gamma})$ , is a rheological signature for the shear banding behavior of WMS. In the shear banding, homogenous flow of WMS separates spatially into two coexisting regions with different local viscosities: i) a high viscous local region with entangled micellar structures and ii) a low viscous local region with linearly aligned micelles.<sup>125</sup> It is considered that these high and low local viscosities in the shear bands are coexisted at the equal shear stress, and their volume fractions are changed to match the imposed macroscopic shear rate.<sup>126</sup>

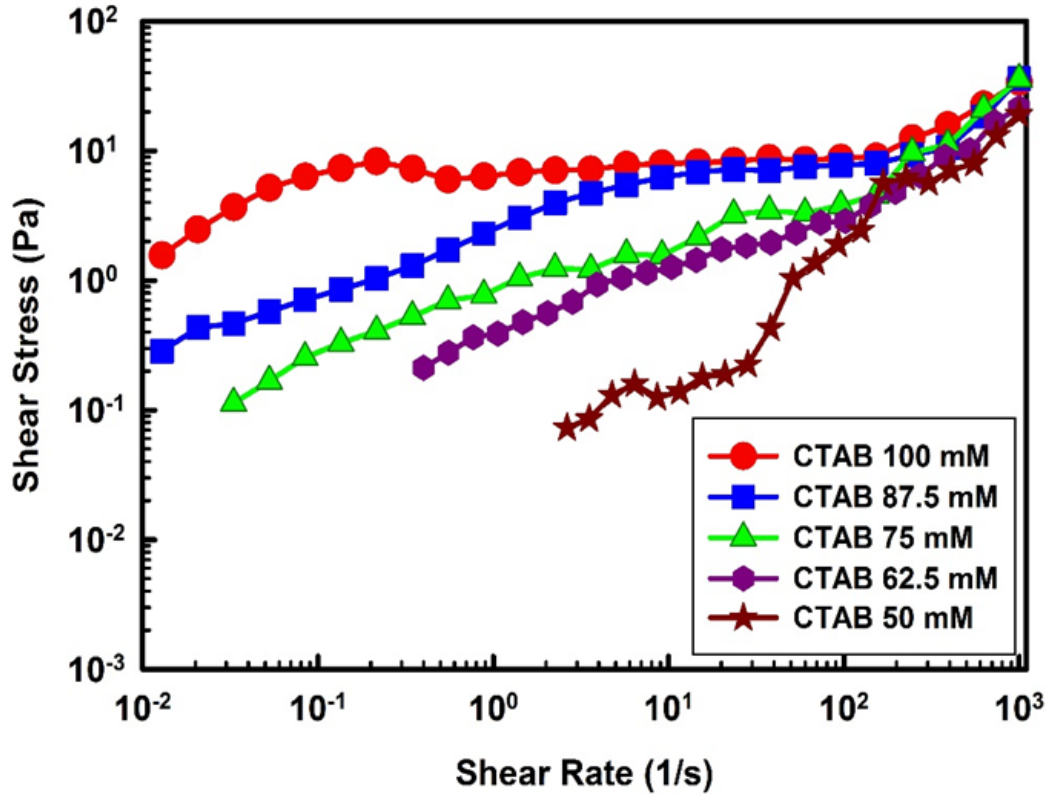


Figure 4.6. Measured shear stresses as a function shear rates.

#### 4.3.4. Extensional Relaxation Times

Figure 4.7 shows the thinning of filaments for the WMS ( $R = 0.32$ ,  $50 \text{ mM} \leq C_d \leq 100 \text{ mM}$ ). The normalized filament diameter ( $D(t)/D_0$ ) are plotted as a function of time in Figure 4.8. The profiles showed the initial sharp decrease of diameter, but the thinning slope got less steep after a certain time period of  $t_c$  by the onset of elasto-capillary thinning dynamics. The inset of Figure 4.8 shows the diameter of filaments that was shifted by their  $t_c$  and normalized with its filament lifetime ( $t_f$ ).

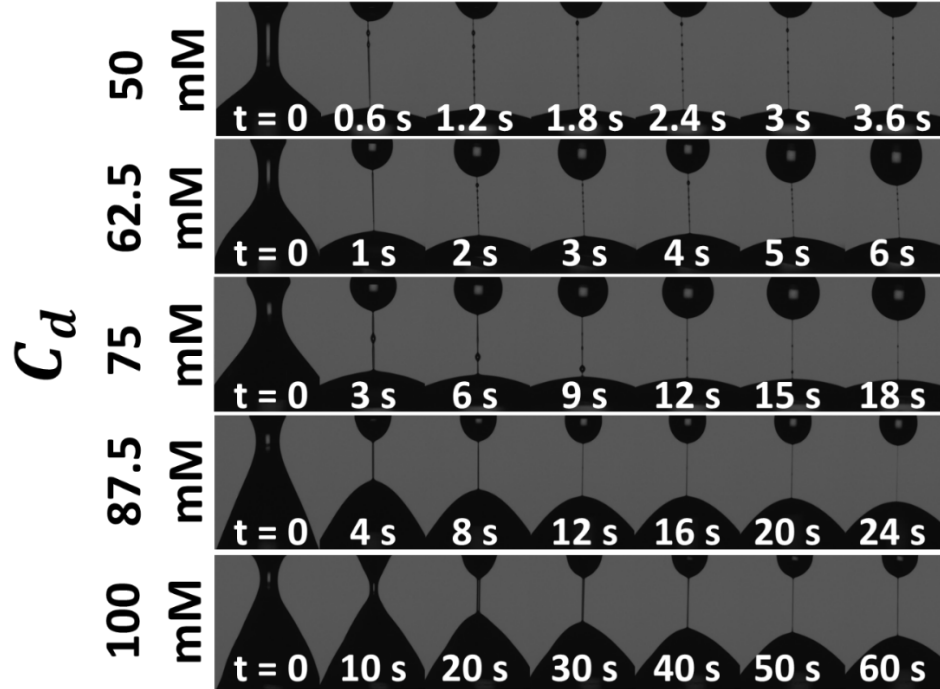


Figure 4.7. The thinning of filament over time for different CTAB concentration ( $R = 0.32$ ,  $50 \text{ mM} \leq C_d \leq 100 \text{ mM}$ ).

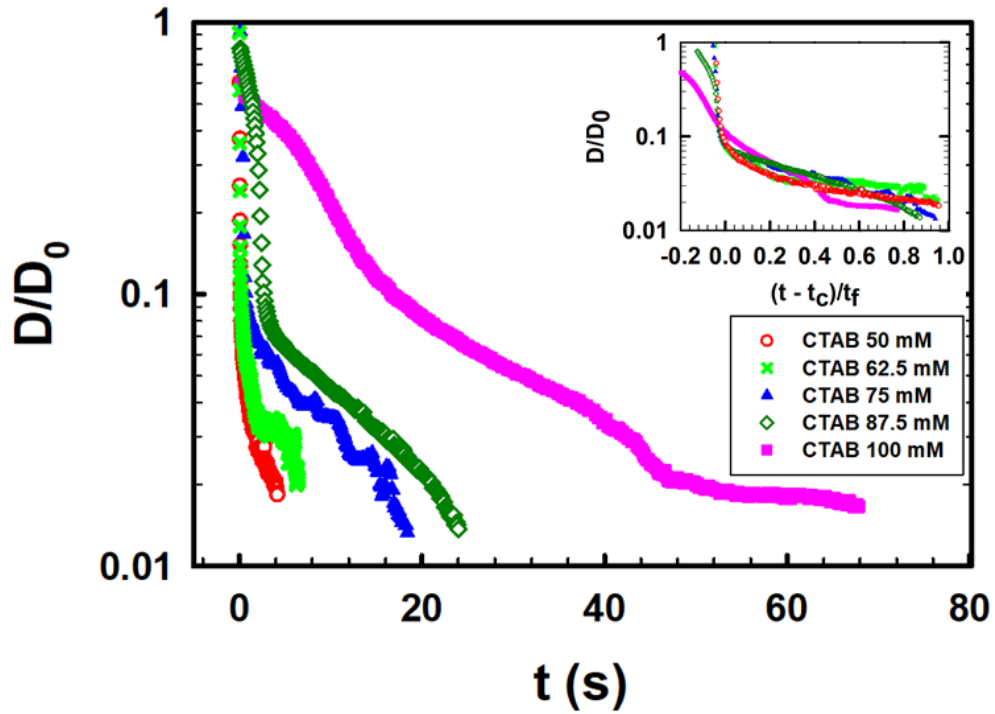
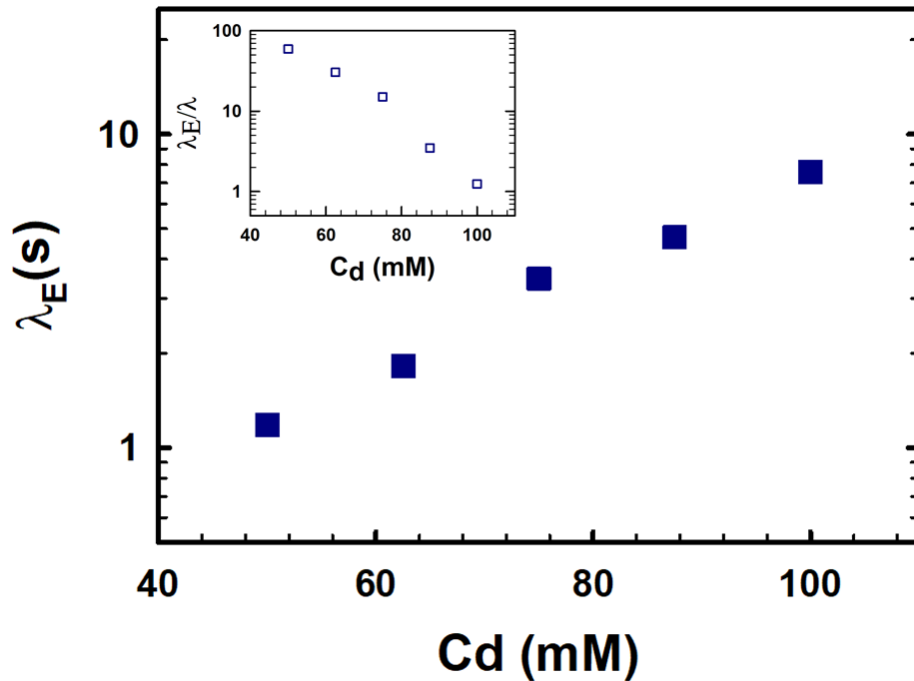


Figure 4.8. Normalized filament diameter profiles as a function of time. The inset shows the profiles against the normalized time  $(t-t_c)/t_f$ .

The filament diameter of each solution in the elasto-capillary regime ( $t - t_c > 0$ ) is fitted by equation 3.17, and the extensional relaxation times were obtained (Figure 4.9). The relaxation time increased with higher  $C_d$  solutions due to the formation of longer wormlike micelles and higher levels of entanglements in the micellar network. However, the ratio of extensional relaxation time ( $\lambda_E$ ) to the shear relaxation time ( $\lambda$ ) that was obtained from shear oscillatory measurements decreased significantly with higher  $C_d$  solutions (see inset of Figure 4.9). The ratio ( $\lambda_E/\lambda$ ) was found to be around the unity for the solution of  $C_d = 100$  mM, which showed no difference in the relaxation time for the solution when it was subjected to either elongation or the shear force. However, we found that the relaxation time ratio increased to around 60 with the lower  $C_d$  solution of 50 mM. The results agree with the previous study on CTAB/NaSal solution ( $C_d = 25$  mM,  $0.5 \leq R \leq 5.2$ ) by Sachsenheimer *et al.*<sup>32</sup> that reported high values of  $\lambda_E/\lambda$  for solutions with  $R < 1$ . The authors reported that while the relaxation time ratio is fixed around 1 for the test solutions of  $R > 1$ ,  $\lambda_E/\lambda$  increased with lower  $R$ , for example when  $R = 0.5$   $\lambda_E/\lambda$  was found to be around 10. It was suggested that a form of micellar structures built up in the solutions of  $\lambda_E/\lambda > 1$  under the extensional mode. The micellar structure is so called elongation induced structure (EIS), which is the main reason for the fluid to yield significantly higher relaxation times.<sup>32, 82</sup> In present study, test fluids with  $R = 0.32$  that have lower  $R$  than the minimum  $R$  ( $R = 0.5$ ) studied by Sachsenheimer *et al.*<sup>32</sup> were investigated and showed even higher values of  $\lambda_E/\lambda$  ( $\approx 60$  at  $C_d = 50$  mM). Indeed, we observed that the  $\lambda_E/\lambda$  decreased to  $\sim 1$  for higher  $C_d$  solutions, which is related to the higher levels of entanglements. Considering the formation of EIS as the main reason for high ratio of relaxation times, the micellar chains should align along the elongation direction to form EIS structure, which is

prevented by entanglement points. Another phenomenon that may be attributed to the relaxation time of solutions in the elongation flow is known as the coil/stretch transition.<sup>72</sup> In an equilibrium state, wormlike micellar chains are considered to have a coil-like structure.<sup>40</sup> In the elongational flow, the micellar chains stretch in the direction of elongation, in turn the coil-stretch transition is considered as the main reason for the strain hardening of wormlike micelles. For higher  $C_d$  solutions, the micellar chains were entangled to each other in tight networks. Therefore, the extensibility of wormlike micellar chains is limited to the length of micelles between the entanglements.<sup>73</sup> Thus, there is no significant change in their structure compared to the one in their equilibrium state. In contrast, for lower  $C_d$  solutions, micellar chains can fully stretch in the direction of flow, which may indeed facilitate their alignment along the flow direction to form EIS.



**Figure 4.9.** Extensional relaxation time ( $\lambda_E$ ) as a function of CTAB concentration ( $C_d$ ). The inset image shows the ratio of relaxation times ( $\lambda_E/\lambda$ ) as a function of  $C_d$ .

#### 4.3.5. Extensional Viscosities

The measured extensional viscosities ( $\eta_E$ ) are plotted as a function of Hencky strain in Figure 4.10. For all solutions,  $\eta_E$  increased with higher surfactant concentration,  $C_d$ , which is attributed to the formation of longer and more entangled wormlike micelles at higher surfactant concentrations ( $C_d$ ). The extensional viscosities of all WMS increased with Hencky strain (strain hardening) and reached to a constant ultimate value of  $\eta_{E,\infty}$ . The strain hardening is attributed to the transition in wormlike micelles from their coil/equilibrium state to stretched chains in the direction of elongation. At high Hencky strains where wormlike micellar chains/networks reach to their maximum extensibility, the elastic stress could no longer grow to resist against the capillary pressure and the solution reaches to its constant ultimate extensional viscosity ( $\eta_{E,\infty}$ ). We also noted that the strain hardening is more prominent at lower  $C_d$ , which can be explained by the role of extensibility and formation of EIS discussed in Section 4.3.4.

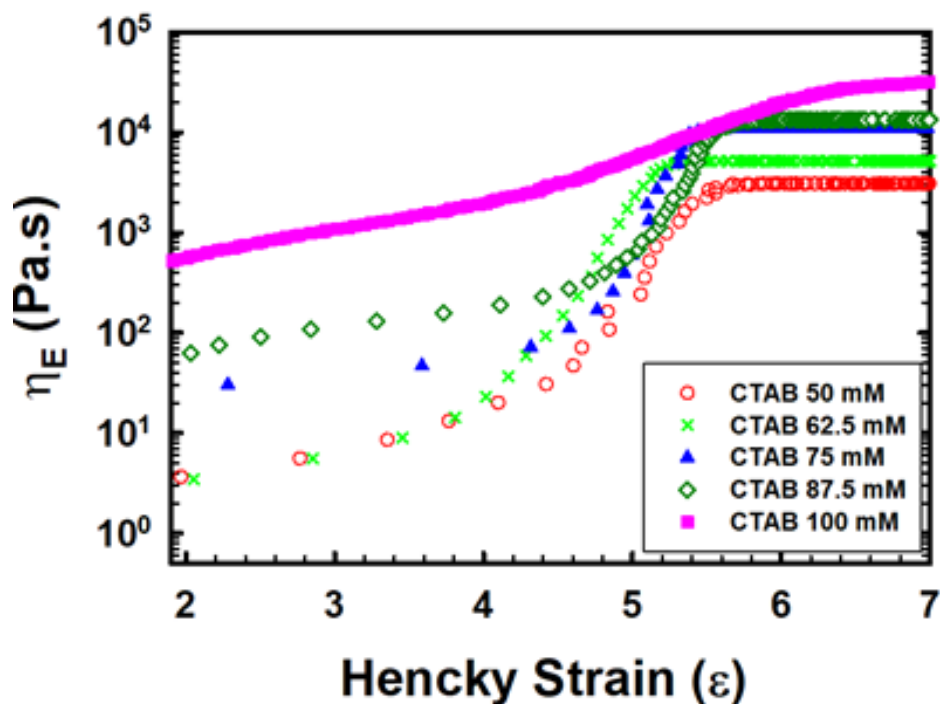


Figure 4.10. Extensional viscosities ( $\eta_E$ ) as a function of Hencky strains ( $\epsilon$ ).

#### 4.4. Effect of Temperature and Salinity on WMS Rheology

In many applications in which WMS is used, such as enhanced oil recovery (EOR)<sup>31, 106, 107</sup> and super cavitation desalination techniques,<sup>104, 105</sup> the wormlike micelles are subject to the high salinity conditions. For example, the base fluid for preparing WMS for EOR is usually sea water, especially in offshore applications where it is amply available.<sup>127</sup> For super cavitation desalination techniques, surfactants should be dissolved in sea water to add viscoelasticity to the system. Sea water contains around 3 wt% of sodium chloride (NaCl) and less amount of other ions such as magnesium ( $Mg^{2+}$ ), calcium ( $Ca^{2+}$ ), and potassium ( $K^+$ ).<sup>127, 128</sup>

There are two main effects of salts on micellar solutions: (i) the effect of salt on inducing wormlike micellar formation that increases the viscosity of fluid. Added salts facilitate the transition of spherical to wormlike micelles<sup>129</sup>, and (ii) the effect of excess salt on the viscoelastic properties of wormlike micelles in concern of their salinity resistance. It has been found that the addition of salts to solutions of cationic surfactants such as cetyl trimethylammonium halides (CTAX) can screen the charge between surfactant head groups and induce the formation of long cylindrical micelles. In this way, the addition of organic salts such as NaSal<sup>42, 129-131</sup> and 3-hydroxy-naphthalene-2-carboxylate (SHNC)<sup>132, 133</sup> was reported to be advantageous for inducing the viscoelasticity in the surfactant solutions, even at a low surfactant concentration. However, a less considered aspect in formulation and characterization of these materials is that WMS are exposed to the excessive salinity (secondary salts) that is presented in their applications.

There are a few studies that investigated the effect of secondary salts addition on WMS. Hu and Matthys<sup>134</sup> studied the effect of metal ions (including  $Na^+$ ,  $Zn^{2+}$ ,  $Mn^{2+}$ , and  $Ca^{2+}$ )

provided by inorganic salts (NaCl, zinc chloride  $ZnCl_2$ , magnesium chloride  $MnCl_2$ , and calcium chloride  $CaCl_2$ ) on WMS prepared using tris(2-hydroxyethyl) tallowalkyl ammonium acetate (TTAA)/NaSal. They reported that the shear viscosity and first normal stress ( $N_1$ ) of WMS have decreased after adding these salts. Xin *et al.*<sup>135</sup> studied the rheology of polyelectrolyte/surfactant complex in the presence of different kinds of inorganic salts (including potassium chloride KCl, NaCl,  $CaCl_2$  and  $MnCl_2$ ). They found that while the addition of each salt resulted in decreased shear viscosity, NaCl had the highest effect in dropping the viscosity of solution. Recently, Zheng *et al.*<sup>136</sup> investigated the effect of sea water on the viscosity of WMS that were prepared with cetyl trimethylammonium tosylate (CTAT)/NaSal. The authors reported that the shear viscosity of the solution and its  $N_1$  decreased because of salts in sea water compared to the WMS prepared with DI water. While it is understood that the secondary salts results in lower viscosity of WMS, the structural changes to wormlike micelles had not been investigated. The goal of present study was to understand the effect of secondary salts on the structure of WMS. Due to its ample presence in sea water and the highest effect (among the secondary salts<sup>135</sup>) on the wormlike micelles, NaCl chose as the secondary salt to be added to WMS prepared with CTAB/NaSal. Dynamic shear oscillatory measurements were used to investigate the effect of NaCl on the structure of wormlike micelles by using rheo-structure relations presented by reaction-reptation model. Indeed, the effect of added salt on the nonlinear rheology of WMS were investigated by using steady-state shear rheology.

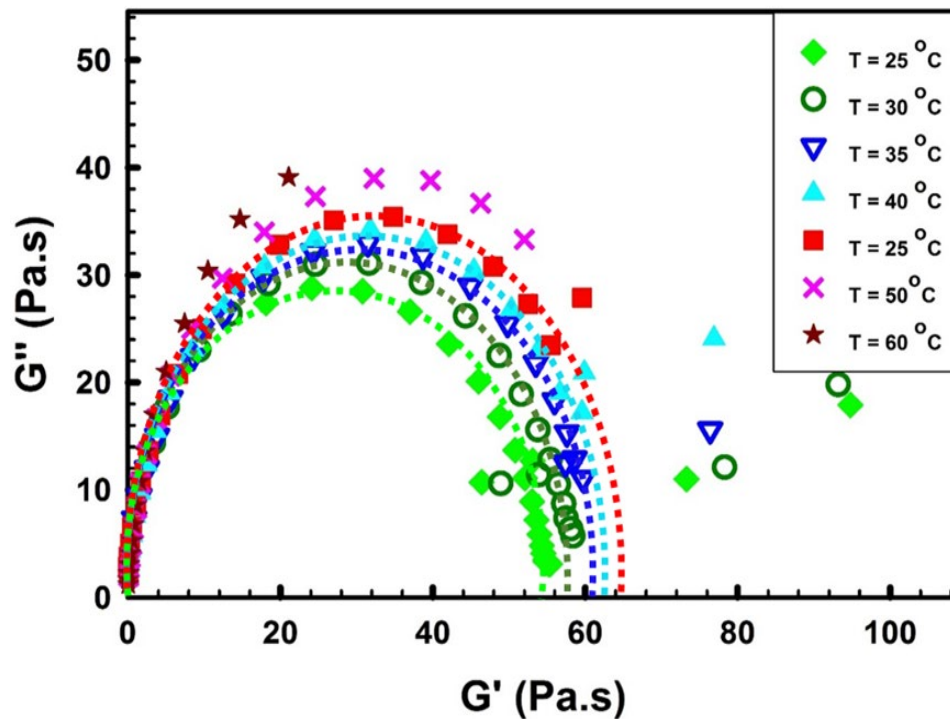
#### **4.4.1. Preparation of Test Fluids**

In order to investigate the effect of salt (NaCl) on the rheological behavior of WMS and the structure of wormlike micelles, the molar ratio of NaSal to CTAB was kept constant at

$R = 1$ . Four solutions with the concentrations of  $C_d = C_s = 100$  mM ( $R = 1$ ) were prepared by the same procedure described in Section 4.3.1. Then, appropriate amounts of NaCl (Sigma Aldrich Co., purity > 99.5%) were added to the three of those solutions to prepare solutions with the ratio of NaCl to CTAB,  $S = \left(\frac{[NaCl]}{[CTAB]}\right) = 0, 3, 6,$  and 9. Following the addition of NaCl, solutions were mixed for 12 h and left to sit for an additional 48 h to equilibrate.

#### 4.4.2. Effect of Temperature

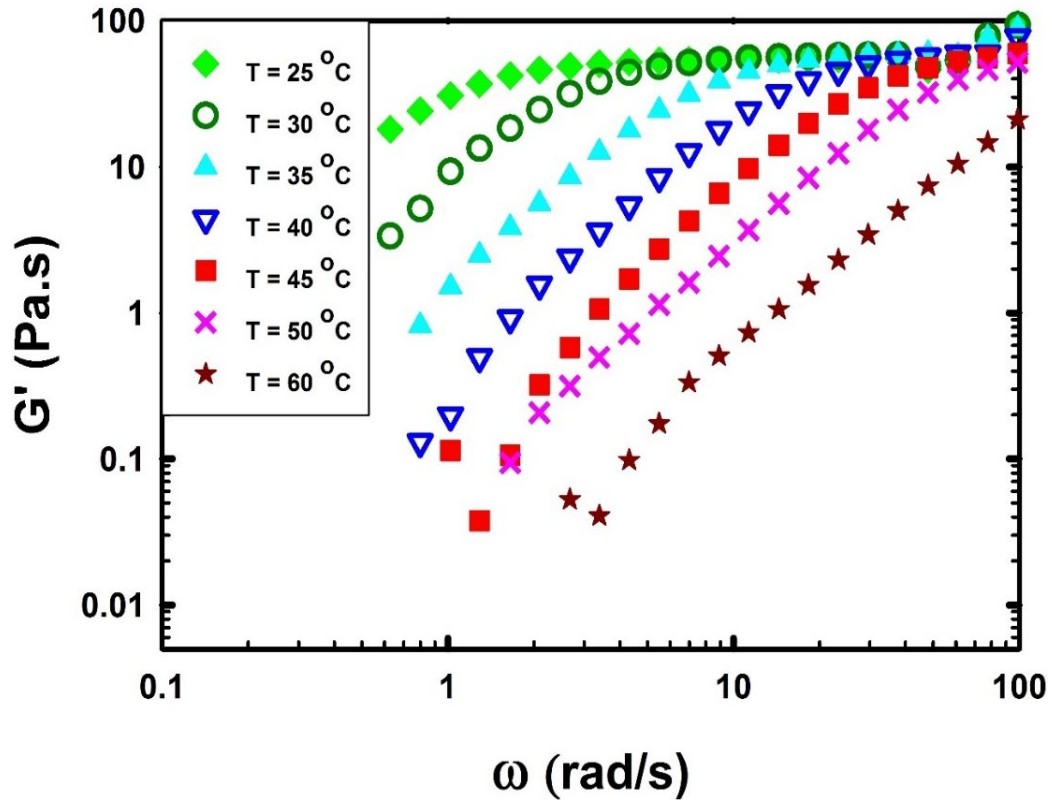
To investigate the effect of NaCl on WMS with different rheological characteristics, experiments were conducted at a different range of temperatures ( $25\text{ }^\circ\text{C} \leq T \leq 60\text{ }^\circ\text{C}$ ). In order to separate the effect of temperature and secondary salt on fluid rheology and structure, first, the effect of temperature on the base solution ( $[CTAB] = [NaSal] = 100$  mM, without NaCl) is investigated. For an ideal Maxwellian fluid, measured data points of viscous modulus as a function of elastic modulus should trace a semicircle. Figure 4.11 shows the Cole-Cole plot of the solution at different temperatures. For  $T \leq 45\text{ }^\circ\text{C}$ , data shown on the plot of  $G''$  versus  $G'$  show a semicircle shape except for the high values of  $G'$  (and  $\omega$ , see the relation of  $G'$  and  $\omega$  in Figure. 4.12). According to the reaction-reptation model,<sup>50, 54, 137</sup> the wormlike micelles show an upturn in their  $G''$  and  $G'$ , and the behavior of WMS deviates from the Maxwellian behavior at high frequencies where  $\omega$  is in order of  $\frac{1}{\lambda_b}$ . The local minimum of viscous modulus ( $G''_{min}$ ) where wormlike micelles start to deviate from the Maxwellian behavior can be used in equation 4.2 to calculate the ratio of entanglement length,  $l_e$ , to their average contour length,  $\bar{L}$ .



**Figure 4.11.** A Cole-Cole plot for the solution ( $S = 0$ ) under different temperatures ( $25\text{ }^{\circ}\text{C} \leq T \leq 60\text{ }^{\circ}\text{C}$ )

Figure 4.12. shows a plot of elastic modulus vs. angular frequency. For  $T \leq 45\text{ }^{\circ}\text{C}$ , all elastic modulus curves reached to the plateau modulus  $G'_0 \approx 55\text{ Pa}$  representing that wormlike micelles maintained their flow activation energy ( $E_a$ ) for  $T \leq 45\text{ }^{\circ}\text{C}$ . The flow activation energy is the energy that required to move a wormlike micelle in the environment of its neighboring micelles.<sup>138, 139</sup> Therefore, the  $E_a$  is the corresponding energy that a micellar chain required to release from the entanglements with its neighboring micelles. However, at higher temperatures the plateau modulus is observed at higher frequencies, which indicates faster dynamics of the micelles and is attributed to the shorter relaxation times<sup>138</sup> (Figure 4.13A). The effect of temperature on the elastic modulus is well corresponding with the results reported for WMS prepared with CTAB/SHNC.<sup>49</sup> For  $T > 45\text{ }^{\circ}\text{C}$ , the test solutions did not follow the Maxwellian behavior and did not show the plateau modulus

because those test solutions lost most of their viscoelasticity.



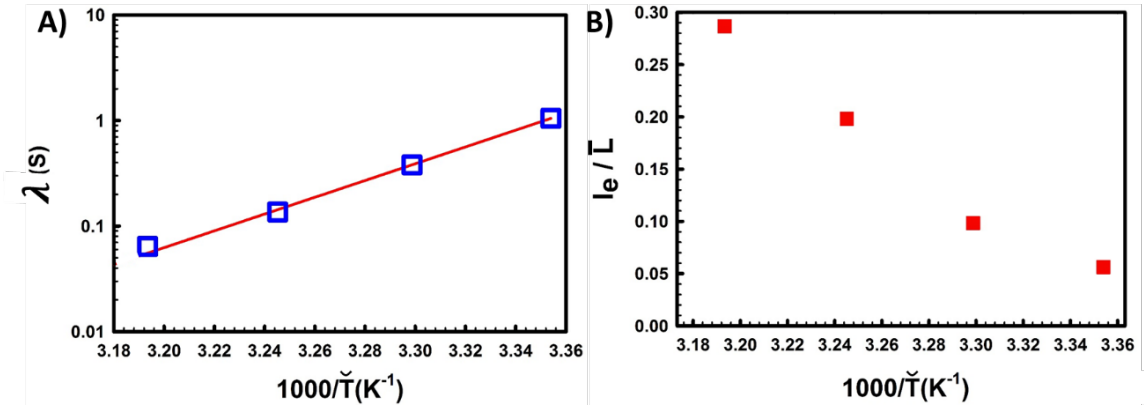
**Figure 4.12.** Elastic modulus as a function of angular frequency curves plots for solution ( $S = 0$ ) at varying temperatures ( $25\text{ °C} \leq T \leq 60\text{ °C}$ ).

Figure 4.13A shows the relaxation time of the test solution with  $S = 0$  under  $25\text{ °C} \leq T \leq 40\text{ °C}$ . The relaxation time decreased with elevated like from  $\lambda = 1.05$  at  $T = 25\text{ °C}$  to  $\lambda = 0.06$  at  $T = 40\text{ °C}$ . The relation of relaxation time  $\lambda$  with the temperature can be described by:

$$\lambda \sim \exp\left(\frac{E_a}{RT}\right) \quad (4.7)$$

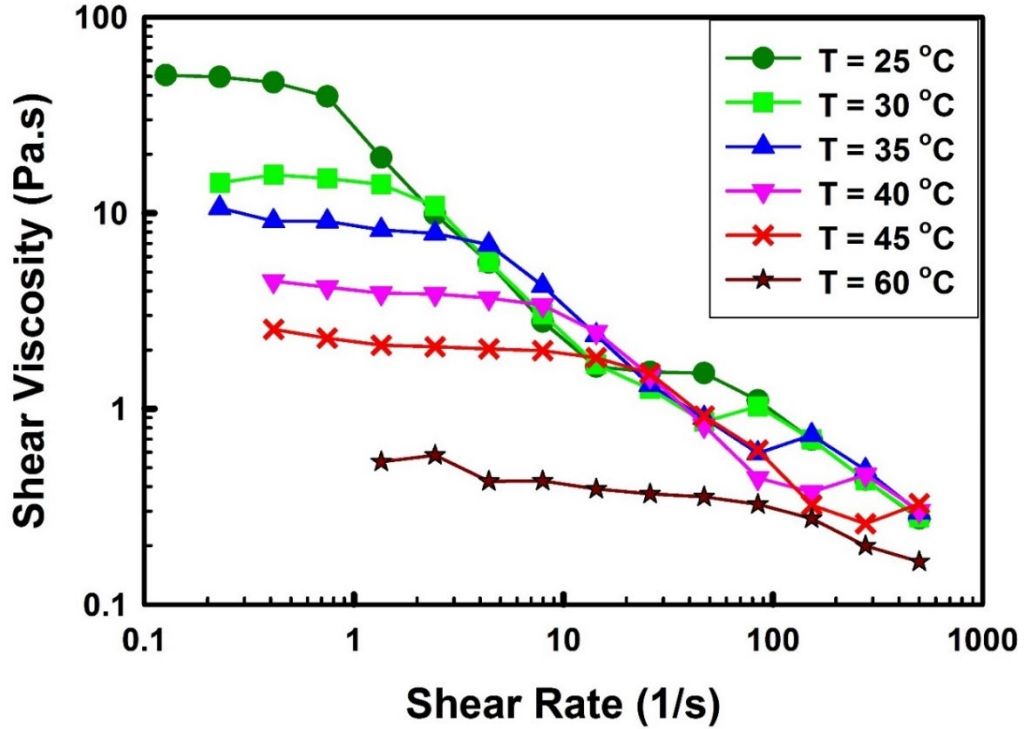
where  $R$  is the gas constant,  $T(K)$  is the absolute temperature, and  $E_a$  is the flow activation energy. The flow activation energy of the solution can be estimated from the slope of regression line in Figure 4.13A which yielded to  $E_a \approx 152.3 \frac{\text{kJ}}{\text{mol}}$ . The value of  $G''_{\min}$  versus

$G'_0$  provides a semi quantitative estimate for the ratio of  $l_e$  to  $\bar{L}$  by the equation 4.2. Figure 4.13B represents the ratio of  $l_e$  to  $\bar{L}$  as a function of temperature indicating that the ratio of entanglement length to the average micellar contour length increased with higher temperatures and that the number of entanglements per micellar chains decreased. At 25 °C, the ratio,  $\frac{l_e}{\bar{L}} (\sim \frac{G''_{min}}{G'_0})$  was 0.05 showing that the average chain length  $\bar{L}$  was ~20 times longer than the micellar entanglement length  $l_e$ . For higher temperatures, values of  $\frac{l_e}{\bar{L}} (\sim \frac{G''_{min}}{G'_0})$  increased to 0.1, 0.2, and 0.29 for temperatures of T = 30 °C, 35 °C, and 40 °C, respectively. It can be noted that there were less entanglements over the average micellar contour length at higher temperatures. This reduced number of entanglements per contour length could be interpreted in two ways: (i) the average contour length of micellar chains decreased at higher temperature or (ii) increased temperature resulted in the disentanglement of micellar chains. To get insight, it is noted that the entanglement mesh size of micellar chains can be calculated by the equation 4.4. Considering that the values of  $G'_0$  was constant ( $G'_0 \approx 55$ ) under  $25 \text{ °C} \leq T \leq 40 \text{ °C}$ , the network mesh size of micellar chains did not change significantly ( $\xi_m = 42.1 \text{ nm}$  at T = 25 °C and  $\xi_m = 42.9 \text{ nm}$  at T = 40 °C). Therefore, no disentanglement of micellar chains occurred, and the shortening of micellar chains must be the prominent reason for increased values of  $\frac{l_e}{\bar{L}}$  at higher temperatures.



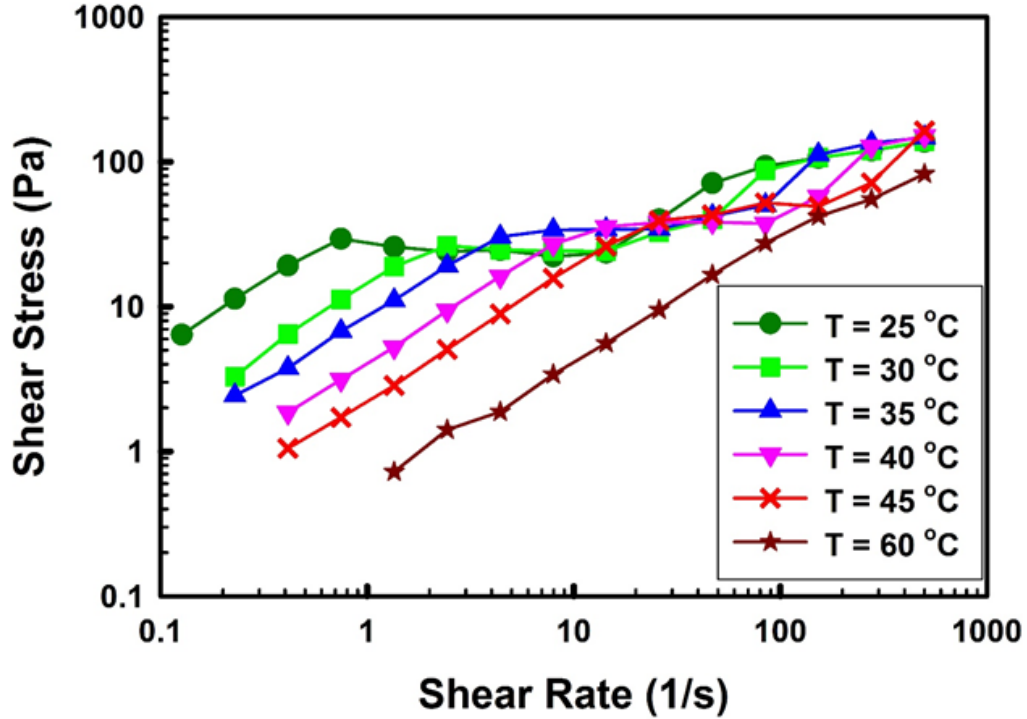
**Figure 4.13.** A) The semi logarithmic plot of relaxation time and B) the ratio of entanglement length as a function of absolute temperature for solution ( $S = 0$ ) at different temperatures ( $25\text{ }^{\circ}\text{C} \leq T \leq 40\text{ }^{\circ}\text{C}$ ).

Figure 4.14 shows the measured shear viscosity as a function of shear rates for  $S = 0$  at a range of temperatures,  $25\text{ }^{\circ}\text{C} \leq T \leq 60\text{ }^{\circ}\text{C}$ . Shear thinning behaviors were clearly observed for  $T \leq 45\text{ }^{\circ}\text{C}$ . While the solution kept its shear thinning behavior for  $T \leq 45\text{ }^{\circ}\text{C}$ , its zero-shear viscosity dropped as a function of temperature. For  $T \leq 45\text{ }^{\circ}\text{C}$ , the length of micellar chains decreased with higher temperatures, but they were still long enough to form micellar networks via entanglements, which showed the viscoelastic property. For higher temperatures (i.e. at  $T = 60\text{ }^{\circ}\text{C}$ ), the solution lost most of its viscoelasticity indicating that micellar chains were shortened to the degree that lost their viscoelastic properties. The decrease in zero-shear viscosity under increased temperatures was also observed in the literature, which is attributed to the shortening of wormlike micelles at higher temperatures



**Figure 4.14.** Shear viscosities vs. shear rates measured from the solution of  $S = 0$  at different temperatures ( $25\text{ °C} \leq T \leq 60\text{ °C}$ ).

Figure 4.15 shows the shear stress-shear rate curve,  $\sigma(\dot{\gamma})$  of the test solutions. The shear stress of the solution for  $T \leq 45\text{ °C}$  is associated with a stress plateau. The plateau observed in the shear stress-shear rate curve is a rheological signature for the shear banding phenomenon. The shear banding occurs when the applied shear rate is in between two critical shear rates ( $\dot{\gamma}_{c1} < \dot{\gamma} < \dot{\gamma}_{c2}$ ). In this range, an inhomogeneous biphasic flow of isotropic/nematic phases was reported where both phases were assumed to have the constant stress (corresponding to the plateau shown in Figure 4.15). The volume fraction of phases changed depending on the applied shear rates.<sup>33, 140</sup> Since the shear banding is a flow instability, the first critical shear rate ( $\dot{\gamma}_{c1}$ ) at which shear banding initiates should be related to the inverse of relaxation time ( $1/\lambda$ ). Therefore, increase  $\dot{\gamma}_{c1}$  at higher temperatures is well described by the shorten relaxation times of the solution.



**Figure 4.15.** Shear stresses vs. shear rates of of solution ( $S = 0$ ) at varying temperatures ( $25\text{ °C} \leq T \leq 60\text{ °C}$ ).

#### 4.4.3. Effect of Secondary Salts

Figure 4.16 shows the measured shear viscosity as a function of shear rate for solutions with different NaCl concentrations ( $S = 0, 3, 6$  and  $9$ ) at  $25\text{ °C}$ . The zero-shear viscosity dropped drastically by the addition of NaCl from  $\eta_0 = 53\text{ Pa}\cdot\text{s}$  at  $S = 0$  to  $\eta_0 = 32\text{ Pa}\cdot\text{s}$  at  $S = 3$ , but then did not change the zero-shear viscosity significantly by further addition of NaCl from  $S = 3$  to  $S = 9$ . Figure 4.17 shows corresponding shear stress-shear rate curves,  $\sigma(\dot{\gamma})$  for those same solutions. Addition of NaCl resulted in a shift of the first critical shear rate to higher shear rates ( $\dot{\gamma}_{c1}$ ). The NaCl addition also showed higher values of shear stress for the plateau regions.

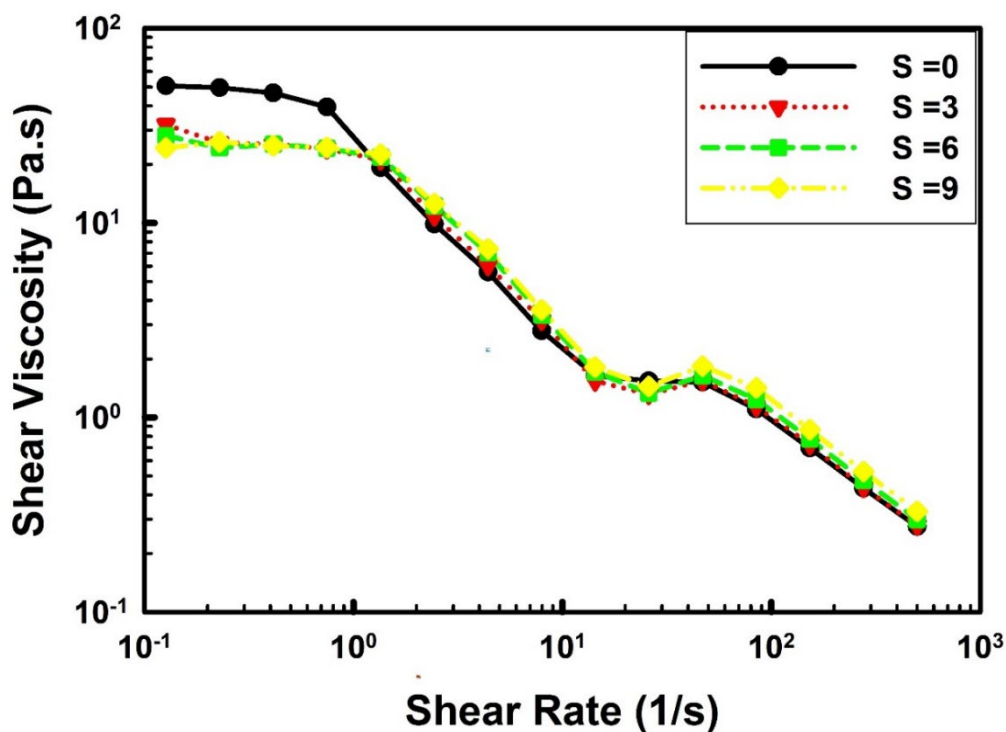


**Figure 4.16.** Shear viscosity vs. shear rates of solutions with different concentrations of NaCl ( $S = 0, 3, 6$  and  $9$ ) at  $25\text{ }^{\circ}\text{C}$ .

We suggest that the addition of NaCl to the solution resulted in branching of wormlike micelles, which made micellar chains more flexible under low shear rates ( $\dot{\gamma} < \dot{\gamma}_{cl}$ ). As proposed by Lequeux *et al.*<sup>141</sup>, branching points in micellar chains are labile, and their movements along micellar contour length facilitate the stress relaxation of micelles. Hence, the NaCl added solution ( $S = 3$ ) showed the lower zero shear viscosity compared to the solution without the addition of NaCl ( $S = 0$ ). The results also agree with the study of Truong *et al.* who investigated the effect of NaCl on CTAT micellar chains using a static light scattering method. They have reported that the addition of NaCl resulted in higher flexibility of CTAT micellar chains.<sup>142</sup> Therefore, unlike the effect of temperature on wormlike micelles that resulted in the shortening of wormlike micelles, the decreased zero-shear viscosity after adding NaCl is caused by branching of wormlike micelles. Moreover,

the higher stresses associated with the stress plateau of NaCl added solutions ( $S = 3, 6$  and  $9$ ) are because of transient network formation of branched micelles at higher applied shear rates ( $\dot{\gamma}_{c1} < \dot{\gamma}$ ). This agrees with the suggestion of Grand *et al.*<sup>143</sup> that a jump in stress plateau ( $\dot{\gamma}_{c1} < \dot{\gamma} < \dot{\gamma}_{c2}$ ) is a result of formation of transient network of branched wormlike micelles.

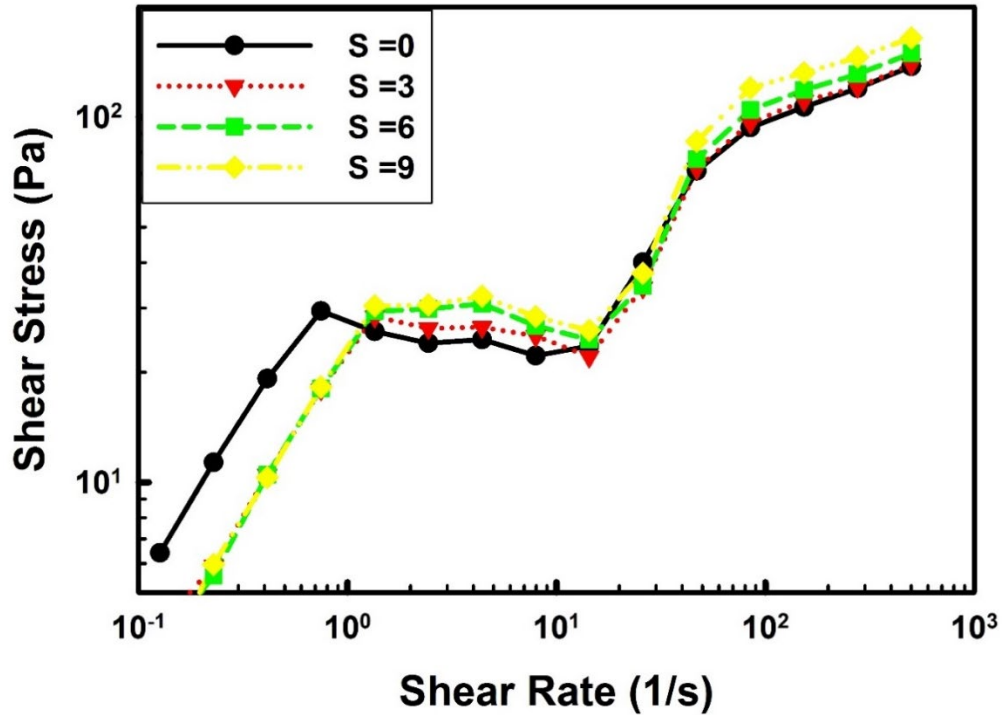


**Figure 4.17.** A Shear stress-shear rate plot of solutions with different concentrations of NaCl ( $S = 0, 3, 6$  and  $9$ ) at  $25\text{ }^{\circ}\text{C}$ .

Figure 4.18A shows the effect of NaCl addition on the relaxation time of WMS. At  $T = 25\text{ }^{\circ}\text{C}$ , addition of NaCl resulted in solutions with lower relaxation times. This agrees with the formation of branched wormlike micelles with addition of salt, where flexible branch points in wormlike micelles can move along the chain contour length to relieve the imposed stress. At higher temperatures, the relaxation times were shortened for all solutions due to

the effect of temperature on shortening of wormlike micelles. At each temperature, the relaxation time decreased with higher salt concentration. However, the slope of dropping relaxation times decreased at higher temperature. This could be attributed to the shortened micellar chain length at higher temperatures where the micellar chains were short enough to relax from the imposed stress quickly, and the flexibility of micellar chains was not a determining factor for the stress relaxation. Figure 4.18B shows the values of  $l_e$  over  $\bar{L}$ , which were obtained from the ratio of  $G''_{\min}$  to the  $G'_0$  following the equation 4.4.

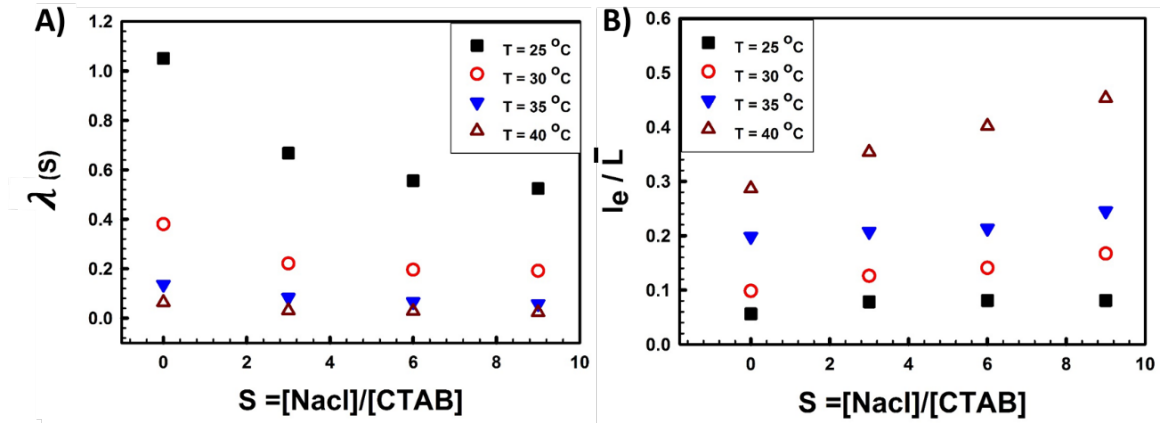


**Figure 4.18.** A) Relaxation time and B) the ratio of entanglement length over the average contour length of micelles as a function of  $S = \frac{[\text{NaCl}]}{[\text{CTAB}]}$  for solutions with different salt concentrations ( $S = 0, 3, 6$  and  $9$ ) at different temperatures ( $25 \text{ }^\circ\text{C} \leq T \leq 40 \text{ }^\circ\text{C}$ ).

Interestingly, while the relaxation time decreased from 1.05 s to 0.52 s by adding NaCl from  $S = 0$  to  $S = 9$  to the solution at  $T = 25 \text{ }^\circ\text{C}$ , the ratio of entanglement length to the contour length did not change significantly from  $\frac{l_e}{\bar{L}} \approx 0.05$  to 0.08. This observation suggests that the addition of NaCl does not affect the number of entanglements per contour length significantly and the decreased relaxation time is caused by the branching of micelles in the presence of NaCl. Moreover, adding NaCl to the solution from  $S = 0$  to  $S =$

3 resulted in a sharp decrease of relaxation time from  $\lambda = 1.05$  s to  $\lambda = 0.66$  s, while further increase of NaCl concentration from  $S = 3$  to  $S = 9$  affected the relaxation time loosely from  $\lambda = 0.66$  s to  $\lambda = 0.52$  s). This indicates that once branching of micellar chains occurred, the addition of more NaCl did not affect the structure of wormlike micelles significantly. This is corresponding well with the results obtained from zero-shear viscosities of solutions discussed with the figure 4.16 where there was a significant drop of  $\eta_0$  when NaCl concentration increased from  $S = 0$  to 3, but no significant change in  $\eta_0$  even after adding more NaCl.

#### 4.5. Conclusion

The shear and extensional rheological characteristics of WMS that are prepared using CTAB/NaSal ( $R = 0.32$ ,  $50 \text{ mM} \leq C_d \leq 100 \text{ mM}$ ) were investigated experimentally. The results of dynamic shear oscillatory measurements showed that increasing the surfactant concentration ( $C_d$ ) led to significant increase of the relaxation time ( $0.02 \text{ s} \leq \lambda \leq 6.1 \text{ s}$  for  $50 \text{ mM} \leq C_d \leq 100 \text{ mM}$ ). At higher  $C_d$ , test solutions formed highly entangled networks. The same result was also reflected in the shear viscosity measurements. Increasing  $C_d$  from 50 mM to 100 mM caused the zero-shear viscosity ( $\eta_0$ ) to increase by 5 orders of magnitude from 0.03 Pa·s to 121 Pa·s, while the ultimate viscosity of the solutions was in the same order ( $\eta_\infty \approx 0.03$ ). Indeed, the shear banding behavior was evidenced for the solutions with the tight entangled wormlike micelles ( $87.5 \text{ mM} \leq C_d$ ). The results of this study suggest that the shear banding phenomenon only occurs for high density entangled networks unlike the shear thinning occurs by the onset of entanglements.

The extensional relaxation time ( $\lambda$ ) of solutions also increased at higher  $C_d$  from 1.2 s to 7.5 s. However, the ratio of extensional relaxation times to the relaxation times ( $\lambda_E/\lambda$ ) that

was obtained from the linear rheology using the dynamics oscillatory measurements was significantly higher with the solutions of lower  $C_d$ . High values of  $\lambda_E/\lambda$  was previously observed by Sachsenheimer *et al.*<sup>32</sup> for CTAB/NaSal solutions with  $R < 1$ , from which  $\lambda_E/\lambda$  were found to increase at lower  $R$ . The authors concluded that high  $\lambda_E/\lambda \approx 10$  at  $R = 0.5$  is related to the formation of EIS during the extension of the CTAB/NaSal solution. To the best of our knowledge, this study firstly evidenced the very high ratio of relaxation times of  $\lambda_E/\lambda \approx 60$  when using the solution of  $C_d = 50$  mM. Indeed, it was found that  $\lambda_E/\lambda$  decreased to  $\lambda_E/\lambda \approx 1.2$  with the solution of higher  $C_d$ , which supports the suggestion of EIS formation during the elongation. Wormlike micellar chains should align along the elongation direction to form EIS structure, which is hindered by the entanglement points when the test solution has higher  $C_d$ . The coil/stretch transitions can be another contributing factor to the  $\lambda_E/\lambda$ , in which wormlike micelles can be fully stretched along the direction of elongation axis in the solution of lower  $C_d$ . However, the extensibility of entangled micelles is limited to the micellar chain length between the entanglements. The extensional viscosity of the test solution was associated with the strain hardening. While the more entangled micelles at higher  $C_d$  induced higher extensional viscosities, the strain hardening was more prominent at lower  $C_d$ , which can be explained by the role of entanglements in promoting viscosity and hindering the extensibility of wormlike micelles.

A complementary experimental investigation has been carried out to study the effects of temperature and salinity on the viscoelastic characteristics of WMS with  $C_d = C_s = 100$  mM ( $R = 1$ ). The solution without NaCl ( $S = 0$ ) showed the shear thinning behavior for  $T \leq 45$  °C but lost most of its viscoelasticity for higher temperatures than 45 °C. For  $T \leq 45$  °C, the zero-shear viscosity and relaxation time decreased with the increased temperature,

while its plateau modulus remained constant at  $G'_0 \approx 55$  Pa. The ratio of micellar chain length to its contour length,  $\frac{l_e}{L} (\sim \frac{G''_{min}}{G'_0})$  increased with the increased temperature indicating that there were less entanglements per the average contour length of micellar chains at higher temperatures. Considering the independency of  $G'_0$  from the temperature for  $T \leq 45$  °C, the entanglement network of micelles was not affected (e.g.,  $\xi_m = 42.1$  nm at  $T = 25$  °C and  $\xi_m = 43$  nm at  $T = 45$  °C). Therefore, increasing temperature up to  $T \leq 45$  °C resulted in the shortening of micellar chains with lower  $\tau_R$  and  $\eta_0$ , but did not affect the entanglement network of solution. The solution also kept its flow activation energy ( $E_a \approx 152.3 \frac{kJ}{mol}$ ) and showed a constant  $G'_0 \approx 55$  Pa.

Initial adding of NaCl to the solution resulted in a significant drop of zero-shear viscosity from  $\eta_0 = 53$  Pa·s at  $S = 0$  to  $\eta_0 = 32$  Pa·s at  $S = 3$ , while the further addition of NaCl from  $S = 3$  to  $S = 9$  did not influence the zero-shear viscosity. All solutions showed a plateau region in their shear stress-shear rate curve ( $\sigma(\dot{\gamma})$ ), which represents the shear banding behavior. For solutions with higher concentrations of NaCl, the stress plateau occurred at higher stresses. Therefore, we suggested that the addition of NaCl to the solution resulted in forming of branched wormlike micelles. Since branched wormlike micelles are more flexible, adding NaCl resulted in lower zero-shear viscosity of solution. Branched micelles resulted by NaCl addition formed a transient network for the shear rate above  $\dot{\gamma}_{c1}$  and showed higher shear stress plateau. In this way, the effect of NaCl addition was to induce branched flexible wormlike micelles unlike the effect of temperature on wormlike micelles that caused the shortening of wormlike micelles.

Further characterization of solutions supported the hypothesis that the branched wormlike micelles were formed as a result of NaCl addition. While increasing NaCl from  $S = 0$  to 9

in the test solutions resulted in shorten relaxation time from  $\tau_R = 1.05$  s to 0.52 s, the ratio of entanglements length to the average contour length did not change significantly from  $\frac{l_e}{L} \approx 0.05$  to 0.08. Therefore, the observed drop of the relaxation time was due to the branching of micelles. Besides, the addition of NaCl to the solution from  $S = 0$  to 3 resulted in a sharp decrease in relaxation time from  $\tau_R = 1.05$  s to 0.66 s, while further increasing of NaCl concentrations from  $S = 3$  to 9 rarely affected the relaxation time indicating that once the branching of micelles occurred, the addition of more NaCl did not affect the structure of wormlike micelles. This is corresponding well with the results obtained from the measurements of zero-shear viscosity, in which a significant drop of  $\eta_0$  was observed when NaCl was added to  $S = 3$ , but no additional drop of zero-shear viscosity even after adding more NaCl (see Figure 4.16).

## V. MICROSCOPIC FLOW OF WORMLIKE MICELLAR SOLUTION IN CONTRACTION GEOMETRY

### 5.1. Introduction

The microscopic flows of viscoelastic wormlike micellar solutions (WMS) through a contraction geometry have been studied in this chapter. The flows of viscoelastic solutions are influenced by their non-linear rheology and elasticity. In addition to that there is no exact solution to obtain the velocity profiles of viscoelastic fluids due to their non-Newtonian rheology, elastic-induced phenomena such as formation of secondary flows make the characterization of the contraction viscoelastic flows even more complex.<sup>8, 9, 12, 18, 75, 144-146</sup> The product of deformation rate and relaxation time of the fluid ( $\lambda\dot{\gamma}$ ) results in a non-dimensional number that estimates the level of elasticity of the fluid flow. This non-dimensional number is named interchangeably in the literature as Weissenberg (Wi) or Deborah (De) number, which have been widely used to characterize the contraction flow of viscoelastic fluids. While the viscoelastic fluids may show different relaxation times in shear and extensional flows, a wide range of relaxation times was used in the literature to calculate the non-dimensional number. In Section 5.2, we discuss the definition of Wi and De non-dimensional numbers and define the non-dimensional numbers that were chosen for this study. The fabrication of microchannel and the experimental setup are described in Section 5.3. Newtonian-like behavior and corner vortices are discussed in Sections 5.4 and 5.5. For gel-like WMS with the strong shear thinning and shear banding rheology, a new type of flow behavior is documented, and how these non-Newtonian fluids influenced the flow behavior are discussed in Sections 5.6 and 5.7.

## 5.2. Non-Dimensional Numbers

Two non-dimensional numbers, De and Wi numbers, are commonly used to quantify the viscoelastic effects in a viscoelastic solution that is subjected to the large deformation. Although these numbers are usually used interchangeably and often appeared with the same formula, they have different definitions, which describe the viscoelastic effects from a different perspective. The Deborah number is named after Prophetess Deborah who proclaimed “*The mountains flowed before the lord*”.<sup>147</sup> As explained by Reiner,<sup>147</sup> the Deborah number points to the fact that the behavior of every material depends on the timescale of observation. For sufficiently large observation time, each material behaves as ‘fluid-like’ and in contrast, if the time scale of the observation is too short, the behavior of the material to the observer is considered as a solid. Therefore, the De number reflects the behavior of material over a given timeframe, and Reiner defined De number of a viscoelastic material as the ratio of characteristic relaxation time ( $\lambda$ ) of the material to the time of observation. This definition was modified later by Metzner *et al.*<sup>148</sup> and the time of observation was replaced by the timescale of deformation. Therefore, the timescale of deformation ( $t_f$ ) can be calculated as the inverse of deformation rate ( $\dot{\gamma}$ ) for a viscoelastic fluid that is subjected to a deformation with the given rate, and the De number is obtained as follows:

$$\text{De} = \frac{\lambda}{t_f} = \lambda\dot{\gamma} \quad (5.1)$$

Weissenberg number that is named after Karl Weissenberg quantifies the relative magnitude of elastic stress to viscous stress in a viscoelastic material that is subjected to a deformation.<sup>149</sup> Considering a fluid in a steady state shear flow, the ratio of normal (elastic) to the shear (viscous) stresses defines the Wi number:

$$Wi = \frac{N_1}{2\sigma_{xy}} = \frac{\eta\dot{\gamma}^2\lambda}{\eta\dot{\gamma}} = \lambda\dot{\gamma} \quad (5.2)$$

where  $\eta$  is the viscosity of the fluid. The equation 5.2 for Wi number is adopted to study the flow of viscoelastic solutions in microscale. In case a viscoelastic fluid flows through sudden contraction geometry, the non-dimensional number is called as either De number or Wi number using the formula of  $(\lambda\dot{\gamma})$ . In addition, while the Wi or De number was often used to compare the results of studies on different fluids and geometries, the relaxation time and characteristic deformation rate were also used as important parameters in previous studies. In following, different relaxation times that were used to characterize the viscoelastic solution are described. The dynamic oscillatory shear measurement characterizes the relaxation time ( $\lambda$ ) of fluid in its linear rheology (i.e., equilibrium state). In addition, in case of viscoelastic polymer solutions in which a single shear relaxation time cannot be characterized by using the shear oscillatory measurement, the relaxation time is calculated based on the Zimm theory,<sup>150</sup> which shows the relaxation time of polymer chains in their equilibrium state.

The relaxation time of the material when it is subjected to the elongation ( $\lambda_E$ ) is obtained by an extensional rheometry. Since most pervious experiments have characterized the extensional relaxation time by using a capillary break up (CaBER) rheometer, the extensional relaxation time was also denoted as  $\lambda_{CaBER}$ . Rod *et al.* (2004)<sup>151</sup> defined the deformation rate as the shear rate in the downstream of the contraction (see equation 5.3) using the extensional relaxation time ( $\lambda_{CaBER}$ ). They also denoted the non-dimensional number with De number ( $De = \lambda_{CaBER}\dot{\gamma}_d$ ):

$$\dot{\gamma}_d = \frac{U}{\frac{w_c}{2}} = \frac{2Q}{w_c h^2} \quad (5.3)$$

where  $Q$  is the volumetric flow rate,  $w_c$  and  $h$  are the width and height of the downstream channel (see Figure 5.1), respectively, and  $U$  ( $= \frac{Q}{w_c h}$ ) is the velocity of fluid in the downstream channel. While Rod *et al.* (2005)<sup>19</sup> used the similar relaxation time and deformation rate, they denoted the non-dimensional number with  $Wi$  number ( $Wi = \lambda_{CaBER} \dot{\gamma}_d$ ). Comparable definitions were used in the study of Rod *et al.* (2010)<sup>152</sup>, Haward *et al.* (2010)<sup>21</sup>, Li *et al.* (2011)<sup>22</sup>, Lanzaro and Yuan (2011)<sup>23</sup>, Lee *et al.* (2014)<sup>25</sup>, and Hidema *et al.* (2019).<sup>153</sup> However, in the studies of Rodd *et al.* (2007)<sup>154</sup> and Sankaran *et al.* (2013)<sup>26</sup>, the  $Wi$  number was defined by using the Zimm relaxation time ( $Wi = \lambda_{Zimm} \dot{\gamma}_d$ ). Gulati *et al.* (2008)<sup>155</sup> and Hemminger *et al.* (2010)<sup>27</sup> defined the  $Wi$  number with the relaxation times obtained from the shear oscillatory measurement ( $Wi = \lambda \dot{\gamma}_d$ ). In this study, the  $Wi$  number is defined by the relaxation time obtained from the shear oscillatory measurements:

$$Wi = \lambda \dot{\gamma}_d = \frac{2\lambda Q}{w_c h^2} \quad (5.4)$$

and the  $De$  number is calculated by using the extensional relaxation time:

$$De = \lambda_E \dot{\gamma}_d = \frac{2\lambda_E Q}{w_c h^2} \quad (5.5)$$

The results that were obtained from the microscopic flow visualization experiments are characterized based on both non-dimensional numbers to see which relaxation time better describes the flow behavior.

The non-dimensional Reynolds number ( $Re$ ) is defined as the ratio of inertial stress to viscous stress that are associated with the fluid flow. For the flow passing through the

contraction geometry, the Re number is calculated by:

$$\text{Re} = \frac{\rho U D_h}{\eta} = \frac{2\rho Q}{(w_c + h)\eta} \quad (5.6)$$

where  $\rho$  is the density of fluids,  $D_h$  is the hydraulic diameter, and  $\eta$  is the viscosity of fluids. In microfluidic devices, the characteristic length scale is in order of tens to hundreds of micrometers, and only a small volume of fluids flows in the microchannel. Therefore, Reynolds numbers are quite small, so the viscous force dominates over the inertial force in the microscale. In several previous studies, the zero-shear viscosity ( $\eta_0$ ) is used for the equation 5.6 to calculate the Re number<sup>19, 152, 154</sup>. While using  $\eta_0$  simplifies the calculations, it is not an accurate assumption for shear thinning fluids. In this study, the viscosity as a function of applied shear rate,  $\eta(\dot{\gamma})$  that was obtained from the shear measurement (see Figure 4.4) is used for the calculation of Re numbers of shear thinning test fluids.

The viscoelastic Mach number (Ma) is the ratio of flow velocity to the speed of elastic wave ( $c_s$ ) that is propagating in the viscoelastic fluid, which is defined by:

$$c_s = \sqrt{\frac{G'}{\rho}} = \sqrt{\frac{\eta}{\lambda\rho}} \quad (5.7)$$

and the viscoelastic Ma number is calculated by:

$$\text{Ma} = \sqrt{\text{DeRe}} \quad (5.8)$$

When the speed of the flow has exceeded that of the elastic wave (i.e.,  $\text{Ma} > 1$ ), it is expected that an elastic induced instability occurs in the flow.<sup>156, 157</sup>

### 5.3. Design and Fabrication of Microfluidic Chips

A microchannel with an 8:1 planar contraction was machined directly on a polymethyl methacrylate (PMMA) chip (Plexiglas®, ePlastics) using a 5-axis CNC micro-milling machine (Minitex Machinery, Norcross, GA). An end mills (Performance Micro Tool, Janesville, WI) with the tip diameter of 203  $\mu\text{m}$  was used to carve the microchannel and the inlet/outlet ports. Figure 5.1 illustrates dimensions of a planar contraction geometry with an upstream channel width ( $w_u$ ) of 2 mm and contraction width ( $w_c$ ) of 250  $\mu\text{m}$  along with a uniform channel depth ( $h$ ) of 500  $\mu\text{m}$ . The machined chip was thermally bonded to a 0.8 mm thick PMMA sheet. Dispensing needle tips with an inner diameter (ID) of 0.81 mm were then glued to both sides of the channel where inlet and outlet ports were located. One end of a 0.9 mm ID tube (Upchurch Scientific Inc., Oak Harbor, WA) was then connected to the inlet needle and the other end was connected to a 5 mL gas-tight syringe (Hamilton, Reno, NV) via a lure lock connector. After the test solution was loaded in the syringe with care not to include air bubbles, the syringe was placed on a syringe pump (New Era Pump Systems, Farmingdale, NY). The volumetric flow rate ( $Q$ ) was varied from 0.05 mL/h to 16 mL/h for this study. For each measurement, a fixed flow rate was applied for at least 5 mins before images were taken to ensure the flow reached its steady state.

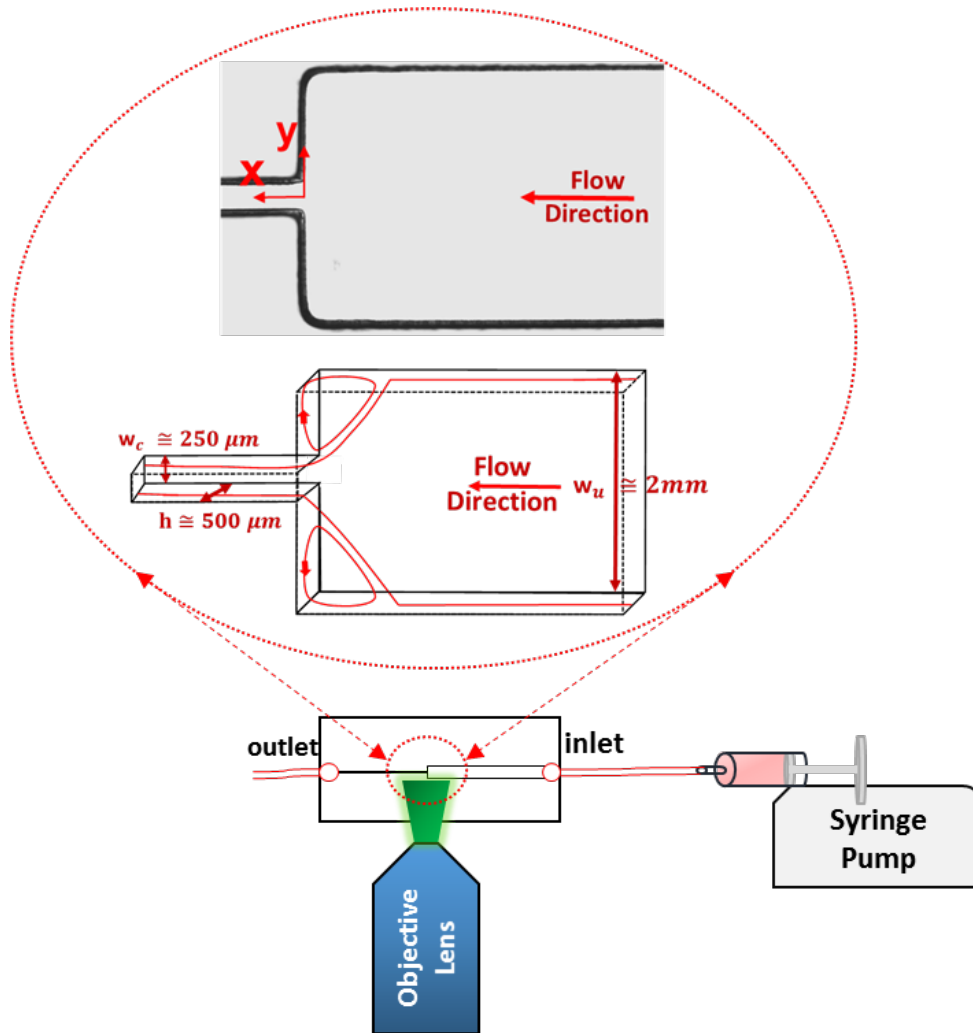


**Figure 5.1.** Schematic diagram of experimental setup for the investigation of WMS behavior at the sudden contraction microchannel.

#### 5.4. Newtonian-Like Flows

For the lower range of volumetric flow rates ( $Q$ ) in which the  $De$  and  $Wi$  numbers were small, the fluidic behavior is similar with the flow of Newtonian fluids (Newtonian-like flow). Figure 5.2 shows representative streak images of WMS ( $C_d \leq 75 \text{ mM}$ ) at  $Q = 0.2 \text{ mL/h}$ . In this flow regime, no flow instability or formation of secondary flows was observed. Figure 5.3 shows a map of  $De$ ,  $Wi$  and  $Re$  numbers for all the flow conditions in which the Newtonian-like behavior was observed. For  $C_d = 50 \text{ mM}$ , the Newtonian-like

behavior is observed for  $Re \leq 0.039$ ,  $Wi \leq 0.52$  and  $De \leq 31.1$ . For higher  $C_d$  where the solutions had higher viscosity and lower  $Re$ , the Newtonian-like behavior is found at lower  $Re$  numbers, but higher  $Wi$  and  $De$  numbers.

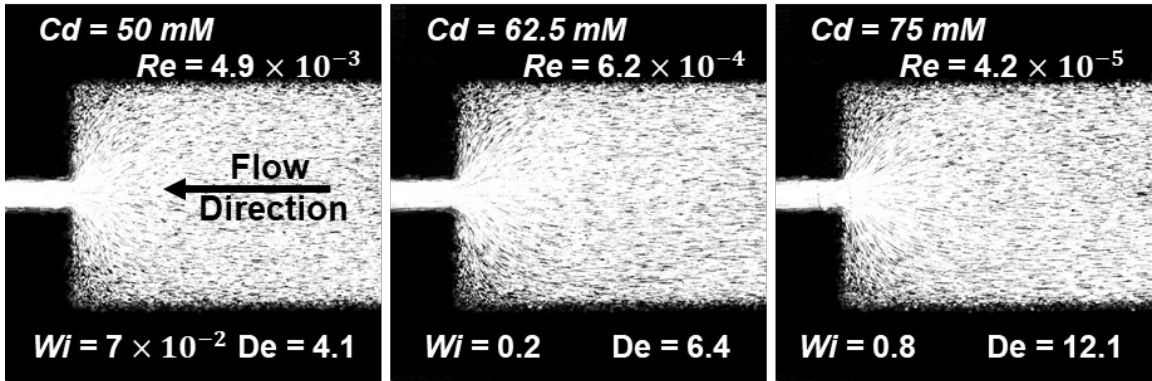


**Figure 5.2.** Streak images of solutions with  $C_d = 50, 62.5,$  and  $75$  mM at the same volumetric flow rate of  $Q = 0.2$  mL/h

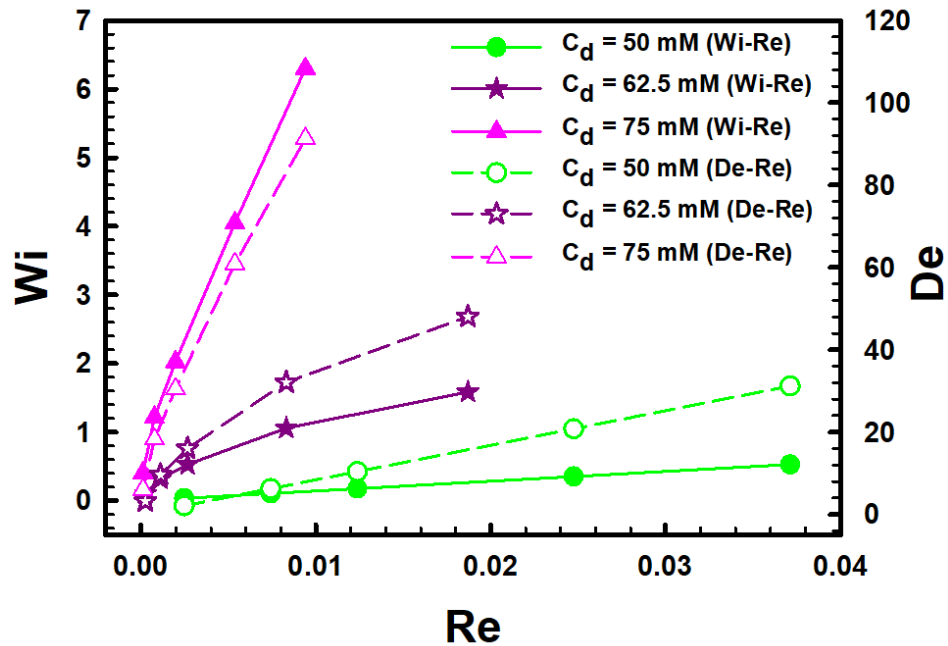


**Figure 5.3.** A  $De$ - $Wi$ - $Re$  map showing the summary of flow conditions that each solution showed Newtonian-like flow pattern.

Therefore, introducing a single critical  $Wi$  or  $De$  number for which the solutions show a

transition from the Newtonian-like behavior to the onset of elastic related phenomena (i.e. formation of secondary flows) is not accurate. Instead, we observed that all solutions ( $C_d \leq 75$  mM) showed Newtonian-like behavior when the viscoelastic Mach number is smaller than 1 ( $Ma < 1$ ). The transition from Newtonian-like flows to secondary flows occurred at  $Ma \approx 1$ . A map of viscoelastic Mach numbers calculated for each solution is plotted in Figure 5.4. It is suggested that when the viscoelastic Mach number exceeds one and the fluid velocity exceeds its characteristic elastic wave speed, an elastic shock wave generates in the flow that could initiate the instability in the viscoelastic flow. Since the calculation of viscoelastic Ma number is corresponding to the geometric average of Re and De, it can be concluded that even for very low Re numbers, the Re number should be considered for the onset of elastic instabilities.

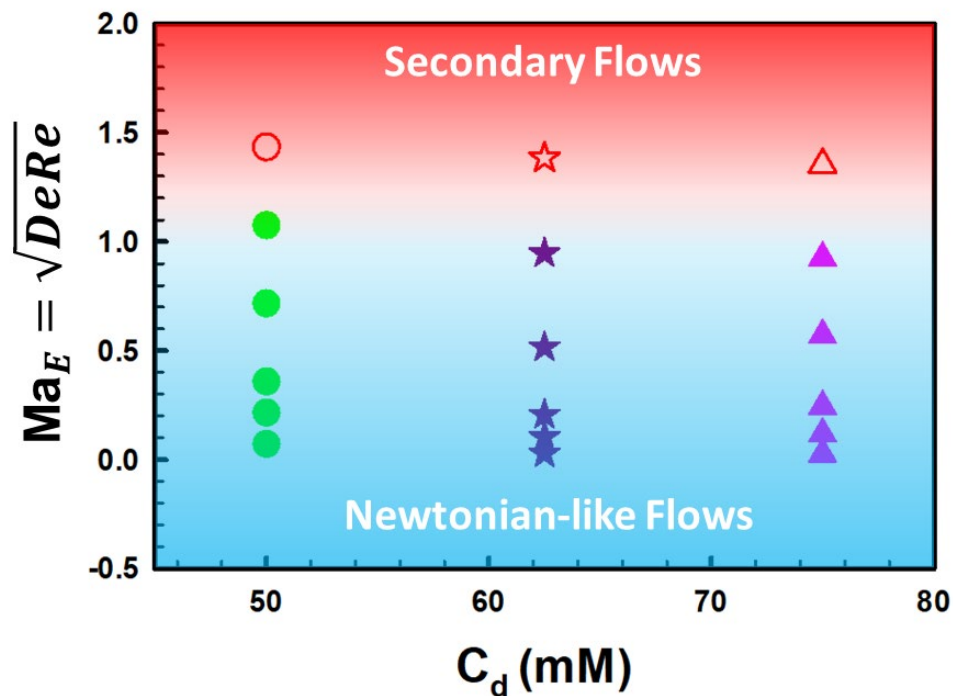


**Figure 5.4.** Transition from Newtonian-like flows (solid symbols) to Secondary flows (hollow symbols) in terms of viscoelastic Mach number for solutions with  $C_d = 50, 62.5,$  and  $75$  mM.

### 5.5. Evolution of Vorticities

As increasing the flow rate of test solutions, in turn, the  $Wi$  and  $De$  numbers, the Newtonian-like flow regime has evolved into the vortex flow regime where vortex began to appear at both upstream corners as shown in Figure 5.5. The corner vortices kept growing at higher applied flow rates. For each solution, the vortices were initially symmetric and turned to non-symmetric for higher flow rates.

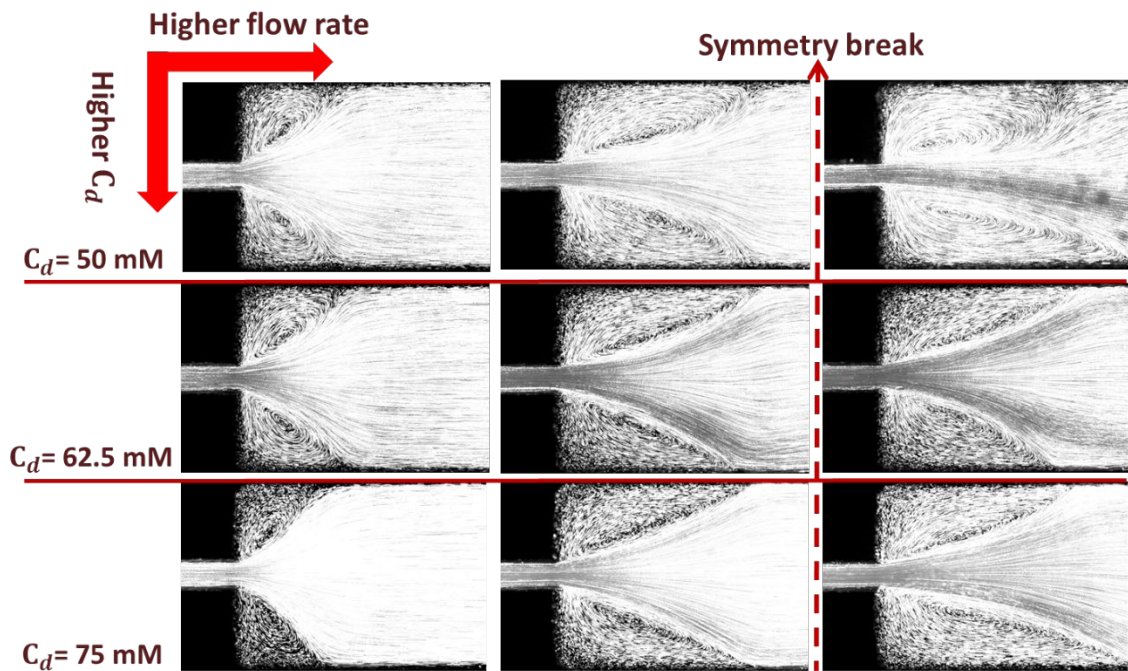


**Figure 5.5.** Streak images of solutions with CTAB molar concentrations of  $C_d= 50, 62.5,$  and  $75$  mM.

In order to quantify the flow behavior of solutions with non-dimensional numbers, the length of vortices was measured and normalized by the width of downstream microchannel ( $w_c$ ). The normalized vortex length ( $L/w_c$ ) is plotted as a function of  $Wi$  and  $De$  numbers as shown in Figure 5.6A and B. For  $C_d = 50$  mM, the vortices were observed for  $0.5 \leq Wi \leq 1.4$  and  $31.1 \leq De \leq 83$ . The length of vortices increased as a function of  $Wi$  and  $De$  numbers. The growth of vortices at higher  $Wi$  and  $De$  numbers was also observed for  $C_d =$

62.5 and 75 mM. However, the range of  $Wi$  and  $De$  numbers at which the vortices were observed were quite different for each solution ( $1.5 \leq Wi \leq 6.3$  and  $48 \leq De \leq 192.2$  for  $C_d = 62.5$  mM, and  $6 \leq Wi \leq 40$ ,  $91.2 \leq De \leq 609$  for  $C_d = 75$  mM). Therefore, the growth of vortices could not be described by  $Wi$  and  $De$  numbers. Indeed, while the transition from the Newtonian-like flows to the formation of secondary flows were observed at viscoelastic  $Ma \approx 1$ , no correlation was found between the  $Ma$  numbers and the growth of vortices.

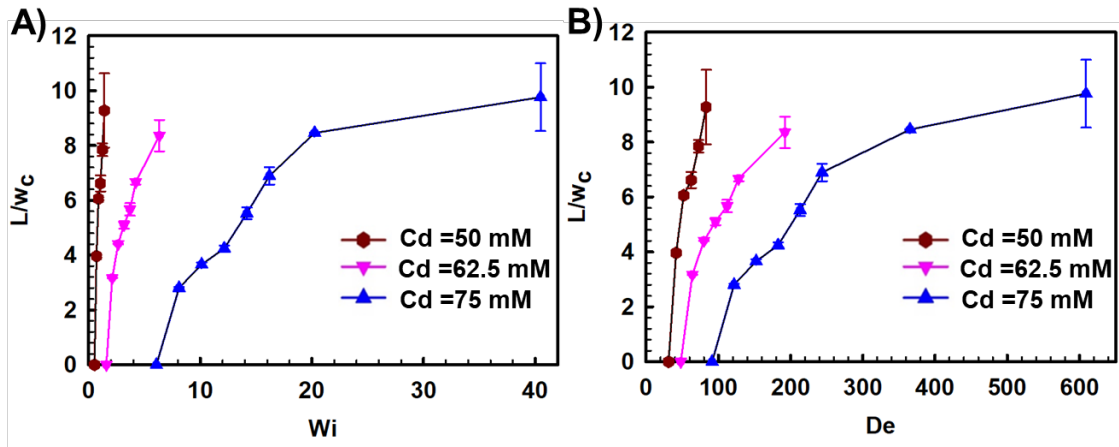


**Figure 5.6.** The normalized vortex length as a function of A)  $Wi$  number and B)  $De$  number.

It is well agreed that the formation and growth of secondary flows are caused by the elasticity of the viscoelastic fluid when it is subjected to high deformation rates. The vortices are formed and grow to minimize the elastic energy that is built up in the fluid.<sup>21</sup> The viscoelastic fluid in the main flow near the centerline area is subjected to high extension rates while only weak shear rates are applied to the fluid of the secondary flows near the corner area. Therefore, the extensional relaxation time of the fluid determines how much stress is accumulates in the main flow while the shear relaxation influences the stress accumulation in the secondary flows. In this study, we multiplied the  $De$  number with a factor of the relaxation time ratio ( $\frac{\lambda_E}{\lambda}$ ) of each fluid and plotted the length of vortices as a

function the resulted non-dimensional number ( $\frac{\lambda_E}{\lambda} \times De$ ) as shown in Figure 5.7. The  $De$  number multiplied by ratio of relaxation times ( $\frac{\lambda_E}{\lambda}$ ) shows a close correlation with the length of vortices regardless of the fluid  $C_d$  compared to the cases when the  $Wi$  or  $De$  numbers were used.

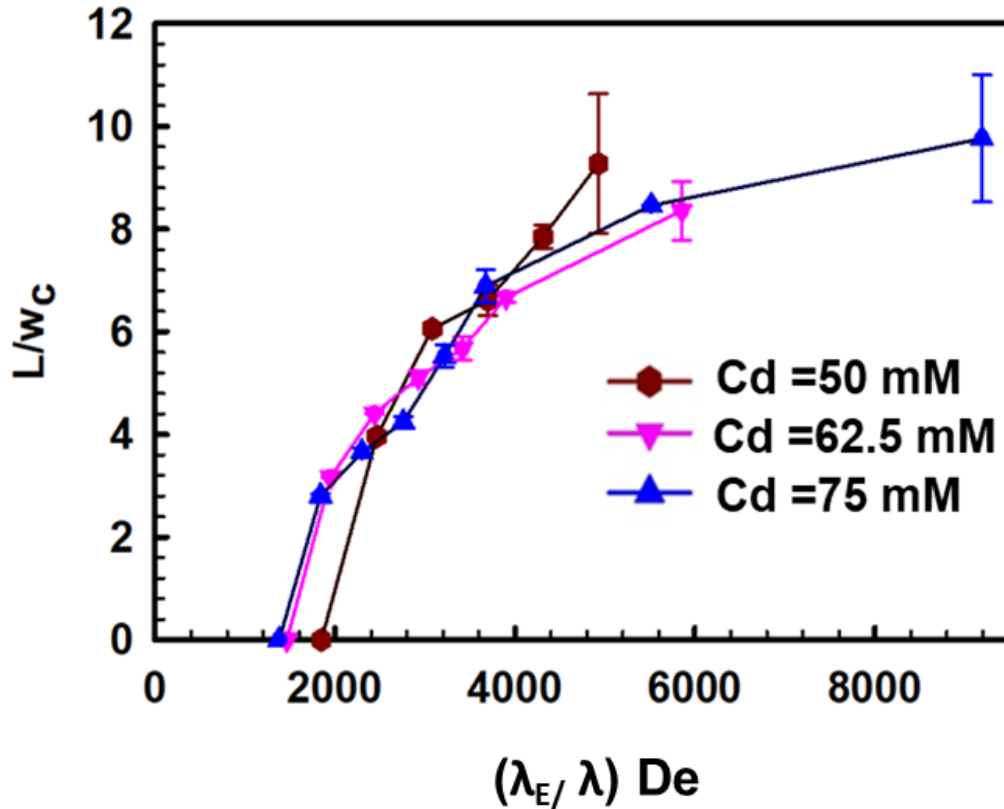


**Figure 5.7.** The normalized vortex length as a function of  $De$  numbers that are modified by the ratio of extensional to shear relaxation times.

### 5.6. Steady Viscoelastic Flows

The flow behaviors of test fluids with  $C_d = 87.5$  and  $100$  mM were deviated from the Newtonian-like flows even under low volumetric flow rates. Figure 5.8 shows representative streak images of WMS ( $C_d = 87.5$  and  $100$  mM) at  $Q = 0.2$  mL/h. While the flow patterns remained steady, the reduction in velocities was observed in upstream corner

areas near the contraction entry.

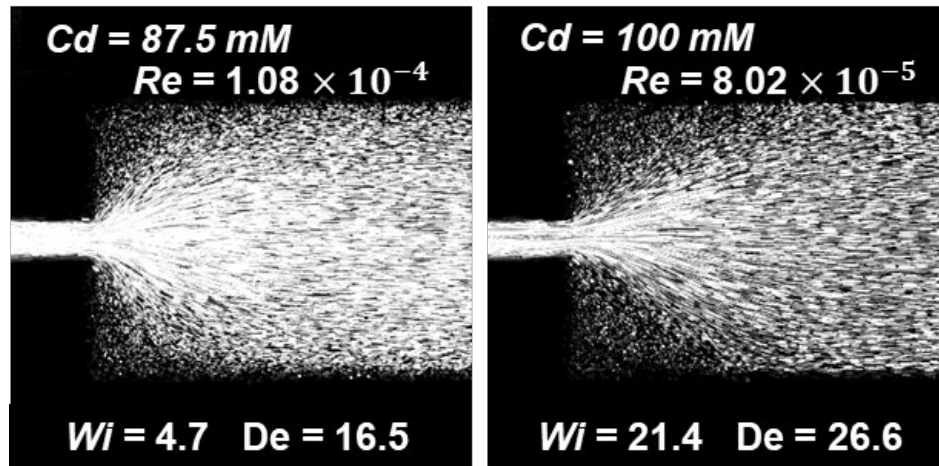


**Figure 5.8.** Streak images of solutions with CTAB molar concentrations of  $C_d = 87.5$ , and 100 mM.

Several factors that influenced on the fluid flow must be investigated to find out the reason why the flow behavior was deviated from the Newtonian-like flow.

For a fully developed Newtonian-like flow (i.e. the flow at the upstream far from the contraction entry), the velocity profile is defined by the Poiseuille equation. In which, the shear rate derived by the gradient of velocity is maximum at the wall and decreases linearly to zero at the channel centerline. Considering a constant viscosity, the shear stress associated with the flow also linearly changes by shear rate with a factor of viscosity ( $\sigma = \eta \dot{\gamma}$ ). However, for a shear thinning fluid, the viscosity,  $\eta(\dot{\gamma})$  varies along a cross sectional line from the wall to the centerline because of the variation of shear rates. At the same time, the variation of viscosity leads to the change of the velocity profile, in turn, the shear rates. Therefore, there is no exact solution representing the velocity profile of a shear thinning fluid, even for a fully developed flow condition due to the interconnected influence of shear rate and viscosity on each other. The effect of shear thinning on the velocity profile of the

fully developed flow is shown in Figure 5.9.

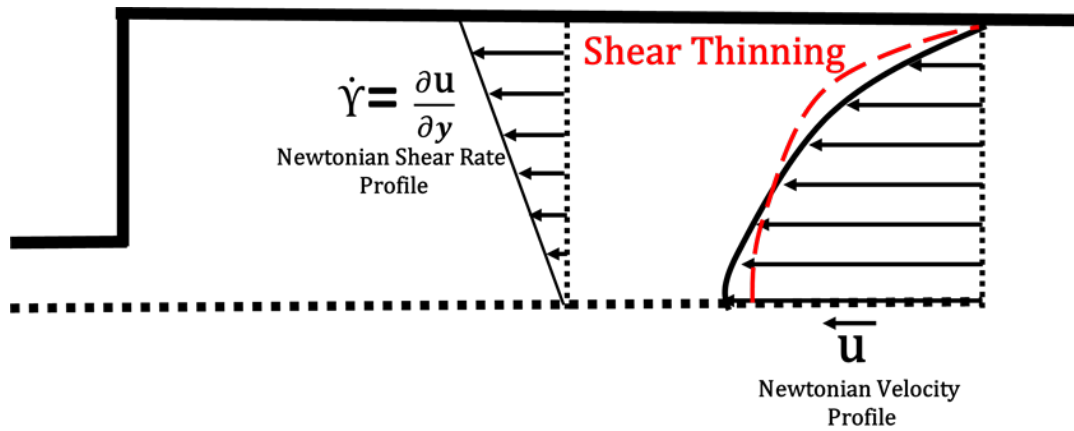


**Figure 5.9.** The velocity and shear profiles of a Newtonian-flow far from contraction entry and deviation of shear thinning fluids from the Newtonian velocity profile.

Near the channel wall, the viscosity is lower and therefore the fluid velocity is higher compared to those of the Newtonian flow. Since the average velocity of both velocity profiles is constant, the velocity of shear thinning fluid near the centerline is slower than the Newtonian fluid. To this point, the effect of shear thinning can be summarized as it increases the flow velocity at higher shear rate area of a given velocity profile.

Another factor that greatly influences the flow behavior is the geometrical effect of contraction. Even for a Newtonian-like flow, the velocity profile changes significantly close to the contraction entry region because of the conservation of mass ( $\frac{w_u}{w_c} = \frac{\bar{u}_c}{\bar{U}}$ ). The fluid velocity accelerates in the centerline area and decelerates in corner regions. Therefore, the shear rate also changes, and the maximum of shear rate is shifted from the wall to where there is the highest velocity gradient of the velocity profile.

Another factor that influences the flow of these fluids is their gel-like behavior. The steady shear rheology of these fluids (see Figure 4.5) showed high shear stresses at very low shear

rates ( $\dot{\gamma} \approx 0$ ),  $\sigma_0 \approx 0.3$  Pa for  $C_d = 87.5$  mM and  $\sigma_0 \approx 1.6$  Pa for  $C_d = 100$  mM. These stresses are considered as the yield stress ( $\sigma_0$ ) and are the amount of stress ( $\sigma$ ) that must be exceeded before the fluid start flowing:

$$\begin{cases} \dot{\gamma} = 0 & \sigma < \sigma_0 \\ \sigma - \sigma_0 = \eta(\dot{\gamma})\dot{\gamma} & \sigma \geq \sigma_0 \end{cases} \quad (5.9)$$

Therefore, in case the shear stress associated with the flow in upstream corners is in the order of the yield stress, a significant reduction of velocity is expected.

To investigate the effect of contraction entry, the velocity and shear rate profiles of a Newtonian-like flow ( $C_d = 50$  mM) were measured from the contraction entry area. Figure 5.10A shows the normalized velocity profiles along the perpendicular lines to the centerline that are fixed at the distances of  $\bar{x} = \frac{x}{w_c} = -2, -1, \text{ and } -0.5$  from the contraction entry. The velocity profiles are normalized by the average nominal velocity of the fluid in the upstream channel,  $\bar{U} = \frac{Q}{w_u H}$  where  $Q = 0.2$  mL/h and  $w_u$  is the width of contracted upstream channel. The normalized velocity profiles are plotted as a function of the normalized distance from the centerline ( $0 \leq \bar{y} = \frac{y}{w_c} \leq 4$ ) as shown in the inset of Figure 5.10A). The fluid velocity in the area near the centerline (i.e.  $0 < \bar{y} < 1$ ) increased significantly as the fluid approached toward the contraction entry like from  $\bar{x} = -2$  to  $\bar{x} = -0.5$ . On the other hand, the fluid velocity in the corner area (i.e.  $2 < \bar{y} < 4$ ) slowed down. The shear rates were also influenced by the contraction because of the change of velocity profiles as shown in Figure 5. 10B. Increased shear rates were observed in the range of  $0.2 < \bar{y} < 1.2$  whereas in corner areas ( $2 < \bar{y} < 4, -1 < \bar{x} < 0$ ) shear rates decreased significantly and are in the order of  $\dot{\gamma} < 0.1$ .

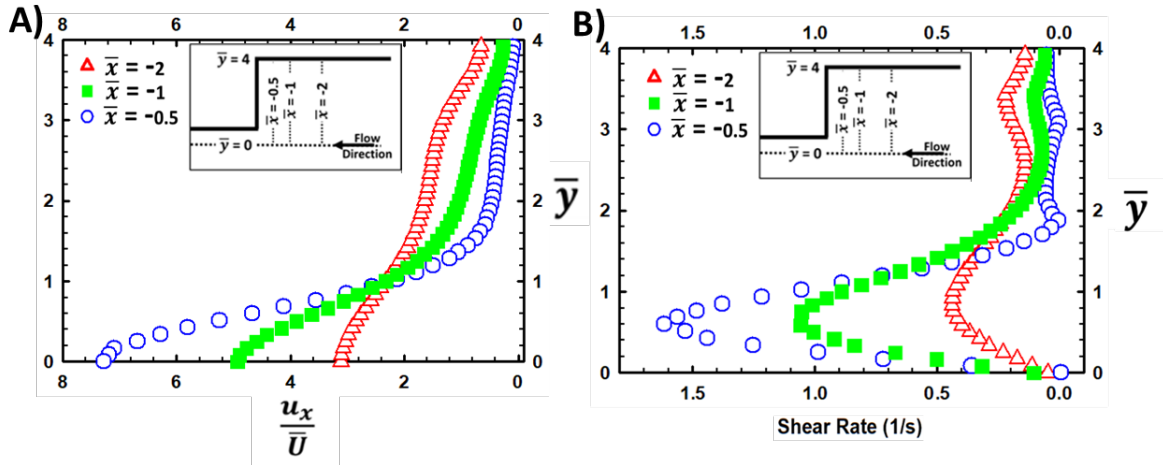


**Figure 5.10.** Profiles of A) the normalized velocity and B) shear rate for a Newtonian-like flow along the lines with the fixed distance from the contraction entry.

In case the test solution of  $C_d = 50$  mM is replaced by a shear thinning fluid, the variation of the velocity profiles near the contraction entry would increase even further. In the region of  $0.2 < \bar{y} < 1.2$  where the shear rate was high as shown in Figure 5.10B, the fluid viscosity decreased by the shear thinning effect when the fluid velocity increased. Contrarily, as the fluid velocity in the corner areas ( $2 < \bar{y} < 4$ ,  $-1 < \bar{x} < 0$ ) are expected to decrease further to the range of  $\dot{\gamma} \ll 0.1$ .

For the test solution of  $C_d = 100$  mM, considering its zero-shear viscosity,  $\eta_0 = 121$  Pa.s, the shear rates associated with the flow of the corner area must be higher than at least  $\dot{\gamma} =$

$$\frac{\sigma_0}{\eta_0} = \frac{1.6}{121} = 0.013 \text{ s}^{-1} \text{ to generate the shear stress that exceeds the yield stress of the fluid.}$$

Similarly, for the solution of  $C_d = 87.5$ , the required shear rate to exceed the yield stress is

$$\dot{\gamma} = \frac{\sigma_0}{\eta_0} = \frac{0.3}{21} = 0.014 \text{ s}^{-1}. \text{ Even for the shear stress higher than the yield stress, the relation}$$

of the shear stress to the shear rates and viscosity is described by  $\sigma - \sigma_0 = \eta(\dot{\gamma})\dot{\gamma}$ . Since

the shear rates in the corner areas ( $\dot{\gamma} \ll 0.1$ ) were in the order of those that were required to overcome the yield stresses, the yield stress caused the reduction of velocities.

### 5.7. Quasi-Static Secondary Flow Regions

At the higher range of volumetric flow rates, it was observed that the fluid in the corner areas stayed almost no flow condition (i.e. quasi-static state) and the quasi-static flow regions were completely separated from the main flow. Figure 5.11 shows representative streak images of WMS ( $C_d = 87.5$  and  $100$  mM) at  $Q = 1$  mL/h. To the best of our knowledge, this is the first time to report this type of fluidic phenomenon that showed the no-flow condition at the contraction corners instead of the well-known corner vortices.

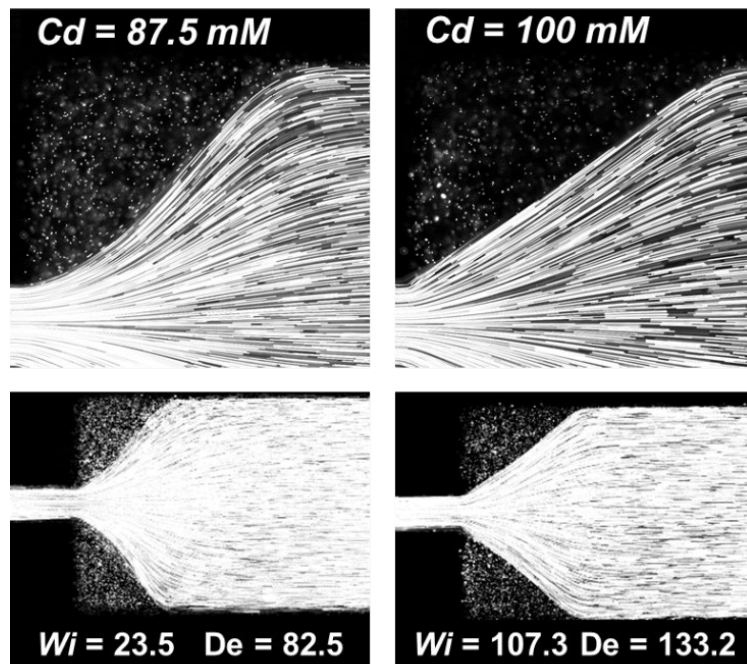


**Figure 5.11.** Streak images of WMS with the CTAB molar concentrations of  $C_d = 87.5$ , and  $100$  mM.

Figure 5.12 shows the profile of shear rate for the test solution of  $C_d = 100$  mM at  $Q = 1$  mL/h, along the perpendicular lines to the centerline that are fixed at the distances of  $\bar{x} = -$

2, -1, and -0.5 from the contraction entry. The maximum shear rate for each perpendicular lines is marked with a cross symbol on the inset of Figure 5.12. The local areas with high shear rates match well with the interface area between the main flow and the secondary no-flow regions. The shear rates applied to the fluid in the interface are in the range of shear rates in which the flow showed the shear banding phenomena (see Figure 4.5).

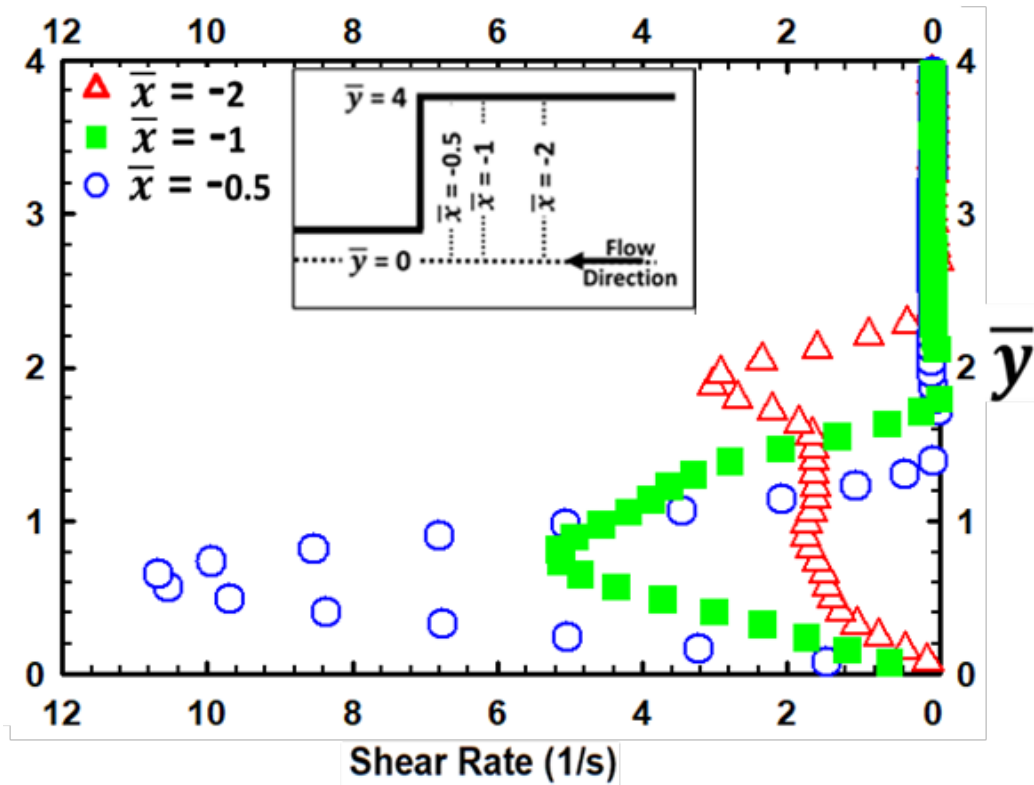


**Figure 5.12.** The profiles of shear rates for the test solutions of  $C_d = 100$  mM along the perpendicular lines to the channel centerline at the fixed distance from the contraction entry.

Therefore, the shear banding phenomena is the underlying reason for the separation of the secondary no-flow region from the main flow. Highly entangled network of micelles forms at the interface area close to the side of the secondary no-flow region, and a low viscosity

phase of micelles are formed on the side of the main flow (see Figure 5.13). In addition, the yield stress of the fluid at the corner areas is the reason why the fluid did not flow at small shear rates that would be expected due to the transition of momentum from the main flow to the corner area.

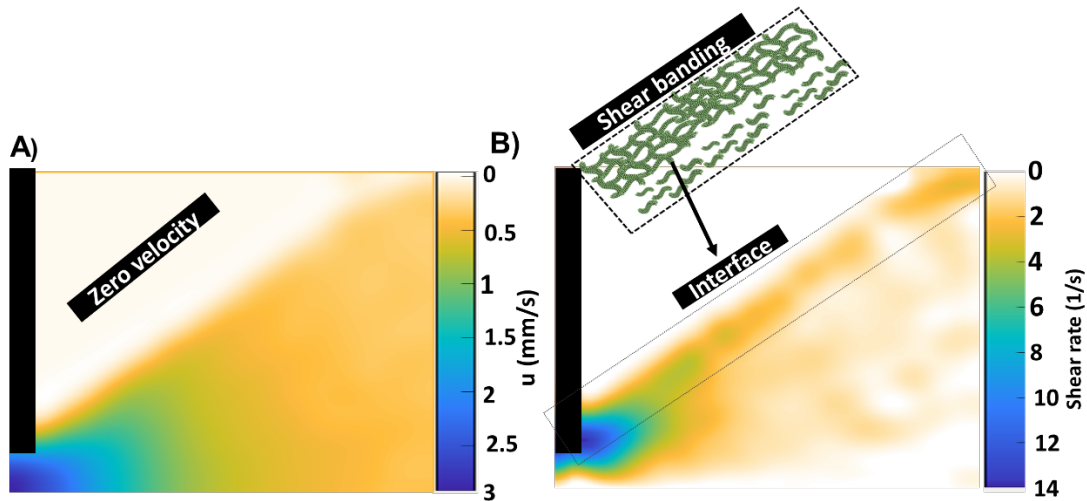


**Figure 5.13.** Maps of A) velocity and B) shear rates at the contraction entry for the test solution of  $C_d = 100 \text{ mM}$  at  $Q = 1 \text{ mL/h}$ .

As the flow rate increased, the length of quasi-static secondary flow region also increased. In Figure 5.14A and B, the normalized length of the region is plotted as a function of the  $Wi$  and  $De$  numbers, respectively. In contrast to what was observed for the corner vortices, the length of quasi-static secondary flow regions showed a close correlation only with the extensional relaxation time, which is reflected in the  $De$  number. That is attributed to the flow separation in the interface of the main and secondary flow regions (i.e. shear banding). At this flow regime, the elastic stress relaxation no longer occurred in the corner areas, and the elastic stresses in the main flow determined the flow pattern.

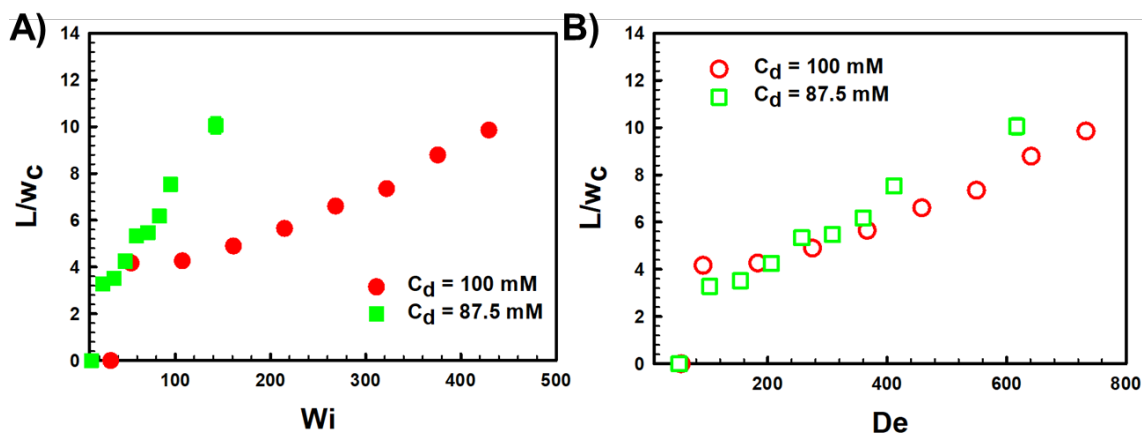


**Figure 5.14.** The normalized length of quasi-static secondary flow regions as a function of A)  $Wi$  number and B)  $De$  number.

### 5.8. Conclusions

In this study, the microscopic contraction flow of viscoelastic WMS solutions with different rheological properties has been investigated experimentally. The non-dimensional numbers,  $Wi$  and  $De$  were calculated based on the shear and extensional relaxation times, respectively. At the low range of volumetric flow rates, the solutions with  $C_d \leq 75$  mM showed the Newtonian-like flows. The transition from the Newtonian-like flow to the elastic-induced flow could not be described by a critical  $De$  or  $Wi$  number. Instead, this transition was found to be closely correlated with the viscoelastic  $Ma$  number as the transition was observed when the viscoelastic  $Ma$  number exceeded the unity ( $Ma \approx 1$ ). In case  $Ma > 1$ , the corner vortices were observed. We also found that the length of corner vortices was closely correlated with the product of  $De$  number and the ratio of extensional to shear relaxation times.

For gel-like shear banding WMS ( $87.5 \text{ mM} \leq C_d$ ), a deviation from the Newtonian-like behaviors has been observed even at low volumetric flow rates. A significant reduction of flow velocity was observed in upstream contraction corners for these solutions. The role of

contraction entry, the shear thinning behavior, and the yield stress of these gel-like solutions on their flow behavior have been discussed. The deviation from the Newtonian-flow is attributed to the role of yield stress of gel-like fluids. In upstream contraction corners, the shear rates associated with the flow were considerably low due to the effect of contraction entry and shear thinning.

At higher flow rates, regions of quasi-static fluids appeared in upstream contraction corners that were separated from the main flow. Local shear rates were found considerably high in the interface of the main flow and secondary regions. These shear rates were higher than the critical shear rate of the shear banding phenomena. Therefore, we suggested that the shear banding phenomena occurred in the interface between the main flows and the secondary flow regions. In the secondary flow regions, the small shear rates that would be expected due the momentum transfer from the main flow, are suppressed by the yield stress of gel-like WMS.

The length of quasi-static fluid region increased with higher flow rates and showed a close correlation with De number (Figure 5.14B). Unlike the corner vortices, because of the separation resulted from the shear banding in the interface of main flow and secondary region, the secondary flows changed the geometry from the sudden contraction to a gradual contraction geometry. This is a possible reason for that the length of secondary flows was not influenced by the ratio of relaxation times.

## VI. CONCLUSIONS AND RECOMMENDATIONS

The shear and extensional rheological characteristics of wormlike micellar solutions (WMS) that were prepared by cetyltrimethylammonium bromide (CTAB) and sodium salicylate (NaSal) ( $R = 0.32$ ,  $50 \text{ mM} \leq C_d \leq 100 \text{ mM}$ ) were investigated experimentally. Microscopic fluidic behaviors of these solutions flowing through a contraction geometry were quantitatively investigated using fluorescent streak imaging and microparticle image velocimetry ( $\mu$ -PIV) techniques. The notable results of the study are summarized in the following sections.

### 6.1. The Influence of Shear and Extensional Relaxation Times on the Contraction Flow

The shear relaxation time ( $\lambda$ ) of WMS was measured using the shear oscillatory measurement. The measured relaxation time increased with higher surfactant concentration ( $C_d$ ) from  $\lambda = 0.02 \text{ s}$  at  $C_d = 50 \text{ mM}$  to  $\lambda = 6.1 \text{ s}$  at  $C_d = 100 \text{ mM}$ . The longer relaxation time is attributed to the formation of highly entangled networks of wormlike micelles at higher  $C_d$ . The extensional relaxation time ( $\lambda_E$ ) of WMS was measured by dripping-onto-substrate (DoS) rheometry, and the extensional relaxation time also increased ( $1.2 \text{ s} \leq \lambda_E \leq 7.5 \text{ s}$ ) for higher  $C_d$  ( $50 \text{ mM} \leq C_d \leq 100 \text{ mM}$ ) because of the same reason.

The product of deformation rate and relaxation time ( $\lambda\dot{\gamma}$ ) quantifies the ratio of elastic to viscous forces associated with the flow, which were calculated based on either shear or extensional relaxation times. The resulted non-dimensional number that was calculated from the latter was called Deborah number ( $De = \lambda_E\dot{\gamma}$ ). The other non-dimensional number calculated from the former was named as Weissenberg number ( $Wi = \lambda\dot{\gamma}$ ) in this study. The  $De$  number showed better correlation with the flow behavior in terms of the length for

quasi-static secondary flow regions. Indeed, integrating the De number in the calculation of viscoelastic Mach numbers (Ma) revealed the onset of secondary flows at  $Ma \approx 1$ . Therefore, it should be noted that the extensional relaxation time provides better estimation of the ratio of elastic to viscous forces in the flow.

## 6.2. The Ratio of Relaxation Times and its Effect on the Contraction Flow

Comparing the relation of  $C_d$  with the shear and extensional relaxation times, quite contrasting relation was observed that the ratio of extensional to shear relaxation times ( $\frac{\lambda_E}{\lambda}$ ) decreased with higher  $C_d$  like  $\frac{\lambda_E}{\lambda} \approx 60$  for  $C_d = 50$  mM and  $\frac{\lambda_E}{\lambda} \approx 1.2$  for  $C_d = 100$  mM. High values of  $\frac{\lambda_E}{\lambda}$  were also reported by Sachsenheimer *et al.*<sup>32</sup> for CTAB/NaSal solutions with  $R < 1$  and were related to the formation of elongation induced structures (EIS) during the extensional deformation of WMS. In their study, it was observed that lower  $R$  resulted in higher  $\frac{\lambda_E}{\lambda}$ . In this study, it was evidenced that lower  $C_d$  also resulted in higher  $\frac{\lambda_E}{\lambda}$ . The decrease of  $\frac{\lambda_E}{\lambda}$  for higher  $C_d$  is related to the role of higher entanglements in these solutions, which was evidenced by higher zero-shear viscosity and longer shear relaxation time. These entanglement points reduce the ability of wormlike micelles to move and align in the elongation direction to form EIS structures. In this study, we found that the product of relaxation time ratio ( $\frac{\lambda_E}{\lambda}$ ) and De number showed a close correlation to the length of corner vortices obtained from different test fluids compared to previous studies that used De and Wi numbers showing irrelevant correlation with the vortex length. The relaxation time ratio,  $\frac{\lambda_E}{\lambda}$  can be considered as a factor that influences the rate of stress built up in the main flow compared to the secondary flows. We found that the vortex length for fluids with

higher  $\frac{\lambda_E}{\lambda}$  grew at a faster rate (regarding De numbers) compared to those with lower  $\frac{\lambda_E}{\lambda}$ .

### 6.3. Role of Shear Thinning and Yield Stress on the Contraction Flow

The steady shear measurement of WMS showed that the zero-shear viscosity ( $\eta_0$ ) of solutions increased by 5 orders of magnitude ( $0.03 \text{ Pa}\cdot\text{s} \leq \eta_0 \leq 121 \text{ Pa}\cdot\text{s}$ ) by increasing  $C_d$ , whereas the ultimate viscosity of the solutions was in the same order ( $\eta_\infty \approx 0.03$ ). The higher  $\eta_0$  is related to higher levels of entanglement at higher  $C_d$ , while at the very high shear rates, the entanglements break due to the high shear rates applied to the flow and the viscosity of solutions reached to comparable values of ultimate viscosity. The shear thinning behavior was thus related to the levels of entanglement in the flow and prominently stronger for the solutions with higher  $C_d$ . The flows of test fluids with higher  $C_d$  in this study also showed significantly high yield stresses,  $\sigma_0 \approx 0.3 \text{ Pa}$  for  $C_d = 87.5 \text{ mM}$  and  $\sigma_0 \approx 1.6 \text{ Pa}$  for  $C_d = 100 \text{ mM}$ . In contraction flow experiment, the flow behavior of these two test fluids deviated from the Newtonian-like flows that were observed for  $C_d \leq 75 \text{ mM}$ , even under low volumetric flow rates. While the flows were steady, a reduction of flow velocity was observed in the upstream corner areas of the contraction entry. Our hypothesis was that the shear thinning and the yield stress of these fluids influenced the flow behavior. While there was no direct method to test the hypothesis, we adopted the following method: firstly, the role of contraction entry influencing the velocity and shear rate profiles of a Newtonian-like flow ( $C_d = 50 \text{ mM}$  at  $Q = 0.2 \text{ mL/h}$ ) were investigated. The shear rates at the upstream corners ( $2 < \bar{y} < 4$ ,  $-1 < \bar{x} < 0$ ) were  $\dot{\gamma} < 0.1$ . Then, the role of shear thinning behavior resulting in further decrease of shear rates and velocities in upstream corners was discussed. Therefore, it was concluded that the shear rates in corner areas ( $\dot{\gamma} \ll 0.1$ ) were in the order of the minimum shear rates that were required for the

test fluids to overcome their yield stress to start flowing ( $\dot{\gamma} = \frac{\sigma_0}{\eta_0} = \frac{1.6}{121} = 0.013 \text{ s}^{-1}$  for  $C_d = 100 \text{ mM}$  and  $\dot{\gamma} = \frac{\sigma_0}{\eta_0} = \frac{0.3}{21} = 0.014 \text{ s}^{-1}$  for  $C_d = 87.5 \text{ mM}$ ). Thus, the yield stresses of the fluids are in order of the stresses associated with their flow at upstream corners, and  $\sigma_0$  was a determining factor ( $\sigma - \sigma_0 = \eta(\dot{\gamma}) \dot{\gamma}$ ) that caused the reduction of velocity in the corner areas.

#### 6.4. Quasi-Static Secondary Flow Regions and the Role of Shear Banding

For higher applied flow rates, a new type of flow behavior for the test fluids with  $C_d \geq 87.5 \text{ mM}$  is documented. To the best of our knowledge, the fluidic behavior had not been reported in the literature. In this flow regime, regions with quasi-static secondary flow regions have appeared instead of corner vortices. The local areas with high shear rates matched with the location of interface area between the main flow and the secondary regions. The shear rates applied to the fluid in the interface were in the range of shear rates that the flow showed shear banding phenomena. Therefore, we suggested that the shear banding phenomena occurred in the interface between the main flow and the secondary region. A highly entangled network of micelles was formed at the interface area close to the side of the secondary flow region and a low viscosity phase of micelles was formed on the side of the main flow. Indeed, we observed that the high yield stresses of test fluids at lower volumetric flow rates (i.e.  $Q = 0.2 \text{ mL/h}$ ) resulted in reduced flow velocities in the corner areas. Two different phases are considered under the same shear stress ( $\sigma = \eta_{\text{higher}} \dot{\gamma}_{\text{lower}} = \eta_{\text{lower}} \dot{\gamma}_{\text{higher}}$ ) when the shear banding was observed. In the higher viscous phase, which is close to the secondary flow side, lower shear rates are expected compared to the high shear rates at the lower viscous phase. Since we observed the quasi-static region at the corner area, we concluded that the yield stress of the test fluid at the

corners further surpassed even the low shear rates that are expected at high viscous phase of the shear banded fluids.

### **6.5. Suggestions for Future Studies**

In this study, we evidenced large variation of extensional to shear relaxation time ratio ( $\frac{\lambda_E}{\lambda}$ ) for test fluids with different surfactant concentration. The ratio was found to influence the length of vortices. Birefringence measurements in the future study would provide valuable information on the degree of alignment of wormlike micellar chains in contraction flows. Therefore, the results of birefringence measurement can show whether the fluid with lower  $C_d$  results in higher degree of micellar structures (i.e., formation of EIS) in the fluid flowing through the contraction geometry. Moreover, it can provide more insight to the underlying reason for the formation of quasi-static secondary flow regions.

As we evidenced a new type of flow behavior that was associated with the formation of quasi-static secondary flow regions instead of corner vortices, the degree of pressure drop associated with this flow regime is still unclear. It is well known that viscoelastic contraction flows forming corner vortices are associated with an extra pressure loss compared to the Newtonian flow under the similar flow condition. A future study is suggested to measure the pressure loss of WMS contraction flows that form quasi-static secondary flows to compare the results with the viscoelastic contraction flows that form corner vortices.

The experimental data presented by this study showed that the shear thinning phenomena resulted in the reduction of flow velocity in the upstream corner areas. Additionally, the shear banding phenomena led to the separation between the main and secondary flows.

These data can be used for validation of future modeling and numerical simulations for the contraction flow of viscoelastic solutions including WMS that show the shear thinning and shear banding phenomena.

## REFERENCES

1. Hertel, D.; Münstedt, H., Dependence of the secondary flow of a low-density polyethylene on processing parameters as investigated by laser-Doppler velocimetry. *Journal of Non-Newtonian Fluid Mechanics* **2008**, *153* (2), 73-81.
2. Pérez-Gonzalez, J.; Pérez-Trejo, L.; de Vargas, L.; Manero, O., Inlet instabilities in the capillary flow of polyethylene melts. *Rheologica Acta* **1997**, *36* (6), 677-685.
3. Combeaud, C.; Vergnes, B.; Merten, A.; Hertel, D.; Münstedt, H., Volume defects during extrusion of polystyrene investigated by flow induced birefringence and laser-Doppler velocimetry. *Journal of Non-Newtonian Fluid Mechanics* **2007**, *145* (2-3), 69-77.
4. Cooper-White, J. J.; Fagan, J. E.; Tirtaatmadja, V.; Lester, D. R.; Boger, D. V., Drop formation dynamics of constant low-viscosity, elastic fluids. *Journal of Non-Newtonian Fluid Mechanics* **2002**, *106* (1), 29-59.
5. Browne, C. A.; Shih, A.; Datta, S. S., Pore-Scale Flow Characterization of Polymer Solutions in Microfluidic Porous Media. *arXiv preprint arXiv:1909.05688* **2019**.
6. Ober, T. J.; Haward, S. J.; Pipe, C. J.; Soulages, J.; McKinley, G. H., Microfluidic extensional rheometry using a hyperbolic contraction geometry. *Rheologica Acta* **2013**, *52* (6), 529-546.
7. Pipe, C. J.; McKinley, G. H., Microfluidic rheometry. *Mechanics Research Communications* **2009**, *36* (1), 110-120.
8. Meller, M.; Luciani, A.; Sarioglu, A.; Månson, J. A. E., Flow through a convergence. Part 1: Critical conditions for unstable flow. *Polymer Engineering & Science* **2002**, *42* (3), 611-633.
9. Kim, S.; Dealy, J. M., Gross melt fracture of polyethylene. I: A criterion based on tensile stress. *Polymer Engineering & Science* **2002**, *42* (3), 482-494.
10. Owens, R. G.; Phillips, T. N., *Computational rheology*. World Scientific: 2002; Vol. 14.
11. Rothstein, J. P. The stability of viscoelastic fluids in complex flows: the role of shear and extensional rheology. Massachusetts Institute of Technology, 2001.
12. Rothstein, J. P.; McKinley, G. H., The axisymmetric contraction–expansion: the role of extensional rheology on vortex growth dynamics and the enhanced pressure drop. *Journal of non-newtonian fluid mechanics* **2001**, *98* (1), 33-63.
13. Oliveira, M. S.; Oliveira, P. J.; Pinho, F. T.; Alves, M. A., Effect of contraction ratio upon viscoelastic flow in contractions: the axisymmetric case. *Journal of Non-Newtonian Fluid Mechanics* **2007**, *147* (1-2), 92-108.

14. Vrentas, J.; Duda, J., Flow of a Newtonian fluid through a sudden contraction. *Applied Scientific Research* **1973**, *28* (1), 241-260.
15. Boger, D.; Hur, D.; Binnington, R., Further observations of elastic effects in tubular entry flows. *Journal of non-Newtonian fluid mechanics* **1986**, *20*, 31-49.
16. Evans, R. E.; Walters, K., Further remarks on the lip-vortex mechanism of vortex enhancement in planar-contraction flows. *Journal of Non-Newtonian Fluid Mechanics* **1989**, *32* (1), 95-105.
17. Evans, R. E.; Walters, K., Flow characteristics associated with abrupt changes in geometry in the case of highly elastic liquids. *Journal of Non-Newtonian Fluid Mechanics* **1986**, *20*, 11-29.
18. Boger, D., Viscoelastic flows through contractions. *Annual review of fluid mechanics* **1987**, *19* (1), 157-182.
19. Rodd, L. E.; Scott, T. P.; Boger, D. V.; Cooper-White, J. J.; McKinley, G. H., The inertio-elastic planar entry flow of low-viscosity elastic fluids in micro-fabricated geometries. *Journal of Non-Newtonian Fluid Mechanics* **2005**, *129* (1), 1-22.
20. Rodd, L. E.; Cooper-White, J. J.; Boger, D. V.; McKinley, G. H., Role of the elasticity number in the entry flow of dilute polymer solutions in micro-fabricated contraction geometries. *Journal of Non-Newtonian Fluid Mechanics* **2007**, *143* (2), 170-191.
21. Haward, S. J.; Li, Z.; Lighter, D.; Thomas, B.; Odell, J. A.; Yuan, X.-F., Flow of dilute to semi-dilute polystyrene solutions through a benchmark 8: 1 planar abrupt micro-contraction. *Journal of non-newtonian fluid mechanics* **2010**, *165* (23-24), 1654-1669.
22. Li, Z.; Yuan, X.-F.; Haward, S. J.; Odell, J. A.; Yeates, S., Non-linear dynamics of semi-dilute polydisperse polymer solutions in microfluidics: a study of a benchmark flow problem. *Journal of non-newtonian fluid mechanics* **2011**, *166* (16), 951-963.
23. Lanzaro, A.; Yuan, X.-F., Effects of contraction ratio on non-linear dynamics of semi-dilute, highly polydisperse PAAm solutions in microfluidics. *Journal of non-newtonian fluid mechanics* **2011**, *166* (17-18), 1064-1075.
24. Lanzaro, A.; Yuan, X.-F., A quantitative analysis of spatial extensional rate distribution in nonlinear viscoelastic flows. *Journal of Non-Newtonian Fluid Mechanics* **2014**, *207*, 32-41.
25. Lee, D.; Kim, Y.; Ahn, K. H., Effect of elasticity number and aspect ratio on the vortex dynamics in 4: 1 micro-contraction channel flow. *Korea-Australia Rheology Journal* **2014**, *26* (3), 335-340.

26. Sankaran, A. K.; Dros, D. A.; Meerman, H. J.; Picken, S. J.; Kreutzer, M. T., Increasing the stability of high contraction ratio flow of Boger fluids by pre-deformation. *Journal of Non-Newtonian Fluid Mechanics* **2013**, *196*, 27-35.
27. Hemminger, O. L.; Boukany, P. E.; Wang, S.-Q.; Lee, L., Flow pattern and molecular visualization of DNA solutions through a 4: 1 planar micro-contraction. *Journal of non-newtonian fluid mechanics* **2010**, *165* (23-24), 1613-1624.
28. White, S. A.; Baird, D. G., The importance of extensional flow properties on planar entry flow patterns of polymer melts. *Journal of Non-Newtonian Fluid Mechanics* **1986**, *20*, 93-101.
29. Kang, K. Microfluidics of complex fluids. The Ohio State University, 2003.
30. Wang, J.; Feng, Y.; Agrawal, N. R.; Raghavan, S. R., Wormlike micelles versus water-soluble polymers as rheology-modifiers: similarities and differences. *Physical chemistry chemical physics* **2017**, *19* (36), 24458-24466.
31. Jafari Nodoushan, E.; Yi, T.; Lee, Y. J.; Kim, N., Wormlike Micellar Solutions, Beyond the Chemical Enhanced Oil Recovery Restrictions. *Fluids* **2019**, *4* (3), 173.
32. Sachsenheimer, D.; Oelschlaeger, C.; Müller, S.; Küstner, J.; Bindgen, S.; Willenbacher, N., Elongational deformation of wormlike micellar solutions. *Journal of Rheology* **2014**, *58* (6), 2017-2042.
33. Berret, J.-F., Rheology of wormlike micelles: Equilibrium properties and shear banding transitions. In *Molecular gels*, Springer: 2006; pp 667-720.
34. Maibaum, L.; Dinner, A. R.; Chandler, D., Micelle formation and the hydrophobic effect. *The Journal of Physical Chemistry B* **2004**, *108* (21), 6778-6781.
35. Cates, M.; Candau, S., Statics and dynamics of worm-like surfactant micelles. *Journal of Physics: Condensed Matter* **1990**, *2* (33), 6869.
36. Israelachvili, J. N.; Mitchell, D. J.; Ninham, B. W., Theory of self-assembly of hydrocarbon amphiphiles into micelles and bilayers. *Journal of the Chemical Society, Faraday Transactions 2: Molecular and Chemical Physics* **1976**, *72*, 1525-1568.
37. Zhang, J.; Li, X.; Li, X., Stimuli-triggered structural engineering of synthetic and biological polymeric assemblies. *Progress in Polymer Science* **2012**, *37* (8), 1130-1176.
38. Chu, Z.; Dreiss, C. A.; Feng, Y., Smart wormlike micelles. *Chemical Society Reviews* **2013**, *42* (17), 7174-7203.
39. Khalil, R. A.; Al-hakam, A. Z., Theoretical estimation of the critical packing parameter of amphiphilic self-assembled aggregates. *Applied surface science* **2014**, *318*, 85-89.

40. Dreiss, C. A., Wormlike micelles: where do we stand? Recent developments, linear rheology and scattering techniques. *Soft Matter* **2007**, 3 (8), 956-970.
41. Candau, S.; Oda, R., Linear viscoelasticity of salt-free wormlike micellar solutions. *Colloids and Surfaces A: Physicochemical and Engineering Aspects* **2001**, 183, 5-14.
42. Rehage, H.; Hoffmann, H., Rheological properties of viscoelastic surfactant systems. *The Journal of Physical Chemistry* **1988**, 92 (16), 4712-4719.
43. Adams, A. Multiscale Investigation of the Nonlinear Rheology of Wormlike Micelles. 2018.
44. Acharya, D. P.; Kunieda, H., Wormlike micelles in mixed surfactant solutions. *Advances in Colloid and Interface Science* **2006**, 123-126, 401-413.
45. Zana, R.; Kaler, E. W., *Giant micelles: properties and applications*. CRC press: 2007; Vol. 140.
46. Dalhaimer, P.; Bates, F. S.; Discher, D. E., Single molecule visualization of stable, stiffness-tunable, flow-conforming worm micelles. *Macromolecules* **2003**, 36 (18), 6873-6877.
47. Bellour, M.; Knaebel, A.; Munch, J.; Candau, S., Scattering properties of salt-free wormlike micellar solutions. *The European Physical Journal E* **2000**, 3 (2), 111-121.
48. Zhao, Y.; Shen, A. Q.; Haward, S. J., Flow of wormlike micellar solutions around confined microfluidic cylinders. *Soft Matter* **2016**, 12 (42), 8666-8681.
49. Zhao, Y.; Haward, S. J.; Shen, A. Q., Rheological characterizations of wormlike micellar solutions containing cationic surfactant and anionic hydrotropic salt. *Journal of Rheology* **2015**, 59 (5), 1229-1259.
50. Cates, M., Reptation of living polymers: dynamics of entangled polymers in the presence of reversible chain-scission reactions. *Macromolecules* **1987**, 20 (9), 2289-2296.
51. Cates, M. E.; Fielding, S. M., Rheology of giant micelles. *Advances in Physics* **2006**, 55 (7-8), 799-879.
52. Osswald, T.; Rudolph, N., Polymer rheology. *Carl Hanser, München* **2015**.
53. de Gennes, P.-G., Reptation of a polymer chain in the presence of fixed obstacles. *The journal of chemical physics* **1971**, 55 (2), 572-579.
54. Cates, M., Nonlinear viscoelasticity of wormlike micelles (and other reversibly breakable polymers). *Journal of Physical Chemistry* **1990**, 94 (1), 371-375.

55. Candau, S.; Khatory, A.; Lequeux, F.; Kern, F., Rheological behaviour of wormlike micelles: effect of salt content. *Le Journal de Physique IV* **1993**, 3 (C1), C1-197-C1-209.
56. Gaudino, D.; Pasquino, R.; Grizzuti, N., Adding salt to a surfactant solution: Linear rheological response of the resulting morphologies. *Journal of Rheology* **2015**, 59 (6), 1363-1375.
57. Oelschlaeger, C.; Schopferer, M.; Scheffold, F.; Willenbacher, N., Linear-to-branched micelles transition: A rheometry and diffusing wave spectroscopy (DWS) study. *Langmuir* **2009**, 25 (2), 716-723.
58. Gabbanelli, S.; Drazer, G.; Koplik, J., Lattice Boltzmann method for non-Newtonian (power-law) fluids. *Physical review E* **2005**, 72 (4), 046312.
59. Galindo-Rosales, F.; Rubio-Hernández, F.; Sevilla, A., An apparent viscosity function for shear thickening fluids. *Journal of Non-Newtonian Fluid Mechanics* **2011**, 166 (5-6), 321-325.
60. Kang, H.; Lee, Y.-J., A three-species model for wormlike micellar fluids. *Computers & Mathematics with Applications* **2016**, 71 (7), 1349-1363.
61. Galindo-Rosales, F.; Rubio-Hernández, F.; Sevilla, A.; Ewoldt, R. H., How Dr. Malcom M. Cross may have tackled the development of “An apparent viscosity function for shear thickening fluids”. *Journal of Non-Newtonian Fluid Mechanics* **2011**, 166 (23-24), 1421-1424.
62. Cross, M. M., Rheology of non-Newtonian fluids: a new flow equation for pseudoplastic systems. *Journal of colloid science* **1965**, 20 (5), 417-437.
63. Bruinsma, R.; Gelbart, W. M.; Ben-Shaul, A., Flow-induced gelation of living (micellar) polymers. *The Journal of chemical physics* **1992**, 96 (10), 7710-7727.
64. Barentin, C.; Liu, A., Shear thickening in dilute solutions of wormlike micelles. *EPL (Europhysics Letters)* **2001**, 55 (3), 432.
65. Lindner, P.; Bewersdorff, H.; Heen, R.; Sittart, P.; Thiel, H.; Langowski, J.; Oberthür, R., Drag-reducing surfactant solutions in laminar and turbulent flow investigated by small-angle neutron scattering and light scattering. In *Trends in Colloid and Interface Science IV*, Springer: 1990; pp 107-112.
66. Boltenhagen, P.; Hu, Y.; Matthys, E.; Pine, D., Observation of bulk phase separation and coexistence in a sheared micellar solution. *Physical review letters* **1997**, 79 (12), 2359.
67. Rojas, M. R.; Müller, A. J.; Sáez, A. E., Shear rheology and porous media flow of wormlike micelle solutions formed by mixtures of surfactants of opposite charge. *Journal of Colloid and Interface Science* **2008**, 326 (1), 221-226.

68. Larson, R.; Magda, J., Coil-stretch transitions in mixed shear and extensional flows of dilute polymer solutions. *Macromolecules* **1989**, *22* (7), 3004-3010.
69. De Gennes, P., Coil-stretch transition of dilute flexible polymers under ultrahigh velocity gradients. *The Journal of Chemical Physics* **1974**, *60* (12), 5030-5042.
70. Tropea, C.; Yarin, A. L., *Springer handbook of experimental fluid mechanics*. Springer Science & Business Media: 2007.
71. Spiegelberg, S. H.; McKinley, G. H., Stress relaxation and elastic decohesion of viscoelastic polymer solutions in extensional flow. *Journal of Non-Newtonian Fluid Mechanics* **1996**, *67*, 49-76.
72. Bhardwaj, A.; Miller, E.; Rothstein, J. P., Filament stretching and capillary breakup extensional rheometry measurements of viscoelastic wormlike micelle solutions. *Journal of Rheology* **2007**, *51* (4), 693-719.
73. Omidvar, R.; Dalili, A.; Mir, A.; Mohammadigoushki, H., Exploring sensitivity of the extensional flow to wormlike micellar structure. *Journal of Non-Newtonian Fluid Mechanics* **2018**, *252*, 48-56.
74. White, S.; Baird, D., The importance of extensional flow properties on planar entry flow patterns of polymer melts. *Journal of Non-Newtonian Fluid Mechanics* **1986**, *20*, 93-101.
75. Musil, J.; Zatloukal, M., Historical review of secondary entry flows in polymer melt extrusion. *Polymer Reviews* **2019**, *59* (2), 338-390.
76. Olson, D. J.; Fuller, G. G., Contraction and expansion flows of Langmuir monolayers. *Journal of non-newtonian fluid mechanics* **2000**, *89* (1-2), 187-207.
77. Patience, G. S., *Experimental methods and instrumentation for chemical engineers*. Elsevier: 2017.
78. Prud'homme, R. K., *Rheological measurements*. ACS Publications: 1991.
79. Doi, M.; Edwards, S. F., *The theory of polymer dynamics*. oxford university press: 1988; Vol. 73.
80. Schramm, G., *A practical approach to rheology and rheometry*. Haake Karlsruhe: 1994.
81. Malkin, A. Y.; Isayev, A. I., *Rheology: concepts, methods, and applications*. Elsevier: 2017.
82. Omidvar, R.; Wu, S.; Mohammadigoushki, H., Detecting wormlike micellar microstructure using extensional rheology. *Journal of Rheology* **2019**, *63* (1), 33-44.

83. Dinic, J.; Sharma, V., Macromolecular relaxation, strain, and extensibility determine elastocapillary thinning and extensional viscosity of polymer solutions. *Proceedings of the National Academy of Sciences* **2019**, *116* (18), 8766-8774.
84. Dinic, J.; Jimenez, L. N.; Sharma, V., Pinch-off dynamics and dripping-onto-substrate (DoS) rheometry of complex fluids. *Lab on a Chip* **2017**, *17* (3), 460-473.
85. Dinic, J.; Jimenez, L. N.; Biagioli, M.; Estrada, A.; Sharma, V., Free Surface Flows and Extensional Rheology of Polymer Solutions. *APS* **2017**, *2017*, M1. 096.
86. Dinic, J.; Biagioli, M.; Sharma, V., Pinch-off dynamics and extensional relaxation times of intrinsically semi-dilute polymer solutions characterized by dripping-onto-substrate rheometry. *Journal of Polymer Science Part B: Polymer Physics* **2017**, *55* (22), 1692-1704.
87. Jimenez, L. N.; Dinic, J.; Parsi, N.; Sharma, V., Extensional relaxation time, pinch-off dynamics, and printability of semidilute polyelectrolyte solutions. *Macromolecules* **2018**, *51* (14), 5191-5208.
88. Castrejón-Pita, J. R.; Castrejón-Pita, A. A.; Thete, S. S.; Sambath, K.; Hutchings, I. M.; Hinch, J.; Lister, J. R.; Basaran, O. A., Plethora of transitions during breakup of liquid filaments. *Proceedings of the National Academy of Sciences* **2015**, *112* (15), 4582-4587.
89. McKinley, G. H.; Tripathi, A., How to extract the Newtonian viscosity from capillary breakup measurements in a filament rheometer. *Journal of Rheology* **2000**, *44* (3), 653-670.
90. Entov, V.; Hinch, E., Effect of a spectrum of relaxation times on the capillary thinning of a filament of elastic liquid. *Journal of Non-Newtonian Fluid Mechanics* **1997**, *72* (1), 31-53.
91. Anna, S. L.; McKinley, G. H., Elasto-capillary thinning and breakup of model elastic liquids. *Journal of Rheology* **2001**, *45* (1), 115-138.
92. Dinic, J.; Zhang, Y.; Jimenez, L. N.; Sharma, V., Extensional relaxation times of dilute, aqueous polymer solutions. *ACS Macro Letters* **2015**, *4* (7), 804-808.
93. Hansen, F.; Rødsrud, G., Surface tension by pendant drop: I. A fast standard instrument using computer image analysis. *Journal of colloid and interface science* **1991**, *141* (1), 1-9.
94. Boutelier, D.; Schrank, C.; Regenauer-Lieb, K., 2-D finite displacements and strain from particle imaging velocimetry (PIV) analysis of tectonic analogue models with TecPIV. *Solid Earth* **2019**, *10* (4), 1123-1139.

95. Thielicke, W.; Stamhuis, E., PIVlab—towards user-friendly, affordable and accurate digital particle image velocimetry in MATLAB. *Journal of Open Research Software* **2014**, *2* (1).
96. Shrestha, R. G.; Shrestha, L. K.; Aramaki, K., Wormlike micelles in mixed amino acid-based anionic/nonionic surfactant systems. *Journal of colloid and interface science* **2008**, *322* (2), 596-604.
97. Parker, A.; Fieber, W., Viscoelasticity of anionic wormlike micelles: effects of ionic strength and small hydrophobic molecules. *Soft Matter* **2013**, *9* (4), 1203-1213.
98. Hu, Y.; Boltenhagen, P.; Matthys, E.; Pine, D., Shear thickening in low-concentration solutions of wormlike micelles. II. Slip, fracture, and stability of the shear-induced phase. *Journal of Rheology* **1998**, *42* (5), 1209-1226.
99. Arenas-Gómez, B.; Garza, C.; Liu, Y.; Castillo, R., Alignment of worm-like micelles at intermediate and high shear rates. *Journal of colloid and interface science* **2020**, *560*, 618-625.
100. Walker, L. M., Rheology and structure of worm-like micelles. *Current opinion in colloid & interface science* **2001**, *6* (5-6), 451-456.
101. Mair, R.; Callaghan, P., Observation of shear banding in worm-like micelles by NMR velocity imaging. *EPL (Europhysics Letters)* **1996**, *36* (9), 719.
102. Makhloufi, R.; Decruppe, J.; Ait-Ali, A.; Cressely, R., Rheo-optical study of worm-like micelles undergoing a shear banding flow. *EPL (Europhysics Letters)* **1995**, *32* (3), 253.
103. Mohammadigoushki, H.; Muller, S. J., A flow visualization and superposition rheology study of shear-banding wormlike micelle solutions. *Soft matter* **2016**, *12* (4), 1051-1061.
104. Zheng, Z.-Y.; Li, F.-C.; Wang, L.; Li, X.-B.; Zhang, H.-N.; Cai, W.-H.; Zheng, X., Experimental study on rheological and thermophysical properties of seawater with surfactant additive—Part II: Surface tension and thermal conductivity. *International Journal of Heat and Mass Transfer* **2018**, *127*, 1367-1379.
105. Jiang, C.-X.; Li, F.-C., Experimental and numerical study of water entry supercavity influenced by turbulent drag-reducing additives. *Advances in Mechanical Engineering* **2014**, *6*, 280643.
106. Kumar, S.; Kalwar, S. A.; Abbas, G.; Awan, A. Q. In *Application of Wormlike Micelles for Mobility Control in Chemical Enhanced Oil Recovery*, Abu Dhabi International Petroleum Exhibition & Conference, Society of Petroleum Engineers: 2018.

107. Kumari, R.; Kakati, A.; Nagarajan, R.; Sangwai, J. S., Synergistic effect of mixed anionic and cationic surfactant systems on the interfacial tension of crude oil-water and enhanced oil recovery. *Journal of Dispersion Science and Technology* **2019**, *40* (7), 969-981.
108. Fardin, M.-A.; Lopez, D.; Croso, J.; Grégoire, G.; Cardoso, O.; McKinley, G.; Lerouge, S., Elastic turbulence in shear banding wormlike micelles. *Physical review letters* **2010**, *104* (17), 178303.
109. Ito, T. H.; Miranda, P. C.; Morgon, N. H.; Heerdt, G.; Dreiss, C. c. A.; Sabadini, E., Molecular variations in aromatic cosolutes: critical role in the rheology of cationic wormlike micelles. *Langmuir* **2014**, *30* (39), 11535-11542.
110. Granek, R.; Cates, M., Stress relaxation in living polymers: Results from a Poisson renewal model. *The Journal of chemical physics* **1992**, *96* (6), 4758-4767.
111. Lam, C. N.; Do, C.; Wang, Y.; Huang, G.-R.; Chen, W.-R., Structural properties of the evolution of CTAB/NaSal micelles investigated by SANS and rheometry. *Physical Chemistry Chemical Physics* **2019**, *21* (33), 18346-18351.
112. Amin, S.; Kermis, T. W.; van Zanten, R. M.; Dees, S. J.; van Zanten, J. H., Concentration fluctuations in CTAB/NaSal solutions. *Langmuir* **2001**, *17* (26), 8055-8061.
113. Inoue, T.; Inoue, Y.; Watanabe, H., Nonlinear rheology of CTAB/NaSal aqueous solutions: finite extensibility of a network of wormlike micelles. *Langmuir* **2005**, *21* (4), 1201-1208.
114. Hartmann, V.; Cressely, R., Influence of sodium salicylate on the rheological behaviour of an aqueous CTAB solution. *Colloids and Surfaces A: Physicochemical and Engineering Aspects* **1997**, *121* (2-3), 151-162.
115. Kern, F.; Zana, R.; Candau, S., Rheological properties of semidilute and concentrated aqueous solutions of cetyltrimethylammonium chloride in the presence of sodium salicylate and sodium chloride. *Langmuir* **1991**, *7* (7), 1344-1351.
116. Yamashita, A.; Mori, K.; Sawa, K.; Yamamoto, T., Creep Tests, Flow Birefringence Measurements, and Flow Visualization of Aqueous Solutions of CTAB and NaSal in Shear Flow between Parallel Plates. *Journal of Fluid Science and Technology* **2009**, *4* (3), 699-710.
117. Vasudevan, M.; Shen, A.; Khomami, B.; Sureshkumar, R., Self-similar shear thickening behavior in CTAB/NaSal surfactant solutions. *Journal of Rheology* **2008**, *52* (2), 527-550.
118. Azzouzi, H.; Decruppe, J.; Lerouge, S.; Greffier, O., Temporal oscillations of the shear stress and scattered light in a shear-banding-shear-thickening micellar solution. *The European Physical Journal E* **2005**, *17* (4), 507-514.

119. Kim, W.-J.; Yang, S.-M., Effects of sodium salicylate on the microstructure of an aqueous micellar solution and its rheological responses. *Journal of colloid and interface science* **2000**, *232* (2), 225-234.
120. Cardiel, J. J.; Dohnalkova, A. C.; Dubash, N.; Zhao, Y.; Cheung, P.; Shen, A. Q., Microstructure and rheology of a flow-induced structured phase in wormlike micellar solutions. *Proceedings of the National Academy of Sciences* **2013**, *110* (18), E1653-E1660.
121. Dubash, N.; Cheung, P.; Shen, A. Q., Elastic instabilities in a microfluidic cross-slot flow of wormlike micellar solutions. *Soft Matter* **2012**, *8* (21), 5847-5856.
122. Keller, S.; Boltenhagen, P.; Pine, D.; Zasadzinski, J., Direct observation of shear-induced structures in wormlike micellar solutions by freeze-fracture electron microscopy. *Physical review letters* **1998**, *80* (12), 2725.
123. Boltenhagen, P.; Hu, Y.; Matthys, E.; Pine, D., Inhomogeneous structure formation and shear-thickening in worm-like micellar solutions. *EPL (Europhysics Letters)* **1997**, *38* (5), 389.
124. Liu, C.-h.; Pine, D., Shear-induced gelation and fracture in micellar solutions. *Physical review letters* **1996**, *77* (10), 2121.
125. Manneville, S., Recent experimental probes of shear banding. *Rheologica Acta* **2008**, *47* (3), 301-318.
126. Spenley, N.; Cates, M.; McLeish, T., Nonlinear rheology of wormlike micelles. *Physical review letters* **1993**, *71* (6), 939.
127. van Santvoort, J.; Golombok, M., Sweep enhancers for oil recovery. *Journal of Petroleum Exploration and Production Technology* **2016**, *6* (3), 473-480.
128. Almansour, A. O.; AlQuraishi, A. A.; AlHussin, S. N.; AlYami, H. Q., Efficiency of enhanced oil recovery using polymer-augmented low salinity flooding. *Journal of Petroleum Exploration and Production Technology* **2017**, *7* (4), 1149-1158.
129. Lin, Z.; Cai, J.; Scriven, L.; Davis, H., Spherical-to-wormlike micelle transition in CTAB solutions. *The Journal of Physical Chemistry* **1994**, *98* (23), 5984-5993.
130. Das, N. C.; Cao, H.; Kaiser, H.; Warren, G. T.; Gladden, J. R.; Sokol, P. E., Shape and Size of Highly Concentrated Micelles in CTAB/NaSal Solutions by Small Angle Neutron Scattering (SANS). *Langmuir* **2012**, *28* (33), 11962-11968.
131. Shikata, T.; Hirata, H.; Kotaka, T., Micelle formation of detergent molecules in aqueous media: viscoelastic properties of aqueous cetyltrimethylammonium bromide solutions. *Langmuir* **1987**, *3* (6), 1081-1086.

132. Mendes, E.; Narayanan, J.; Oda, R.; Kern, F.; Candau, S. J.; Manohar, C., Shear-Induced Vesicle to Wormlike Micelle Transition. *The Journal of Physical Chemistry B* **1997**, *101* (13), 2256-2258.
133. Krishnaswamy, R.; Ghosh, S. K.; Lakshmanan, S.; Raghunathan, V. A.; Sood, A. K., Phase Behavior of Concentrated Aqueous Solutions of Cetyltrimethylammonium Bromide (CTAB) and Sodium Hydroxy Naphthoate (SHN). *Langmuir* **2005**, *21* (23), 10439-10443.
134. Hu, Y.; Matthys, E. F., Effect of metal ions and compounds on the rheological properties of a drag-reducing cationic surfactant solution exhibiting shear-induced structure formation. *Journal of colloid and interface science* **1997**, *186* (2), 352-359.
135. Xin, X.; Wang, L.; Shen, J.; Xu, G.; Li, Y., Rheological properties of hydrolyzed polyacrylamide/sodium oleate mixed system in the presence of different inorganic salts. *Journal of Petroleum Science and Engineering* **2014**, *114*, 15-21.
136. Zheng, Z.-Y.; Li, F.-C.; Wang, L.; Li, X.-B.; Zhang, H.-N.; Cai, W.-H.; Zheng, X., Experimental study on rheological and thermophysical properties of seawater with surfactant additive—part I: rheological properties. *Rheologica Acta* **2018**, *57* (10), 619-633.
137. Turner, M.; Cates, M., Linear viscoelasticity of wormlike micelles: a comparison of micellar reaction kinetics. *Journal de Physique II* **1992**, *2* (3), 503-519.
138. Kuryashov, D.; Philippova, O.; Molchanov, V.; Bashkirtseva, N. Y.; Diyarov, I., Temperature effect on the viscoelastic properties of solutions of cylindrical mixed micelles of zwitterionic and anionic surfactants. *Colloid journal* **2010**, *72* (2), 230-235.
139. Fischer, P.; Rehage, H., Rheological master curves of viscoelastic surfactant solutions by varying the solvent viscosity and temperature. *Langmuir* **1997**, *13* (26), 7012-7020.
140. Fischer, E.; Callaghan, P. T., Shear banding and the isotropic-to-nematic transition in wormlike micelles. *Physical Review E* **2001**, *64* (1), 011501.
141. Lequeux, F., Reptation of connected wormlike micelles. *EPL (Europhysics Letters)* **1992**, *19* (8), 675.
142. Truong, M. T.; Walker, L. M., Quantifying the Importance of Micellar Microstructure and Electrostatic Interactions on the Shear-Induced Structural Transition of Cylindrical Micelles. *Langmuir* **2002**, *18* (6), 2024-2031.
143. Grand, C.; Arrault, J.; Cates, M., Slow transients and metastability in wormlike micelle rheology. *Journal de Physique II* **1997**, *7* (8), 1071-1086.

144. Yesilata, B.; Öztekin, A.; Neti, S., Instabilities in viscoelastic flow through an axisymmetric sudden contraction. *Journal of non-newtonian fluid mechanics* **1999**, *85* (1), 35-62.
145. Ghosh, I.; Joo, Y. L.; McKinley, G. H.; Brown, R. A.; Armstrong, R. C., A new model for dilute polymer solutions in flows with strong extensional components. *Journal of Rheology* **2002**, *46* (5), 1057-1089.
146. Tamaddon-Jahromi, H.; López-Aguilar, J.; Webster, M., On modelling viscoelastic flow through abrupt circular 8: 1 contractions—matching experimental pressure-drops and vortex structures. *Journal of Non-Newtonian Fluid Mechanics* **2018**, *251*, 28-42.
147. Reiner, M., The Deborah number. *Physics today* **1964**, *17* (1), 62.
148. Metzner, A.; White, J.; Denn, M., Constitutive equations for viscoelastic fluids for short deformation periods and for rapidly changing flows: significance of the Deborah number. *AIChE Journal* **1966**, *12* (5), 863-866.
149. Poole, R., The Deborah and Weissenberg numbers. *Rheol. Bull* **2012**, *53* (2), 32-39.
150. Öttinger, H. C., Generalized Zimm model for dilute polymer solutions under theta conditions. *The Journal of chemical physics* **1987**, *86* (6), 3731-3749.
151. Rodd, L. E.; Scott, T. P.; Boger, D. V.; Cooper-White, J. J.; McKinley, G. H. In *Planar entry flow of low viscosity elastic fluids in micro-fabricated geometries*, Proceedings of the XIVth international congress on rheology, NF24-1-NF24-4, 2004.
152. Rodd, L. E.; Lee, D.; Ahn, K. H.; Cooper-White, J. J., The importance of downstream events in microfluidic viscoelastic entry flows: Consequences of increasing the constriction length. *Journal of non-Newtonian fluid mechanics* **2010**, *165* (19-20), 1189-1203.
153. Hidema, R.; Oka, T.; Komoda, Y.; Suzuki, H., Effects of flexibility and entanglement of sodium hyaluronate in solutions on the entry flow in micro abrupt contraction-expansion channels. *Physics of Fluids* **2019**, *31* (7), 072005.
154. Rodd, L.; Cooper-White, J.; Boger, D.; McKinley, G. H., Role of the elasticity number in the entry flow of dilute polymer solutions in micro-fabricated contraction geometries. *Journal of Non-Newtonian Fluid Mechanics* **2007**, *143* (2-3), 170-191.
155. Gulati, S.; Muller, S. J.; Liepmann, D., Direct measurements of viscoelastic flows of DNA in a 2: 1 abrupt planar micro-contraction. *Journal of Non-Newtonian Fluid Mechanics* **2008**, *155* (1-2), 51-66.
156. Fouxon, A.; Lebedev, V., Spectra of turbulence in dilute polymer solutions. *Physics of Fluids* **2003**, *15* (7), 2060-2072.

157. Shi, X.; Kenney, S.; Chapagain, G.; Christopher, G. F., Mechanisms of onset for moderate Mach number instabilities of viscoelastic flows around confined cylinders. *Rheologica Acta* **2015**, *54* (9-10), 805-815.